Masteroppgave

NTNU
Norges teknisk-naturvitenskapelige universitet
Fakultet for informasjonsteknologi og elektroteknikk
Institutt for elektroniske systemer

Peter N. Sundgaard

Design, Simulations and Fabrication of Silicon-On-Insulator Long-Period Grating Couplers for Nanophotonic Sensor Applications

Masteroppgave i Nanotechnology
Veileder: Astrid Aksnes
Medveileder: Jens Høvik
Juni 2023

NTNU
Kunnskap for en bedre verden

Peter N. Sundgaard

Design, Simulations and Fabrication of Silicon-On-Insulator Long-Period Grating Couplers for Nanophotonic Sensor Applications

Masteroppgave i Nanotechnology
Veileder: Astrid Aksnes
Medveileder: Jens Høvik
Juni 2023

Norges teknisk-naturvitenskapelige universitet
Fakultet for informasjonsteknologi og elektroteknikk
Institutt for elektroniske systemer

NTNU

Kunnskap for en bedre verden

NTNU

Kunnskap for en bedre verden

Master's Thesis

Design and Simulations of Silicon-on-Insulator Long-Period Grating Couplers for Nanophotonic Sensor Applications

Author:
Peter N. Sundgaard

12th June 2023

Abstract

Integrated photonic sensors have gained significant attention for their potential applications in medical diagnostics and environmental monitoring. This thesis focuses on the design, simulation, and fabrication of silicon-on-insulator (SOI) long-period grating (LPG) couplers with high sensitivity and desirable transmission characteristics for bio-related applications. Two generic LPG coupler designs, namely single and double LPG couplers, are considered as the basis for other designs. The sensitivity and transmission of these designs are calculated, and promising structures are fabricated into physical devices and subjected to transmission measurements.

The study utilizes a frequency domain eigenproblem solver to calculate dispersion relations and grating periods for coupling and sensitivity in the mid-infrared range. Transmission simulations are conducted with eigenmode expansion methods to evaluate the performance of the structures. Fabrication of the selected structures is carried out using electron beam lithography and plasma-reactive ion etching, followed by characterization with a scanning electron microscope. The measurements are performed in a laser laboratory with cleaved fibers for light coupling.

The results for the single LPG coupler indicate that there are discrepancies between the predicted coupling in simulations and the actual transmission measurements. These discrepancies are attributed to differences in simulation software and the consideration of grating geometry. The fabricated samples did not exhibit coupling effects, which were attributed to short grating lengths and shallow depths.

For the double LPG coupler design, simulations predict high sensitivity and a wide operation range. The fabricated sample for this design, however, suffered from damage and was unsuitable for transmission measurements.

In both cases, the results indicate that asymmetric modes achieve stronger coupling for grating periods corresponding to even order diffraction modes, while symmetric modes achieve stronger coupling for odd ones.

In conclusion, the simulation results demonstrate the potential of double LPG couplers for high sensitivity in nanophotonic sensor devices for biomedical applications. Further investigations are necessary to address transmission properties, loss, dispersion, and other challenges associated with physical devices.

Sammendrag

Denne masteroppgaven fokuserer på design, simulering og fabrikkering av silisium-på-isolator (SOI) langperiodiske gitterkoblinger (LPG) for bruk i integrerte fotoniske kretser. Slike nanofotoniske sensorer basert på små, men geometrisk enkle, bølgeledere har potensiale for å oppnå svært høy sensitivitet og vil kunne anvendes innen medisinsk diagnostikk og deteksjon av miljøgifter.

To generiske LPG-koblere, enkelt- og dobbel LPG-kobler, vil være et utgangspunkt for design og optimalisering av strukturer i den hensikt å oppnå høyest mulig sensitivitet over et bredt operasjonsspekter, samtidig som gode transmisjonsegenskaper er ivaretatt. Strukturer som oppfyller disse kravene vil realiseres som fysiske enheter slik at faktiske transmisjonsmålinger også kan foretas.

Datasimuleringer blir gjort i den fritt tilgjengelige programvaren MIT Photonic Bands for å beregne dispersjonsrelasjoner, gitterperioder for kobling og sensitivitet. Transmisjonssimuleringer utføres ved hjelp av programvare fra Lumerical MODE. Med utgangspunkt i funn fra simuleringene vil utvalgte strukturer fabrikkeres på substrater deponert med silisiumoksid (SiO_2) og amorft silisium (αSi) ved hjelp av elektronstrålelitografi (EBL) etterfulgt av plasma-reaktiv ioneetsing (ICP-RIE). Påfølgende karakterisering gjennomføres ved hjelp av et electronmikroskop (SEM). Vellykkede prøver gjennomgår transmisjonsmålinger i et laserlaboratorium.

Resultatene for enkelt LPG-kobler viser noe avvik mellom predikert koblingsperioder i simuleringene og observert resonanser. Avvikene tilskrives forskjeller i simuleringsmetodene og om gittergeometrien var inkludert eller ikke. Ingen resonanser i transmisjonen ble observert i målingene, hvilket mest sannsynlig skyldes for korte gitterlengder og for liten gitterdybde.

Simuleringene for dobbel-LPG-kobler predikerte høye sensitiviteter for et relativt bredt operasjonsspekter og viste akseptabel transmisjonsegenskaper. Strukturene ble også fabrikkert, men aktuelle prøve ble ødelagt av et defekt kløyveinstrument før noen transmisjonsmålinger var blitt gjort.

For å konkludere viser simuleringene av doble LPG-koblinger lovende sensitivitetsegenskaper som har potensiale for biomedisinsk bruk. Ytterligere forskning knyttet til transmisjonen kreves for å undersøke tap, dispersjon og andre utfordringer forbundet med fysiske enheter.

Table of Contents

List of Figures

List of Tables

0.1 Problem Description

Integrated photonics involve the design and development of miniaturized optical components, such as dielectric waveguides, modulators and resonators, onto a single chip. Due to its large refractive index contrast, silicon-on-insulator technology offers a highly suitable platform for the integration of these components into high-performance devices.

In this master's project, multiple long period grating (LPG) couplers will be designed, simulated and fabricated on the SOI material platform for use as nanophotonic biosensors. LPG couplers are corrugated waveguides that can be designed to achieve coupling between selected modes by adjusting the structure geometry. This coupling effect can be utilized for sensing purposes to obtain simple devices with superior sensitivity. This project will consider two generic coupler designs: a single LPG coupler consisting of one single waveguide and a double LPG coupler composed of two waveguides. Both designs will be subject to the same simulations and fabrication procedures.

Computer simulations aiming to optimize sensitivity of each design will be performed using eigenmode computations with MIT Photonic Bands (MPB). The transmission properties of selected structures from these simulations will then be investigated with eigenmode expansion methods offered by Lumerical.

The main focus is on the design and simulations, but promising devices will be realized and subject to transmission measurements. Fabrication will be conducted at the cleanroom facilities of NTNU NanoLab utilizing suitable nanofabrication techniques, such as electron beam lithography (EBL) and inductively coupled plasma-reactive ion etching (ICP-RIE). Characterization will be performed using scanning electron microscopy (SEM).

Chapter 1

Introduction

Integrated photonic sensors have been subject to extensive research in recent years due to their potential for a wide range of important applications [1]. Medical diagnostics and environmental monitoring for toxin detection in ocean water are examples of areas where the development of low-cost and high-performance devices would greatly benefit both public health and environmental health.

Silicon-on-insulator (SOI) devices are of particular interest due to their compatibility with conventional complementary metal-on-oxide semiconductor (CMOS) fabrication techniques, their reliability, and their low material cost [2]. This makes them promising candidates for photonic lab-on-chip devices.

Photonic sensors often rely on the evanescent field of the guided mode for sensing, and their sensitivity is directly related to the magnitude of the evanescent field. However, there are limitations and drawbacks to many of these sensors. For example, Mach-Zehnder-based devices have demonstrated high sensitivity [3, 4], but they can suffer from signal ambiguity and relatively large size. These issues have been partially addressed by incorporating ring resonators to enable easier multiplexing and unambiguous measurements [5, 6], but at the cost of reduced sensitivity.

Long period grating (LPG) couplers are a type of optical device that keeps a lot of the same advantages while maintaining a high sensitivity [7]. These devices are based on the principle of coupling light between two modes using a periodic perturbation of the waveguide's refractive index [8]. They have a number of attractive features for sensor applications, including high sensitivity, small size, and the ability to multiplex multiple sensors on a single device. Due to the existence of a phase matching turning point, these devices have theoretically infinite sensitivity for certain wavelengths. Høvik et al. successfully fabricated such a device yielding a sensitivity of 5.078 µm/RIU through a fairly simple fabrication process[7]. Adjusting the design to obtain a high sensitivity for a wider operation range with a single mode structure was proposed as a possible improvement.

The goal of this project is to design, simulate, analyze and fabricate silicon-on-insulator (SOI) long-period grating (LPG) couplers that yield high sensitivity for a wide operation range and exhibit desirable transmission characteristic for bio-related applications.

The study will consider the two generic LPG coupler designs as basis for other designs: the single LPG coupler and the double LPG coupler. Sensitivities and transmission will be calculated for both types and promising structures will be subject to fabrication and transmission measurements.

The basic theory behind electromagnetic theory, waveguides, mode coupling and computational electromagnetism is presented in Chapter 2. Chapter 3 introduces the specific tools used for simulations, while fabrication, simulation and measurement procedures are described in Chapter 5, 4 and 6, respectively. Results and discussions of the single LPG coupler design is presented in Chapter 7, while Chapter 8 presents the results and discussions of the double LPG coupler. Everything is finally concluded in Chapter 9.

Chapter 2

Theory

This theory aims to provide a comprehensive overview of the fundamental concepts of electromagnetism, as well as a brief introduction to the additional theory required to understand the physical principles behind a long period grating coupler sensor. This includes the discussion of Maxwell's equations, guided waves optics, and coupled mode theory.

The wave equation will be derived from Maxwell's relations and presented as an eigenproblem, the theory of which is based on the first chapters of [9]. This eigenproblem will then be applied to a waveguide system with relevant boundary conditions. Guided waves optics are introduced through simpler approximations in order to provide a useful intuition for the reader, rather than an exhaustive mathematical treatment. Silicon-on-insulator photonics will therefore not be covered in detail.

To gain insight into the periodic coupling mechanism of waveguides, coupled mode theory is presented using the example of two waveguides in close proximity. A periodic perturbation is then analyzed by solving the electromagnetic eigenproblem for periodic materials, resulting in the emergence of Bloch modes and the phase match condition.

Finally, all of these concepts are brought together to present the specific sensor structure that will be simulated in the experimental procedure. The computational electromagnetism techniques used in these simulations are also presented at this point.

2.1 Electromagnetic theory of light

2.1.1 Maxwell's Equations and the General Wave Equation

The electromagnetic theory of light describes light as a wave of electric and magnetic fields, $\mathbf{E}$ and $\mathbf{H}$, propagating through a dielectric medium according to Maxwell's equations,

$$\nabla \times \mathbf{E} = -\frac{\partial \mathbf{B}}{\partial t} \tag{2.1}$$

$$\nabla \times \mathbf{H} = \mathbf{J} + \frac{\partial \mathbf{D}}{\partial t} \tag{2.2}$$

$$\nabla \cdot \mathbf{D} = \rho \tag{2.3}$$

$$\nabla \cdot \mathbf{B} = 0 \tag{2.4}$$

where $\mathbf{D}$ is the displacement field, $\mathbf{B}$ is the magnetic induction field, ρ is the charge density of the medium and $\mathbf{J}$ is the electric current density. The medium is considered to be non-conductive without any free charges or currents so that $\rho = \mathbf{J} = 0$. All electric dipole moments induced by the electric field inside the medium are summed into the polarization density $\mathbf{P}$. Thus, the polarization density can be viewed as the system's response to an external electric field. The magnetization $\mathbf{M}$ is equivalently a response to the magnetic field $\mathbf{H}$. Maxwell's equations can then be simplified further by imposing certain restrictions on the material with regards to this response.

Firstly, we consider the material to be linear if the vector field $\mathbf{P}$ ($\mathbf{M}$) is linearly related to the electric (magnetic) field $\mathbf{E}$ including only first order terms of the fields expressed as

$$\mathbf{D}(\mathbf{r}) = \epsilon_0 \epsilon \mathbf{E}(\mathbf{r}) \tag{2.5}$$

$$\mathbf{B}(\mathbf{r}) = \mu_0 \mu \mathbf{H}(\mathbf{r}) \tag{2.6}$$

where ϵ_0 and μ_0 are the vacuum permittivity and permeability, while ϵ and μ are the relative permittivity and permeability, respectively. $\mathbf{r}$ is the spatial position vector. Henceworth, only non-magnetic materials are considered so that $\mu = 1$. Furthermore, the medium is considered to be homogeneous and isotropic. Such media have a relation between $\mathbf{E}$ and $\mathbf{P}$ that is independent of the position $\mathbf{r}$ and direction of $\mathbf{E}$. Lastly, we idealize the material to be nondispersive, i.e. to have an instantanous response to the external field. The relative permittivity ϵ will in general be a frequency dependent dielectric function $\epsilon(\mathbf{r}, \omega)$ of spatial direction, but these dependencies are omitted for isotropic non-dispersive media. As the material is assumed to be transparent, ϵ is also real and positive.

Using these restrictions on our system, Maxwell's equations is simplified to

$$\nabla \times \mathbf{E} = -\mu \frac{\partial \mathbf{H}}{\partial t} \tag{2.7}$$

$$\nabla \times \mathbf{H} = \epsilon \frac{\partial \mathbf{E}}{\partial t} \tag{2.8}$$

$$\nabla \cdot \mathbf{D} = 0 \tag{2.9}$$

$$\nabla \cdot \mathbf{B} = 0. \tag{2.10}$$

Solutions to eqns. (2.7)-(2.10) require certain conditions at the boundary between two dielectric media in a given system. With no surface currents or charges, the boundary conditions are:

1. The tangential components of the electric and magnetic field must be continuous

2. The normal components of the electric and magnetic field must be continuous

Applying the curl operator to equation (2.7) and combining with equation (2.8) allows us to decouple Maxwell's equations into one equation expressed in $\mathbf{E}$, which shows that the electric field satisfies the wave equation

$$\nabla^2 u - \frac{1}{c^2}\frac{\partial^2 u}{\partial t^2} = 0 \tag{2.11}$$

where the scalar function $u(\mathbf{r}, t)$ represents any of the six components of the electric- and magnetic-field vector. c in equation (2.11) is the speed of the light that propagates through the medium

$$c = \frac{1}{\sqrt{\epsilon\mu}}. \tag{2.12}$$

The light speed c differs from the speed of light propagating through free space, c_0 by a factor called the refractive index. The value of this quantity depends on the material of consideration and is given as

$$n = \frac{c_0}{c} = \sqrt{\frac{\epsilon}{\epsilon_0}}, \quad \epsilon_0 = \frac{1}{\sqrt{\epsilon_0\mu_0}} \tag{2.13}$$

As will be seen later on, the refractive index is the most important material property in the context of waveguides and photonic sensors.

2.1.2 Electromagnetism Formulated as an Eigenproblem

All equations derived from Maxwell's equations thus far in this section hold for electromagnetic fields of an arbitrary time-dependence. The form of this dependence depends on the electric source functions in equation (2.2) and (2.3). Nevertheless, an arbitrary periodic time function may be expanded into a series of harmonic sinusoidal components, a so-called Fourier series [10]. As Maxwell's equations are linear differential equations, sinusoidal time variations of source functions will result in sinusoidal variations in the electric and magnetic fields with the same frequency as the source during steady state. Thus, it is possible to separate the time dependence from the spatial dependence of $\mathbf{E}$ and $\mathbf{H}$ by expanding them into time-harmonic modes, i.e. steady-state sinusoidal field relationships on the form

$$\begin{aligned} \mathbf{E}(\mathbf{r}, t) &= \mathbf{E}(\mathbf{r})e^{-j\omega t} \\ \mathbf{H}(\mathbf{r}, t) &= \mathbf{H}(\mathbf{r})e^{-j\omega t}, \end{aligned} \tag{2.14}$$

where j is the imaginary unit, t is time and $\omega = 2\pi f$ is the angular frequency. Expressing the fields as complex functions simplifies the mathematics considerably while retaining all information; The physical fields are the real part of the complex functions.

Inserting equation (2.14) into the two divergence equations, (2.9) and (2.10), of Maxwell's equations yields two important conditions:

$$\begin{aligned} \nabla \cdot \mathbf{H}(\mathbf{r}) &= 0 \\ \nabla \cdot [\epsilon \mathbf{E}(\mathbf{r})] &= 0. \end{aligned} \tag{2.15}$$

These conditions stipulate that the field configurations consist of *transverse* electromagnetic waves [9]. I.e. equation (2.15) requires that for a plane wave $\mathbf{H}(\mathbf{r}) = \mathbf{a}e^{i\mathbf{k}\cdot\mathbf{r}}$, for some wave vector $\mathbf{k}$, $\mathbf{a}$ and $\mathbf{k}$ are orthogonal so that $\mathbf{a} \cdot \mathbf{k} = 0$. This condition is also called the transversality requirement.

As with what was shown for equation (2.11), (2.8) and (2.7) can be combined, now with the time-harmonic magnetic field expression, to give

$$\nabla \times \left(\frac{1}{\epsilon} \nabla \times \mathbf{H}(\mathbf{r}) \right) = \left(\frac{\omega}{c} \right)^2 \mathbf{H}(\mathbf{r}) \tag{2.16}$$

which can be rewritten as

$$\hat{\Theta}\mathbf{H}(\mathbf{r}) = \left(\frac{\omega}{c} \right) \mathbf{H}(\mathbf{r}), \tag{2.17}$$

where $\hat{\Theta} = \nabla \times \frac{1}{\epsilon} \nabla \times$. Because equation (2.16) and (2.15) together contain all information about $\mathbf{H}$ that is needed, equation (2.16) is called the master equation. It is formulated in terms of $\mathbf{H}$ due to mathematical convenience. Also note that it is on the same form as equation (2.11), which should be no surprise.

The master equation is, as indicated by the reformulation in (2.17), an *eigenproblem* that actually constitutes the core of electromagnetism. $\mathbf{H}(\mathbf{r})$ is the eigenfunctions with eigenvalues ω^2/c^2 that is calculated to describe an electromagnetic system. $\mathbf{E}$ is readily found once $\mathbf{H}$ is. Another attribute that follows from the eigenproblem perspective is that the differential operator $\hat{\Theta} = \nabla \times \frac{1}{\epsilon} \nabla \times$ contains many properties that can be used to understand more about the subject of interest - the eigenmodes.

Currently, there is a significant amount of concepts to process. The master equation being an eigenproblem signifies that when the function $\mathbf{H}(\mathbf{r})$ is subjected to a series of operations $\hat{\Theta}$ and the outcome is the same function multiplied by a constant, then $\mathbf{H}$ represents the spatial pattern of a permitted harmonic mode in a geometric material represented by the dielectric constant ϵ. Because the solution to this eigenproblem is a mode, it is known as an eigenmode. As previously mentioned, by examining the operator $\hat{\Theta}$, many properties of the eigenmodes can also be understood.

Firstly, $\hat{\Theta}$ is a linear operator. That means any linear combination of solutions to the master equation, is also a solution to the same equation. Secondly, $\hat{\Theta}$ is Hermitian, which means that the operator acts the same to the left and to the right under the inner product of two vector fields. This allows for a couple of conclusions regarding the eigenmodes and eigenvalues:

1. All eigenmodes $\mathbf{H}(\mathbf{r})$ are orthogonal[1]
2. All eigenvalues ω^2/c^2 are real
3. Eigenmodes can be obtained by a variational principle

It is straightforward to demonstrate the validity of these conclusions, and proof may be found in [9]. It is worth noting that the orthogonality of modes allows for the separate transmission of multiple modes through a system without interference. The implications of real eigenvalues in the eigenproblem of electromagnetism depend on the specific application or system being considered. In general, real eigenvalues correspond to stable modes of wave propagation. The third consequence of the

[1]Some eigenmodes may have the same frequency but different field configuration, which means they are not necessarily orthogonal. These are said to be degenerate modes.

Hermitian operator related to the variational principle is included for completeness and will not be elaborated upon further.

Electromagnetic light can be three types of modes depending on the direction of the electric- and magnetic- field relative to the direction of propagation. If both fields are orthogonal to the direction of propagation, the wave is transverse electromagnetic (TEM). For a transverse electric (TE) mode, only the electric field is orthogonal to the direction of propagation, while the transverse magnetic (TM) mode only has an orthogonal magnetic field [2].

2.1.3 Scale Invariance of Maxwell's Equations

One of the important properties of Maxwell's equations is their scale invariance. This means that the equations are unchanged when the length, time, and mass scales of a system are changed by a common factor. That is, they are invariant under the scale transformation $\mathbf{r} \to s\mathbf{r}$ and $t \to st$, so that if $\mathbf{E}(\mathbf{r}, t)$ is a solution to one of Maxwell's equations then $\mathbf{E}(s\mathbf{r}, st)$ are also solutions with the same functional form.

2.2 Guided-waves optics

Maxwell's relations govern how the electromagnetic fields will behave in a system of various media and geometries. Waveguide

2.2.1 Planar-mirror waveguides

The simplest way to study a guided wave would be to have a light ray propagating in the x-y plane between two lossless infinitely planar mirrors separated by a distance d in vacuum. The ray would be reflected and bounce in between the mirrors with an angle θ making it propagating in the z-direction. Mathematically, the propagation is described by wavenumber $k = nk_0 = (0, k_y, k_z)$ where

$$\begin{aligned} k_y &= nk_0 \sin\theta \\ k_z &= nk_0 \cos\theta. \end{aligned} \tag{2.18}$$

The wavenumber originates from the wave equation where the eigenvalue in equation (2.16) is rewritten as $\omega/c \equiv k$. It determines how much of a phase change ϕ the wave experiences per meter of distance it propagates.

If we associate each ray inside the waveguide with a transverse electromagnetic (TE) plane wave we can investigate the total electromagnetic field between the mirrors as the sum of these plane waves. The wave is polarized in the x-direction and its wavevector lies in the y-z plane so that each reflection is accompanied by a phase change of π while the amplitude and polarization remains unchanged. Fields that satisfies what we call the *self-consistency condition* reproduces itself after every two reflections. In one roundtrip the wave undergoes two phase shifts, $\phi_d = 2k_y d$ while propagating in-between the boundaries, and two additional phase shifts, ϕ_u

[2] This is not necessarily the right definition for TE and TM modes in dielectric waveguides as both modes propagate with magnetic and electric fields orthogonal to the direction of propagation.

and ϕ_l during reflections at the upper and lower mirrors. For the self consistency condition to be satisfied the roundtrip has to equal a multiple of 2π so that [11]

$$\phi_d - \phi_u - \phi_l = 2\pi m, \quad m = 1, 2, 3, ... \tag{2.19}$$

Using equation (2.18) and the perfect mirror assumption , it can be shown that this requirement is only satisfied for bounce angles $\theta = \theta_m$ where [12]

$$\sin(\theta_m) = m\frac{\lambda}{2d}, \quad m = 1, 2... \tag{2.20}$$

and each integer m corresponds to the mth mode (or eigenmode) of the waveguide. These are the same modes as was discussed in section 2.1, but now restricted to waveguides. In the context of waveguides, the word "mode" is referring to a stable, propagating pattern of electric and magnetic fields that satisfies the self consistency condition. Thus, it has the same transverse distribution at all locations throughout the waveguide. It is a particular case of the general eigenmodes explained in section 2.1.

We define the propagation constant β of the guided wave as the z-component of its wavevector $\beta = k_z = k\cos\theta = nk_0\cos\theta$. The propagation constant of a specific mode depends on the refractive index of the medium between the mirrors and the angle of reflection $\beta_m = k\cos\theta_m$ which by using (2.20) yields

$$\beta_m^2 = k^2 - \frac{m^2\pi^2}{d^2} \tag{2.21}$$

and shows that the higher-order modes propagate with smaller propagation constants.

An important characteristic of a waveguide is the relation between the propagation constant β and the angular frequency ω. The so-called dispersion relation for mode m can be found from (2.21) where $k = \omega/c$ so that

$$\beta_m = \frac{\omega}{c}\sqrt{1 - m^2\frac{\omega_c^2}{\omega^2}} \tag{2.22}$$

where we have defined the cut-off frequency $\omega_c = \pi c/d$. This is the smallest frequency that satsifies the self-consistency condition and thus the smallest frequency that can be guided by the structure.

The complex amplitude of the electric field distribution inside the waveguide can be written on the form [13]

$$E_x(y, z) = a_m u_m(y) e^{-j\beta_m z}, \tag{2.23}$$

where

$$u_m(y) = \begin{cases} \sqrt{\frac{2}{d}}\cos\left(m\pi\frac{y}{d}\right), & m = 1, 3, 5, ... \\ \sqrt{\frac{2}{d}}\sin\left(m\pi\frac{y}{d}\right), & m = 2, 4, 6, ... \end{cases} \tag{2.24}$$

a_m is the amplitude of mode m. From section 2.1, one of the implications of an Hermitian operator $\hat{\Theta}$ in the master equation was that the resulting eigenmodes was orthogonal. It can be shown that

$$\int_{-d/2}^{d/2} u_m(y)u_l dy = 0, \quad l \neq m, \tag{2.25}$$

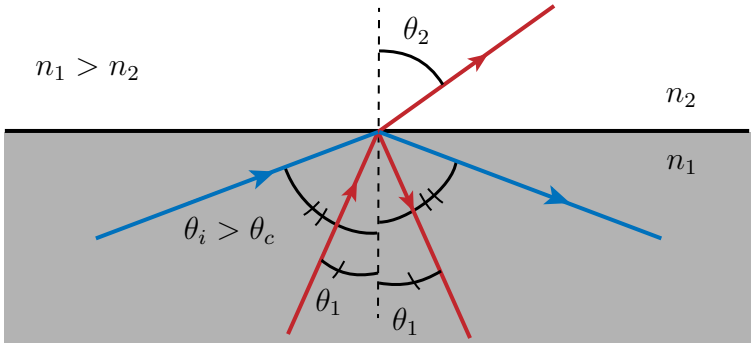

Figure 2.1: Snells law of refraction. Total internal reflection only occurs for incident angles θ_i that is larger than the critical angle θ_c, such as the blue ray in this figure. The red wave has an incident angle smaller than the critical angle and is thus refracted as well. Note that the angle θ in this figure is defined differently than in the case for waveguides in Figure 2.2 [3]. Figure reprinted with permission from [15].

which demonstrates that u_m satisfies the condition of orthoganlity within the constraints of the two mirrors. It can be shown that u_m is normalized within the boundaries, as well.

The field distributions are superpositions of the aforementioned upward and downward TEM waves. Even (symmetric) and odd (asymmetric) modes are the additive and subtractive superpositions, respectively. Furthermore, since the initial TEM planewaves were assumed to be x-polarized, then so is the total electric field and the guided wave is transverse electric (TE). A similar approach as what has been shown here can be applied to show that transverse magnetic (TM) waves are also supported by a mirror waveguide.

As a final note, it is important to clarify that even though the field distribution inside the wave guide is quantized to multiple modes, the guided light do not have to match one of these modes exactly. However, the optical power of the guided wave will be divided among the modes [14]. Thus, the collection of all possible modes form an orthogonal basis set.

2.2.2 Planar dielectric waveguides

Infinite and lossless mirror planes are due to obvious reasons impractical for real-life applications. They are most likely difficult to fabricate and highly expensive. Modern photonic integrated circuits are mostly based on dielectrics.

A planar dielectric waveguide follows much of the same principles as the planar-mirror waveguide. A dielectric slab, often called the core, of refractive index n_1 is surrounded by a cladding media of a lower refractive index n_2 so that a wave may be guided by the means of total internal reflection (TIR) at the dielectric boundaries as shown in Figure 2.2. Now that dielectric materials are introduced in place of mirrors, the critical angle, θ_c, becomes an important parameter. While the mirrors in section 2.2.1 losslessly reflect incoming waves, dielectric materials will either reflect or refract (or both) incoming waves depending on the incoming angle. The critical angle is the smallest angle that allows for TIR within the waveguide. This mechanism is governed by Snell's law given by

$$n_1 \sin\theta_1 = n_2 \sin\theta_2, \tag{2.26}$$

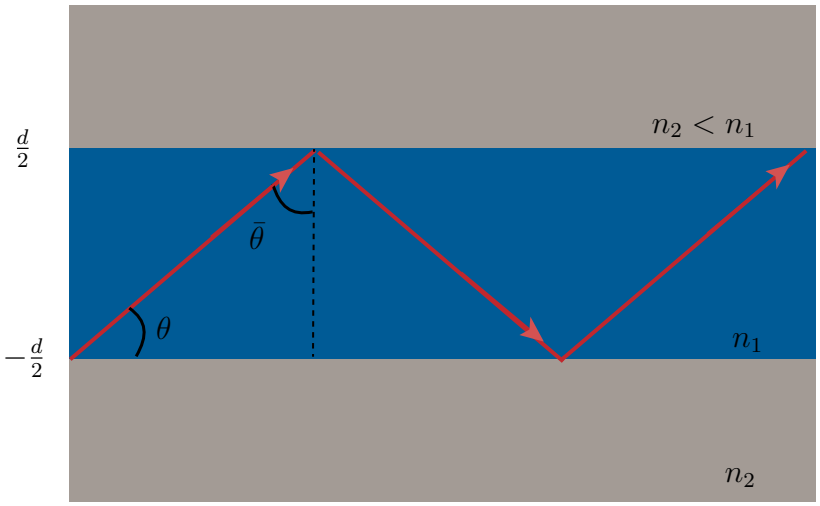

Figure 2.2: Schematic of how waves are guided through a dielectric slab waveguide by the means of TIR. The ble colored core is of a higher refractive index than the surrounding cladding $n_1 > n_2$ so that the wave propagates throughout.

and schematically shown in Figure 2.1. For all waves with incident angles θ_1 that makes $\theta_2 \leq 2\pi$, TIR occurs and the wave is supported throughout the waveguide. Thus, the critical angle is given by

$$\sin\theta_c = \frac{n_2}{n_1}. \tag{2.27}$$

Any wave with a larger angle than θ_c would partly refract into the cladding for each bounce and inevitably disappear from the core.

Similarly as for the planar mirror example, solutions to the electromagnetic eigenproblem within the waveguide are modes that satisfy the self-consistency condition. However, the reflection phase change is now dependent on the refractive index contrast at the core boundaries. It can be shown that for TE modes the self consistency condition takes on the form [16]

$$\tan\left(\pi\frac{d}{\lambda}\sin\theta - m\frac{\pi}{2}\right) = \sqrt{\frac{\sin^2\bar{\theta}_c}{\sin^2\theta} - 1}, \tag{2.28}$$

where the refractive index dependence is implicitly incorporated through θ_c. The solution to equation (2.28) yield the bounce angles θ_m for each mode m that propagates with propagation constant

$$\beta_m = n_1 k_o \cos\theta_m. \tag{2.29}$$

As previously mentioned, the propagation constant is the wave vector component along the propagation direction. Thus, it makes sense to define an *effective refractive index* n_{eff} that describes the propagating mode so that

$$\beta = n_1 k_0 \cos\theta = n_{\text{eff}} k_0 \tag{2.30}$$

or equivalently

$$n_{\text{eff}} = \frac{c_0\beta}{f} \tag{2.31}$$

where f is the frequency. Analogously to how the refractive index quantifies the increase in wavenumber that a wave experiences while propagating in a dielectric medium, the effective refractive index quantifies how a wave changes its wave number when propagating through a waveguide.

Dispersion relation and group velocities

The dispersion relation of a dielectric waveguide is comparable to that of a planar mirror waveguide, albeit slighlty more complicated. The relation between propagation constant β and angular frequency ω is obtained by rewriting the self consistency equation (2.28) in terms of these quantities. The resulting relation depends on the refractive indices involved in the waveguide, and certain restrictions are imposed on allowed modes similarly to the case of the planar mirror. Each mode β_m has its own relation to the frequency of the light that is guided, but all modes are confined between the *lightlines* of the structure. Figure 2.3 shows a schematic representation of the dispersion for some dielectric waveguide and how the modes are confined between the upper and lower lightline. The upper lightline represent propagation in homogeneous cladding medium $\omega = c_0/n_2\beta = c_2\beta$ while the lower lightline correspond to the propagation in homogeneous core material $\omega = c_0/n_1\beta$. As the frequency increases the dispersion relation for each mode approaches the lower lightline. This is equivalent to that the effective refractive index approaches the index of the core material $n_{\text{eff}} \to n_1$. This demonstrates how high frequency waves are confined more strongly to high refractive index materials.

The group velocity of each mode is found from the derivative of the dispersion relation [17]

$$v_g = \frac{d\omega}{d\beta}. \tag{2.32}$$

It is the velocity at which the envelope of a wave pulse propagates through the waveguide. In most cases it can be interpreted as the speed at which a signal is propagating through the waveguide[4].

Analogously to the refractive index, the group index can be defined as the ratio of the vacuum velocity of light c_0 and the group velocity v_g [19]:

$$n_g = \frac{c_0}{v_g} \tag{2.33}$$

An important takeaway from the dispersion relation discussed here is that for a specific frequency, there exist guided modes and *cladding modes*. The cladding modes are located in the shaded are of 2.3 which means they won't be guided by the waveguide. Nevertheless, the fact that they exist is very imporant blabla because as we will se it is possible to couple to these waves blabla

So far, only symmetric dielectric waveguides have been considered, despite the fact that this project actually aims to simulate silicon-on-insulator waveguides that are *asymmetric*. Figure 2.2 shows a symmetric waveguide where the refractive index of the top and bottom layer are identical. An asymmetric waveguide, on the other hand, will have two different indices which makes the refractive index contrast for the top and bottom boundaries of the core asymmetrical, as depicted to the

[4]Not the case for medium with high absorption and dispersion [18]

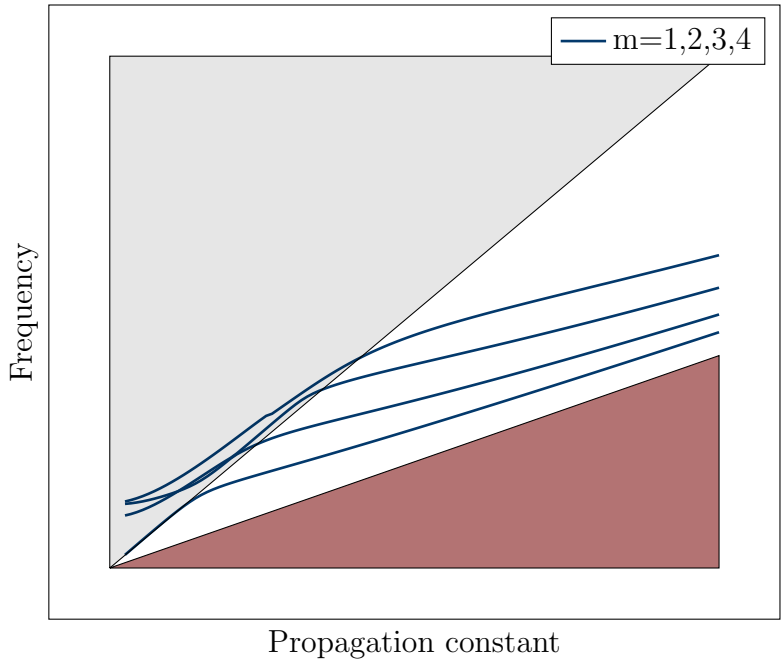

Figure 2.3: Schematic representation of the dispersion relation of a dielectric waveguide. Allowed modes are represented by the blue lines confined by two lightlines associated with forbidden states indicated by the shaded areas. All frequencies above the upper lightline $\omega = c_2\beta$ are shaded with grey as these modes will not be guided at certain frequencies. Similarly, the lower lightline $\omega = c_1\beta$ represent the lower boundary for the modes. As the frequency increases, the dispersion relation of each modes moves from the upper lightline towards the lower lightline.

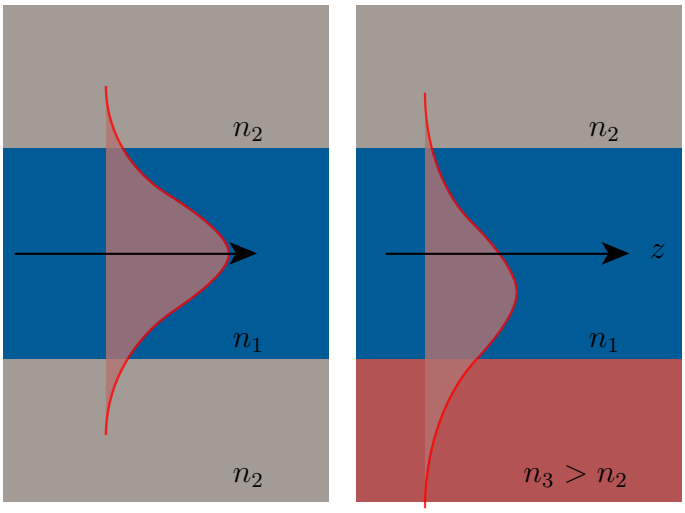

Figure 2.4: Field distributions of mode number 1 for symmetric (left) and asymmetric (right) waveguides. The field penetrates the upper and lower cladding equally for the symmetric waveguide, while the asymmetric case will have a deeper field penetration into the cladding with the highest refractive index. Figure adapted from [14].

right of Figure 2.4. Because the boundary conditions are different for asymmetric waveguides, the TIR and self-consistency condition will be slightly more complicated. However, the mechanism is the same; The guided wave reproduces itself after every two reflections and the phase change associated with each reflection depends on the refractive index contrast at the respective boundary. The result is a set of propagating modes that maintains their transverse field distribution throughout the waveguide. Another consequence of the asymmetric waveguide regards the field distribution.

Internal and External Field Distributions

The field distribution of TE modes in a waveguide was briefly discussed for the planar mirrors, mathematically expressed in equation (2.34). Due to the assumption of perfectly reflecting mirrors, these fields are completely confined within the waveguide core and vanish at the boundaries $y = \pm d/2$. This field property is not present in dielectric waveguides. Instead, there is a distinction between the *internal* and *external* field distribution. The internal field is defined inside the core between the two dielectric boundaries, while the external field is defined outside. Similarly to the planar mirror, the field distribution is the superposition of the upward and downward TEM waves and the solutions are sinusoidal. For $-d/2 \leq y \leq 2/d$ [20]

$$u_m(y) \propto \begin{cases} \cos\left(\omega \sin\theta_m y\right), & m = 0, 2, 4, ... \\ \sin\left(\omega \sin\theta_m y\right), & m = 1, 3, 5, ... \end{cases} \tag{2.34}$$

The modes have a slightly more complicated form, but the most important difference is that the internal field does not vanish at the boundaries anymore. However, the boundary conditions from 2.1.1 still applies, which set restrictions on the field outside of the core. This external field is also referred to as the evanescent field because it decays exponentially with the distance from the boundary, as shown in the left of Figure 2.4.

2.3 Silicon-on-Insulator photonics

Integrated optics in silicon has been the industrial convention for many decades and is still subject to extensive research [21]. The cost of silicon and SOI wafers are significantly lower than more exotic materials like III-V compounds GaAs and InP [22], both in terms of total material cost and processing costs. Furthermore, silicon is robust and well understood; The microelectronics industry already has a silicon processing and fabrication that is well-developed. Lastly, this technology is highly compatible with complementary metal-oxide-semiconductor (CMOS) fabrication [23].

All waveguides discussed so far confine the propagating light in one dimension. This is clearly a simplification that is not strictly valid for most real-life applications; the cladding will not extend infinitely in the x and y-direction. But the theory of planar mirror and planar dielectric waveguides does contain important concepts and valuable insights regarding the physics of wave propagation in photonic circuits. As was briefly discussed at the end of section 2.2.2, this project will revolve around two-dimensional silicon-on-insulator waveguides and these waveguides approximates the theoretical waveguides that has been discussed so far.

Figure 2.5 shows the configuration of a SOI waveguide, where the silicon core lies on top of an oxide layer which again lies on top of a silicon substrate. The waves are guided in the silicon core with a high refractive ($n_{\mathrm{Si}} \approx 3.5$) index. As discussed in section 2.2.2, the refractive index contrast at the boundaries has to be high for the waves to be confined within the core. The oxide layer is therefore of a much lower refractive index ($n_{\mathrm{SiO_2}} \approx 1.4$) than the core and functions as the bottom cladding layer. Additionally, it has to be thick enough to prevent the evanescent field to penetrate into the silicon substrate below [24].

Compared to the aforementioned planar dielectric waveguide, it appears that the upper cladding is missing. Certainly, this is not the case. It is actually the outer environment that works as the upper cladding and final constituent of the SOI waveguide. The refractive index of this part depends on what application the photonic device is boing designed for, but it is most often either air or, as for this project, water of $n_{\mathrm{H_2O}} \approx 1.3$. The fact that the outer environment is a part of the SOI waveguide configuration is precisely what makes it so suitable for sensor applications.

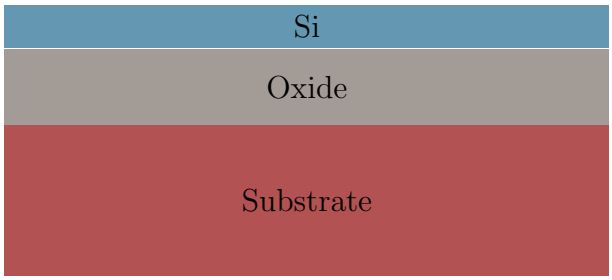

Figure 2.5: Material composition of an SOI planar waveguide. The modes are guided by silicon core on top.

2.4 Coupled mode theory

The existence of the evanescent field in dielectric waveguides enables an immensely useful phenomenon called waveguide coupling. When two waveguides are in sufficient proximity to one another, their fields may overlap and optical power is able to transfer between the two waveguides. This is actually a special case of optical tunneling which contains all forms of coupling such as coupling from a beam to a fiber or in-between fibers. The exact analysis of optical coupling is highly complex and beyond the scope of this project. The reader is referred to the works of Burns and Milton for a more formal treatment [25]. There is however an approximation known as coupled-mode theory that will suffice in a lot of cases - including here.

Coupled mode theory is better understood when explained through an example. When two waveguides are in close proximity, they will exchange power as a (often periodic) function of the direction of propagation. This situation can be explained mathematically with the assistance of an important assumption: The coupled modes are represented as a weighted sum of the individual guided modes. In other words, the mode of each waveguide is determined as if the other waveguide is absent [26]. This is a simplification as the modes in reality will be perturbed to some extent by the presence of the other waveguides. Furthermore, the waveguides are assumed to be single moded so that the total fields for the whole situation can be expressed as functions of the fields in each waveguide $\mathbf{E}_i$ and $\mathbf{H}_i$,

$$\begin{aligned} \mathbf{E} &= A(z)\mathbf{E}_1 + B(z)\mathbf{E}_2 \\ \mathbf{H} &= A(z)\mathbf{H}_1 + B(z)\mathbf{H}_2, \end{aligned} \tag{2.35}$$

where $A(z)$ and $B(z)$ is the amplitude of the mode in waveguide 1 and 2, respectively. The direction of propagation is set to be in z, so the z-dependence illustrates that the two waveguides will exchange power as the coupled mode propagates.

As explained in section 2.1 the fields have to satisfy Maxwell's equations and the relevant boundary conditions in order to be allowed solutions. $\mathbf{H}$ can be substituted into the master equation and $\mathbf{E}$ is readily found from $\mathbf{H}$. Doing these substitution and applying relevant vectors identities will yield the generalized coupled mode equations. The derivation is quite cumbersome, but the solutions will give a full description of the coupling between the two waveguides.

To simplify further into something more digestable, additional assumptions are applied. Firstly, the waveguides are assumed to be lossless so that the total optical power of the situation remains the same for all z. Secondly, the propagation constants of the modes, β_1 and β_2 are also assumed to be unchanged in z. Using this, the coupled mode equations are written as [26]

$$\begin{aligned} \frac{dA}{dz} &= -j\kappa_{21}Be^{j(\beta_1-\beta_2)z} \\ \frac{dB}{dz} &= -j\kappa_{12}Ae^{j(\beta_1-\beta_2)z}. \end{aligned} \tag{2.36}$$

The coupling coefficients κ describe how quickly power transfers from one waveguide to another, i.e. the efficiency of the coupling. The exponential describes the phase mismatch between the modes. As expected from the assumed conservation of power, the change in A is proportional to B and vice versa. The amplitude exchange also depends on the synchronization of the two phases. This has an immensely important

consequence as it shows that modes need a certain phase match to achieve efficient coupling.

Equation (2.36) can be solved by using harmonic trial solutions and applying appropriate boundary conditions, which yields solutions on the form

$$\begin{aligned} A(z) &= a_1(z)A(0) + a_2(z)B(0) \\ B(z) &= b_1(z)A(0) + b_2(z)B(0) \end{aligned} \tag{2.37}$$

where the a_i, b_i are elements of a transmission matrix $\mathbf{T}$ that relates the fields going in and out of the coupling region. These are all functions of the phase mismatch and refractive index of the materials involved. For identical waveguides, there is no phase mismatch and it can be shown that the transmission matrix takes on the form [27]

$$\mathbf{T} = \begin{bmatrix} a_1 & a_2 \\ b_1 & b_2 \end{bmatrix} = \begin{bmatrix} \cos\kappa z & -j\sin\kappa z \\ -j\sin\kappa z & \cos\kappa z, \end{bmatrix} \tag{2.38}$$

The subscripts of κ has been removed due to the reciprocity condition, $\kappa_{12} = \kappa_{21}^*$, which for real coupling coefficients means that $\kappa_{12} = \kappa_{21} = \kappa$. A complex coupling coefficient would simply mean a change of phase as one mode leaks into the other. As the optical powers are proportional to the amplitudes $A(z), B(z)$ squared ($P_A \propto |A|^2$, $P_B \propto |B|^2$), equation (2.38) shows that the power exchange between the two waveguides is periodic. This means that for some z all the optical power has coupled to the other mode, but for another z all the power has coupled back again. The *coupling length* is the propagation distance over which all the optical power has transferred to the other waveguide.

As the reader probably would have realized by now, many steps in this derivation have been skipped and many simplifications have been applied. This is mostly done with intent to help the reader from drowning in details. The point is to mathematically show how wave coupling can be understood as amplitudes being periodically transferred from one mode to another and that it is a consequence of Maxwell's equations discussed in section 2.1. The final result had an especially simple form because of the assumption of identical waveguides with matched phases.

2.4.1 Phase match condition

Phase matching is an important condition for high coupling efficiency [28], and was assumed in the coupled mode theory discussed in section 2.4. As the propagation constants of two modes diverges, the phase synchronization will reduce and so will the power transfer. If the two phases are sufficiently out of phase, no power transfer will occur at all. The question is therefore how to achieve matching propagation constants of two asynchronous modes to ensure adequate coupling - and the answer is to introduce a periodic perturbation in the waveguide. By introducing a grating to an electromagnetic system, it is possible to couple waves that are out of phase and even waves that are travelling in different directions. This happens due to generation of spatial harmonics with altered wavev ectors that depends on the periodicity of the grating.

The periodic perturbation, here described as a grating, could be any periodic change in the refractive index of the waveguide in question so that the dielectric

function repeats itself in space by some vector $\mathbf{K}$. This grating can generally be expressed as

$$\epsilon(\mathbf{r}) = \epsilon_{avg} + \Delta\epsilon \cos(\mathbf{K} \cdot \mathbf{r}), \tag{2.39}$$

where the delectric contrast of the grating $\Delta\epsilon$ is multiplied with a unit amplitude cosinusoidal function that varies with the grating vector $\mathbf{K}$ and an average dielectric value ϵ_{avg} is added. So the dielectric function swings periodically from some average value. The solutions to the master equation (2.16) for a periodic potential was found by Felix Bloch in 1929 to be a plane wave $e^{j\mathbf{k}\cdot\mathbf{r}}$ times a function with the same periodicity as the potential [29]

$$\mathbf{H}_\mathbf{k}(\mathbf{r}) = \mathbf{u}_\mathbf{k}(\mathbf{r}) e^{-j\mathbf{k}\cdot\mathbf{r}}. \tag{2.40}$$

where $\mathbf{u}_\mathbf{k}(\mathbf{r})$ has the same periodicity as ϵ. These eigenfunctions are called Bloch modes, and even though they were initially derived to solve the Schrõdinger equation, they are equally valid solutions in electromagnetism. What Bloch's theorem really shows is that a wave propagating through a periodic structure will take on the same symmetry. Another consequence is that only a discrete set of wavevector $\mathbf{k}$ are allowed. These are the spatial harmonics and are calculated using the grating equation. Physically it could be explained as a wave travelling through a periodic structure needs to keep the field continuous at all boundaries and this condition is only satisfied for certain propagation directions.

As the amplitude envelope of the Bloch mode takes on the same symmetry as the periodic structure it makes it possible to express the amplitude envelope as that dielectric function times some factor A that converts the dielectric functions into a field value. Thus, inserting equation (2.39) into equation (2.40) yields the following results

$$\begin{aligned}
\mathbf{H}_\mathbf{k}(\mathbf{r}) &= A\left[\epsilon_{avg} + \Delta\epsilon\cos(\mathbf{K}\cdot\mathbf{r})\right] e^{-j\mathbf{k}\cdot\mathbf{r}} \\
&= A\left[\epsilon_{avg} + \Delta\epsilon\frac{e^{j\mathbf{K}\cdot\mathbf{r}} + e^{-j\mathbf{K}\cdot\mathbf{r}}}{2}\right] e^{-ij\mathbf{k}\cdot\mathbf{r}} \\
&= A\epsilon_{avg} e^{-j\mathbf{k}\cdot\mathbf{r}} + \frac{A\Delta\epsilon}{2} e^{-j(\mathbf{k}-\mathbf{K})\cdot\mathbf{r}} + \frac{A\Delta\epsilon}{2} e^{-j(\mathbf{k}+\mathbf{K})\cdot\mathbf{r}}
\end{aligned} \tag{2.41}$$

Applying the symmetry condition on the Bloch eigenmodes results in three different terms that describe three different waves. The first term contains a complex exponential which indicates that the wave is travelling in the original direction, while the other terms are waves where the wave vector is altered by the addition or subtraction by the grating vector $\mathbf{K}$. The incident wave has split into three different waves due to the periodic perturbation. All the generated spatial harmonics will be subject to the same pertubation once more, creating three new waves for each harmonics and so on. The total set of allowed harmonics will be described by

$$\mathbf{k}_m = \mathbf{k} - m\mathbf{K}, \qquad m = \infty, ..., -1, 0, 1, ..., \infty \tag{2.42}$$

From section 2.1, one of the boundary conditions for electromagnetic systems was that the tangential components of the fields had to be continous. Now the wave vector of the modes inside the grating has to be expanded. Using this, the phase matching condition for a wave entering a grating becomes

$$k_{t,m} = k_t - mK_t \tag{2.43}$$

where $k_{t,m}$ is the tangential component of spatial harmonic m inside the grating, k_t is the tangential component of the incoming mode and K_t is the tangential component of the grating vector.

2.5 Long Period Grating coupler

So far, a general grating has been discussed. However, specific grating characteristics result in different properties of the coupling. A *long period grating* (LPG) is a grating that has a periodicity that is considerably longer than the wavelength of operation. The coupling mechanism of such gratings has been used vastly for optical fiber-based sensors [30] in recent years. LPG couplers are a special kind of codirectional couplers that is especially interesting for sensor application due to the so-called phase turning matching point at which the sensitivity is theoretically infinite.

2.5.1 Coupling

Figure 2.6 and Figure 2.7 depict 3D models of LPG couplers. The single waveguide geometry is designed to transfer power from a propagating mode to a leaky cladding mode, while the double waveguide structure is intended to couple power between the two waveguides. Both coupler types consist of a slab waveguide with a long period grating introduced. Near the grating, the periodicity in the refractive index of the material will generate a distribution of Bloch modes that satisfy the phase match condition from equation (2.43). The tangential component of the wave vectors can be rewritten as propagation constants in the case of waveguide modes, so that

$$\beta_m = \beta_0 + mK_t = \beta_0 + m\frac{2\pi}{\Lambda} \tag{2.44}$$

where β_ν is the modified propagation constant, β_0 is the propagation constant without the LPG and Λ is grating period as depicted in Figure **??**. As explained in section 2.4 two modes may exchange power through mode coupling, but phase matching is a requirement for a strong coupling. Thus, two asynchronous modes with propagation constant β_1 and β_2 may couple optically given the phase difference [7]

$$\beta_1 - \beta_2 = m\frac{2\pi}{\Lambda}. \tag{2.45}$$

By using equation (2.31) and the relation between wavelength λ and wave vector $k = 2\pi/\lambda$, equation (2.45) can be rearranged into an expression that gives the grating period required to couple mode 1 and 2 at wavelength λ:

$$\Lambda = m\frac{\lambda}{n_{\text{eff1}} - n_{\text{eff2}}} \tag{2.46}$$

n_{eff1} and n_{eff2} are the effective refractive indices of mode 1 and 2, respectively.

By introducing a grating with a periodicity that satisfies (2.46) for a specific wavelength λ, it is possible to achieve coupling between two modes at that wavelength. This coupling effect can be observed by measuring the transmission spectrum, which will reveal a dip at the coupling wavelength, also called resonance. This ability to achieve coupling at a specific wavelength is what enables the device to function as a

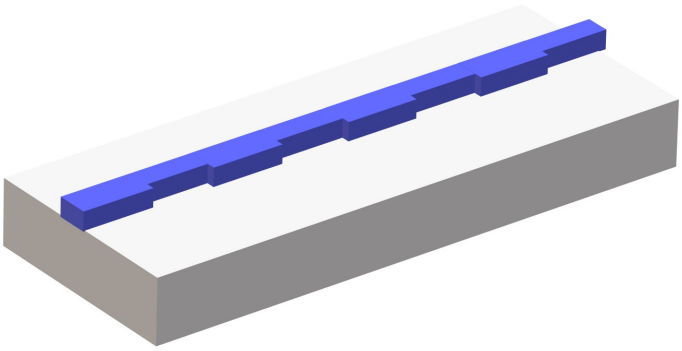

Figure 2.6: 3D model of the asymmetric waveguide coupler adapted from [7].

sensor. The particular wavelength at which coupling occurs depends on the effective refractive index of the two modes, which in turn depends on the refractive index of the environment surrounding the waveguide. Therefore, any change in the surrounding refractive index will cause a shift in the coupling wavelength and a corresponding shift in the transmission dip. By measuring this shift, it is possible to determine the amount by which the refractive index of the surroundings has changed, allowing the device to serve as a sensor.

2.5.2 Sensitivity

The sensitivity of an optical refractive index sensor is commonly defined as the ratio between resonance shift and change in refractive index $\Delta\lambda/\Delta n$, yielding a result measurable in micrometers per refractive index unit (µm/RIU). Using this definition, it is possible to derive the sensitivity of an LPG coupler from equation (2.46), which yields

$$S = \lambda \frac{\frac{dn_{\text{eff1}}}{dn_c} - \frac{dn_{\text{eff2}}}{dn_c}}{n_{g1} - n_{g2}}. \tag{2.47}$$

$\frac{dn_{eff1}}{dn_c}$ and $\frac{dn_{eff2}}{dn_c}$ are the effective index responses to a change in the cladding material of the two coupling modes, $n_{g1} - n_{g2}$ is the difference between the group index of the two modes and λ denotes the operation wavelength. According to equation (2.47), the sensitivity of the system is theoretically infinite at the point where $n_{g1} - n_{g2} = 0$, referred to as the phase matching turning point (PMTP). At the PMTP, the relative phase difference between the two coupled modes experiences a turning point. This characteristic of the PMTP is what makes LPG couplers particularly suitable for use in sensor applications.

2.6 Refractive Index Sensors for Bio Applications

Biosensors are designed to convert a physical or chemical quantity in a biological system into a measurable signal. Refractive index-based transduction has been widely used for this purpose due to its compact size, high sensitivity, reliability, portability, and low cost [2]. Optical sensing techniques can be divided into two

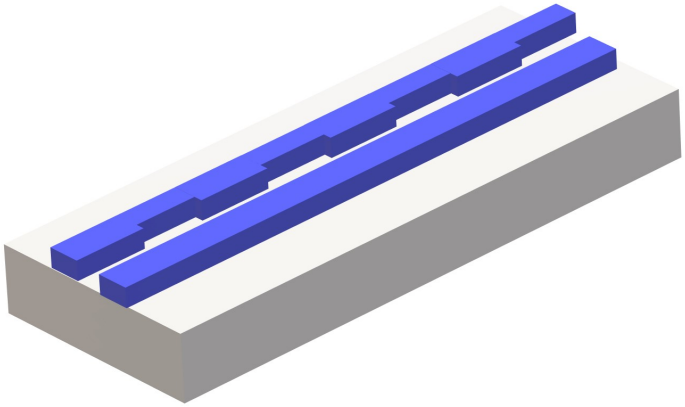

Figure 2.7: 3D model of the asymmetric waveguide coupler adapted from [7].

categories: label-free and fluorescence [31]. Label-free detection refers to methods that do not require the use of fluorescent labels or dyes to detect the presence or concentration of a target biomolecule. These methods rely on the inherent physical or chemical properties of the target biomolecule to generate a measurable signal.

In the context of photonic sensors, label-free sensing relies on the change in the refractive index at the sensor surface caused by the accumulation of target molecules in this area. To achieve this, the surface of the sensor is covered with biorecognition molecules, also known as antibodies. If target molecules are present in the system, they will bind to the antibodies. The biomolecules in the layer typically have a different refractive index than the surrounding environment, leading to a change in the refractive index at the surface of the sensor. This refractive index change results in a shift in the resonance of the signal transmission of the sensor, which can be measured.

2.7 Computational Electromagnetism

Photonics offers a unique advantage in numerical computations due to the accuracy of Maxwell's equations, well-known material properties, and the practicality of the length scales involved. This allows for quantitative theoretical predictions without the need for unreasonable assumptions or simplifications. As such, simulations are a valuable tool for optimizing photonic designs before fabrication.

The selection of solver techniques depends upon the objectives of the simulations. Specifically, this project employs computational software to model a waveguide sensor designed for biosensing purposes. The sensing component of the sensor is linked to the coupling mechanism that occurs between different modes. Therefore, it is necessary to utilize a frequency domain eigenproblem solver, available through the MIT Photonic Bands software. However, as the sensor is a finite-dimensional structure that requires measurement through the transmission of light, simulations of transmission are also critical. The bidirectional eigenmode expansion (EME) solver, obtainable through Lumerical MODE software, will therefore be employed to address this part of the analysis.

Although a detailed theory of computational methods used for the analysis of electromagnetic problems is outside the scope of this project, a general understand-

ing of these methods is necessary to correctly interpret the results of the simulations. A brief overview of common numerical techniques for solving Maxwell's equations is provided, and these methods are commonly used in computational photonics. Most of this overview is based on [9, Appendix D]. The specific simulation software used in this project will be discussed further in section 3.

2.7.1 Frequency Domain Eigenproblems

Frequency-domain eigenproblems are used to find the dispersion relation and associated field patterns of a waveguide. This is done by expressing the problem as a finite matrix eigenproblem and using linear algebra techniques to find the first few eigenvectors and values. For non-periodic structures, the supercell approximation can be used, which involves applying periodic boundary conditions to a large computational cell surrounding the localized mode. This effectively isolates the waveguide structure and allows for the study of its electromagnetic properties without considering the effects of the boundaries. The k-vector along a supercell direction determines the phase relation between the artificially repeated structures, but this phase relation becomes irrelevant as the size of the computational cell increases and the solution converges exponentially to the desired isolated-waveguide solution. This method is useful for studying localized modes that are exponentially confined to the waveguide.

Solving for all eigenvectors and values is straightforward, but it is typically too resource-intensive for practical purposes because the number of terms can be very large. An alternative approach is to only solve for the lowest few eigenvalues and eigenvectors using iterative methods, since the lowest modes are typically the ones of greatest interest.

Frequency-domain eigenproblems are not well-suited for analyzing all properties of interest for sensors. For example, it is not possible to use these methods to directly analyze transmission spectra for finite structures, as this information cannot be deduced from dispersion relations. However, information about eigenfrequencies and eigenmodes is crucial for interpreting the results of the transmission spectrum. In other words, even though frequency-domain eigenproblems cannot be used to directly analyze certain properties of interest, they can still provide valuable information that is necessary for understanding the behavior of sensors.

2.7.2 Eigenmode Expansion Methods

Eigenmode expansion (EME) methods are linear frequency-domain modeling technique that seek to address the aforementioned shortcomings of the frequency-domain eigenproblems related to transmission characteristics. By solving Maxwells equation at localized cross sections, the algorithm decomposes the electromagnetic fields as a sum of local eigenmodes [32]. Then each computed section is joined together by the use of scattering matrices that relates incoming and outgoing waves at one cross section. The scattering matrices are products of the continuity in Maxwell's equations that has to be satisfied at the section boundaries. If the complete set of eigenmodes is calculated, a scattering matrix for every component can be easily found.

The most important advantage of the eigenmode expansion method is that it is based on a rigorous solution to Maxwell's equations, only limited by the finite number of modes used in the expansion and inevitable numerical errors in the im-

plementation. Furthermore, simulations solves for both TE and TM modes in the same calculation because the s-matrix technique provides the solution for all inputs [33]. The drawback of this approach is that the time complexity scales cubically for increasing area of the computed cross section ($O(N^3)$). On the other hand, the scattering matrix approach of the EME method is very well suited for periodic or long structures since the s-matrix of repeating units can be re-used giving the time complexity $O(\log(N))$ for periodic structures.

Chapter 3

Simulation and Fabrication Tools

This chapter presents the tools that were used for this thesis. Simulation software and associated capabilities will discussed first and the instruments used for fabrication and characterization will be presented subsequently. The main idea of introducing the various tools early on is to provide the reader with a useful foundation before being presented the experimental procedure.

3.1 Simulation software

The simulation software is presented relatively briefly because the underlying mathematical methods were introduced in Section 2.7. Additional details will be discussed consecutively in the description of the experimental procedure as certain details are easier to comprehend through the use of an example.

MIT Photonic bands

MIT Photonic Bands (MPB) is a freely available open-source software package for solving frequency-domain eigenproblems in electromagnetics. Even though the package's intended application was the study of periodic dielectric structures, so-called photonic crystals, it applies well to compute optical dispersion-relations and eigenstates of simpler structures. To compute the dispersion relation of a waveguide using MPB, one would first need to construct a computational model of the waveguide and specify the relevant material and boundary conditions. The software would then solve the electromagnetic eigenvalue problem for the waveguide and compute the dispersion relation of the electromagnetic modes supported by the waveguide.

One of the main disadvantages of using MPB is that it is not specifically designed for computing the dispersion relations of waveguides. While it can be used for this purpose in some cases, other software tools may be better suited. Additionally, the computational demands of MPB can be quite high, especially for larger and more complex structures. This can make it challenging to use the software on systems with limited computing resources, such as laptops or small computing clusters.

A comprehensive tutorial describing the specifics of working with MPB can be found at [34].

Lumerical MODE

Lumerical MODE is an optical waveguide and coupler solver developed by the American software company Ansys [35]. It offers high-accuracy waveguide simulations through Finite Difference Eigenmode solver, a variational FDTD solver and a bidirectional EME solver. As this project is considering periodic structures, the EME solver is highly suitable due to reasons discussed in Section 2.7.2.

In contrast to MPB, Lumerical MODE offers an easily operated user interface to help perform the simulations. The software's graphical user interface (GUI) displays the simulated structure, ports and computational cells as each element is added by the user. Once the setup is finalized, the simulation is executed and the software transitions to analysis mode. Within this mode, users can conduct helpful parameter sweeps and modify specific sections of the structure. The propagation sweep is particularly useful because it allows the results for a range of spans to be calculated fairly accurate without recalculating the modes at each cell [36]. The wave Ansys' webpages offer very useful tutorials which can be found at [37].

3.2 Fabrication and Characterization Instruments

This section describes the instruments used for fabrication and characterization. Instrumental setups are presented and important parameters are discussed. Certain physical principles involved in each method are also described. The level of detail is chosen to provide sufficient understanding of the working principles of each method and is deemed necessary for comprehending arguments presented in following chapters.

3.2.1 Electron Beam Lithography

Electron Beam Lithography (EBL) is a nano-fabrication technique that utilizes a focused beam of electrons to write patterns onto a sample covered by a radiation sensitive resist by selectively changing its solubility. To accurately control the writing process, the technique typically involves a Scanning Electron Microscope (SEM) integrated into a lithography system [1]. EBL was developed as a consequence of the increasing industrial need for submicron devices that appeared in the 60's. Unless otherwise specified, the information regarding EBL is gathered from [38].

The EBL process consists of three steps: exposure, development and pattern transfer. First, the sample has to be covered by a so-called electron beam (e-beam) resist. The resist is usually an organic polymer that will become more or less soluble when exposed to high-energy electrons. A *negative* resist will initiate cross-linking of the organic molecules upon exposure yielding non-soluble resist at exposed areas. The exact opposite occurs in the case of *positive* resists. Here, the electron beam will induce the breaking of molecular bonds so that exposed areas become more soluble. The terms "positive" and "negative" are associated with the visual features of the exposed pattern compared to that of the final pattern after successive fabrication steps involving deposition and removal of material.

[1] The SEM-instrument will be presented in section 3.2.3

For exposure to occur, the electron beam has to be produced by some form of emitter. For high resolution requirements, this emitter typically consists of a field emission source based on a single crystal tip. The beam is then focused by electromagnetic fields onto the resist-covered sample to function as the tip of a pencil. Being a maskless process, the exposure is rather time consuming and not suited for high-volume industry applications. However, the technique is excellent for research purposes due to its flexibility and superb resolution below 10 nm [39].

Instrumental setup and writing mechanism

The EBL system consists of two parts; the electron-optics and the high precision stage located above it. The electron optics consists of an electron source that creates the electron beam that is controlled by a beam blanker, aperture and beam deflector so that it exposes the stage in accordance with the design the system is given.The beam blanker turns the beam on and off by deflecting the beam away onto the aperture.

The writing field refers to the largest area that is exposed without the stage movement. Within the writing field, the e-beam is deflected to expose the pattern inside. Each writing field is then further divided into subfields and the patterns within a subfield are divided into trapezoids. Each trapezoid is filled by an array of e-beam shots, or dots, which determines the resulting exposure quality. The spot size and step size of these e-beam shots is what determines the level of detail possible to write successfully with the system.

The beam spot size is increased with increasing beam current and aperture, and decreased with increasing acceleration voltage. These parameters are chosen depending on the size of the feature that is written. The shot pitch, referring to the distance between two adjacent beam spots that can be exposed, is defined by setting the beam position resolution given by the field size divided by number of dots. The shot pitch is then some multiple of the beam position resolution.

Resolution limiting mechanism

An important characteristic of an EBL process is the resolution, i.e. the minimum feature dimension that can be precisely transferred to the resist film [40]. The resolution depends heavily on the diameter of the beam, which again depends on the energy spread the electrons and acceleration voltage. Low voltages might amplify existing aberrations of the microscope which yield a lower resolution. Furthermore, the interaction between the beam and resist also gives rise to limitations such as the proximity effect. A non-zero exposure dose of the resist area outside of the target area is unavoidable due to forward and backscattering electrons generated upon collision between beam and resist. Backscattered electrons of high energy will again generate secondary electrons along their traveling path leaving exposed resist far from the original incident point.

The result of considerable proximity effects on positive e-beam resists differ from that of negative resist. In the former case it leads to excessive resist removal, while the latter leads to an undesired excess of resist in the form of side lobes. The proximity effect can be reduced by increasing the beam voltage or by utilizing EBL software to simulate the effect and make appropriate dose and design corrections.

If a pattern is larger than the writing field, it has to be divided into multiple fields and the stage has to move in between writing fields. Consequently, if the writing fields are not aligned properly, stitching errors will occur. These errors increase with the size of the writing field because the magnitude of the beam position error increases as the beam is deflected further away from the column axis. This is often mitigated by performing field correction prior to exposure.

Another source of error occurs for non-uniform sample heights. A large sample inclination leads to deflection scale error caused by the change in sample height. To make the sample as flat as possible, it is important to clean it thoroughly on the backside.

Pattern Development

Another important step for achieving a high resolution in the EBL process is the development that follows exposure. This is the step where the soluble parts of the e-beam resist is selectively removed from the sample. This is usually done by immersing the sample in an appropriate developer and slightly agitating the reaction by stirring. The resulting pattern depends on whether positive or negative resist was coated onto the sample surface as shown in figure.

3.2.2 Inductively Coupled Plasma-Reactive Ion Etching

Inductively coupled plasma-reactive ion etching (ICP-RIE) is a commonly used dry etching technique that achieves high etch rates, highly anisotropic material removal and process flexibility [41]. The etch-mechanism combines both reactive chemical and physical processes by using ion bombardment at low pressure. The discussion on the ICP-RIE technique is based on [40].

It is based on an inductively coupled plasma (ICP) reactor that generates high-density plasma from inductive coupling between a radio frequency (RF) antenna and the plasma. An RF magnetic field is generated by a spiral coil separated from the plasma by a dielectric plate or quartz tube. The magnetic field serves to densify the plasma to enable acceptable etch rates at lower pressure. Positive plasma ions are then accelerated toward the sample by an RF electric field powered by a strong DC bias. In essence, the density of the generated plasma is governed by the ICP power and associated magnetic field, while the energy of the ion bombardment is powered by the capacitively coupled plasma (CCP) and associated electric field.

Dry etching mechanism

The etching action in dry etch systems, such as the ICP-RIE, is a result of either a physical or a chemical process or a combination of the two. A purely *physical* mechanism involves the bombardement of positive non-reactive ions onto a the sample surface by strong electric fields. The collision causes the ions to physically remove unprotected parts of the sample surface material in what is called a sputter etch action. The mechanical etching mechanism gives a high etch rate and strong etch directionality which yields a highly anisotropic etch profile. The drawbacks, however, include poor selectivity and unwanted deposition of sputtered material. In contrast, *chemical* etching processes result in an isotropic etch profile. In this case, the plasma creates free radicals and reactive atoms that chemically react with the

sample surface. By utilizing carefully selected gases in the process, it is possible to attain a very high selectivity that minimizes unwanted reactions with the resist or underlying substrate. Silicon based devices are often etched by fluorine and chlorine plasmas such as SF_6 and CHF_3 [42].

The integration of both etching procedures allows for the mitigation of the aforementioned limitations and the utilization of their respective benefits. In this context, the chemical etching process is improved through ion bombardment, enabling enhanced control over the etch profile. Manipulation of the plasma conditions and gas composition can control the degree of anisotropy, while simultaneously ensuring adequate selectivity. Increased ICP power will increase the ion density to generate an etch that is more chemical, while an increase in CCP power increases the enegry of the ions, yielding an etch of a typically physical character. Moreover, the magnitude of the physical or chemical etching phenomena can be effectively governed by the orientation of the electric field relative to the surface of the sample. For instance, if the field is aligned parallel to the sample surface, the mechanism would be predominantly chemical, as sputtering becomes unlikely to occur.

Etching parameters

A very important characteristic of an etching procedure is the shape of the sidewall of the etched feature, also referred to as the etch profile. The two basic etch profiles, isotropic and anisotropic, are results from the directionality of the etch during the process. An *isotropic* etch profile is obtained when etching occurs at the same rate in all directions, leading to an undercut of the etched material under the mask. This profile is generally undesirable for submicron devices because it leads to loss of linewidth.

On the other hand, *anisotropic* etching profiles is characterized by a unidirectional etching rate perpendicular to the sample surface. The result is vertical sidewalls that permits a high packing density of features. This is obtained by most dry etching methods and is desirable for small scale devices, and especially submicron waveguide structures. Deviation in etch angles will result in altered group velocity, transmission loss, bend loss and polarization coupling [43].

3.2.3 Scanning Electron Microscopy

Scanning electron microscopy (SEM) is a microscopy technique that utilizes a focused beam of electrons to generate high-resolution images of the surface of a sample. Electrons have significantly smaller wavelengths than visible light, which enables the examination of atomic-scale objects that are unobservable in optical microscopes. This section is based on chapter 5 of Springer's "Physical Principles of Electron Microscopy" [44].

Instrument setup

For an operational scanning electron microscope (SEM), an electron gun is essential to produce a stream of electrons. This is done by a either a field emission gun that utilizes a high electric field, or thermionic filament that thermally emits electrons for high temperatures. These electrons are subsequently attracted and shaped into a coherent beam by a positively charged anode positioned beneath. Controlling the

size of the beam, which directly influences the resolution of the resulting image, is achieved with condenser lenses. Furthermore, the scanning component of an SEM is governed by scan coils, which deflect the electron beam along the surface of the specimen. Finally, the beam reaches the objective lens, responsible for focusing the electron beam onto the sample. It is worth noting that all lenses employed within the SEM system are composed of electromagnetic coils, generating magnetic fields that act upon the electrons.

Penetration of electrons into a solid

Accelerated electrons that collides with a sample will interact in different ways that gives different kinds of information. The collision generates other electrons, photons and irradiations. The most important of which are *backscattered electrons* (BSE) and *secondary electrons* (SE).

If the incident electrons are elastically scattered with a deflection angle larger than 90°, it is said to be backscattered. As the scattering is elastic, meaning no considerable loss of energy, the resulting electrons have a significant probability of being collected inside the surrounding vacuum. The collected BSE are then used to generate an image of the sample surface. BSE originate from deeper areas of the sample and display high sensitivity for the distribution of various elements that make up a sample. This is a consequence of the high-energy scattering mechanism that allows deeper electrons to escape the sample where heavier elements with deflect incident electrons more strongly. Thus, heavier elements appear brighter than lighter elements on the SEM image yielding a high *elemental* contrast.

Another type of electrons that can be utilized to generate an image of a specimen, are SE. Unlike BSE, they are products of inelastic scattering of the incident electrons. In this case, when the incident electrons collide with the weakly bound valence electrons of the sample, the energy is transferred and used to release them from their confinement and give them kinetic energy to travel through the sample as SE. However, the SE may escape into the vacuum if they were created close to the surface ($< 2\,\text{nm}$). The SEM image resulting from SE will therefore display high *topographical* contrast.

Resolution Limiting Mechanisms

The primary objective of operating a scanning electron microscope (SEM) is to obtain high-resolution images. Nevertheless, it is important to acknowledge the limitations that restrict the level of achievable resolution, as well as associated trade-offs.

Similarly to the resolution discussion of the EBL in section 3.2.1, the resolution of SEM is dictated by the diameter of the incident electron beam. The probe size is reduced by the help of condenser lenses, but this reduction also reduces the beam current which disables the imagery. Furthermore, higher accelerating voltages can provide higher resolutions as the incident electrons are allowed to penetrate deeper into the sample and generate more BSE or SE [45]. The drawback is that high-energy electrons can also potentially damage the sample. In short, the parameters that yield optimal image results depends on the inspected sample and features of interest.

Chapter 4

Experimental Simulation Procedure with MPB and Lumerical

The experimental procedure of the simulations conducted in this thesis is two-fold as two different simulation methods are utilized. First, MPB is used to simulate LPG couplers in order to obtain dispersion relations that are used to calculate sensitivities. Focus is put on finding geometries that achieve high *sensitivity* for a wide operation range. Second, the geometries that satisfy the aforementioned requirement are subject to *transmission* simulations to find the correct grating period required for coupling.

Two generic designs, the single and double LPG coupler, are of interest. For each simulation software, the single LPG coupler will be considered first, followed by the double LPG coupler. As Lumerical simulations depend heavily on the findings from MPB, MPB will be presented first.

4.1 MPB simulations of single LPG coupler

MPB simulations for a single LPG coupler were conducted during the preliminary work, but the procedure is included because it is a prerequisite for simulating double LPG structures. The objective is to simulate a silicon on insulator waveguide that is immersed in water and is assumed to be infinitely long. By simulating such a structure, it is possible to calculate the propagating modes and corresponding dispersion relations, which can provide all of the necessary information to compute the effective refractive index, group velocity, coupling grating period and sensitivity. The simulation procedure is based on the tutorials provided by Arvadan Oskoii as part of a two-day symposium hosted by the Boston University Photonics Center [46].

Device Geometry and Simulation Parameters

The device consists of three main components in addition to the surrounding environment: a strip waveguide (core) on top of an oxide layer, which sits on top of a substrate. To ensure strong mode confinement throughout the structure, it is necessary for the refractive index contrast between the core and oxide to be large.

For this reason, the materials used are silicon (Si) and silicon dioxide (SiO_2). The evanescent fields in such a structure decay exponentially into the oxide layer, allowing the substrate to be omitted during simulations. The surrounding cladding is modeled by setting the default material of the simulation to the refractive index of water, which is chosen to ensure relevance for biosensor applications. Table 4.1 lists the functions and refractive index at $\lambda = 1.55\,\mu m$ of the materials discussed, and Figure 4.1 illustrates the geometry and computational cell. The waveguide core has a width of $w = 0.5\,\mu m$ and a height of $h = 0.22\,\mu m$. Important parameters and their functions are listed in table 4.2. The thicknesses of the water and silicon dioxide layers are not included in the list of parameters because the confined mode is expected to be highly concentrated within the core of the waveguide. The cladding layer and oxide layer only need to be thick enough to ensure that the confined mode decays to negligible values as the computational region is truncated. This assumption is validated through convergence tests with varying cladding thickness or computational cell size.

Material	Function	Refractive index
H_2O	cladding	1.31
Si	core	3.47
SiO_2	oxide	1.44

Table 4.1: Materials and associated function and index that was used in the simulations.

As far as dimensions are concerned, only the height and width of the silicon core are of interest as the waveguide is considered to be infinitely long. The height h and width w is set to $0.22\,\mu m$ and $0.50\,\mu m$, respectively. This is a well-known geometry for silicon-on-insulator waveguides chosen for its low propagation losses and single-mode operations at infrared wavelengths around $\lambda = 1.55\,\mu m$ [47].

In addition to the device itself, the computational cell has to be defined with associated resolution. The device geometry is set so that the modes propagate in the x-direction where the waveguide is translationally invariant. This enables a 3D calculation based on a 2D computational cell in y and z. To ensure accurate *and* efficient computations, a convergence test should be performed for the cell size and resolution. It is recommended to set resolution to a power of two for slightly faster processing.

Mode calculation, Coupling and Sensitivity Determination

Once the geometry has been defined, all of the necessary parameters can be input to the MPB modesolver that will run the simulation. MPB allows the user to choose whether to solve for TE modes, TM modes, or both. As the setup of the available laser laboratory offers a TE polarized light source, only TE modes will be considered in this study[1]. However, the same experimental procedure could be applied to TM modes as well.

[1]The polarizer can be adjusted to TM modes as well, but it is more convenient for all users if it is kept constant at TE.

Parameter	Value	Description
w	0.5	Width of waveguide core
h	0.22	Height of waveguide core
sc_x	0	Computational cell x-direction size
sc_y	2	Computational cell y-direction size
sc_z	2	Computational cell z-direction size
resolution	32	Pixels per length unit
k_{min}	0.1	Lower wavector limit
k_{max}	3	Upper wavevector limit
k_{num}	100	Amount of wavevectors to compute
N_{bands}	2	Number of modes to calculate
k_{dir}	x-direction	Direction of the k-vectors to be computed
f_{mode}	1/1.55	Frequency of interest
$kmag_{\text{guess}}$	3.45 f_{mode}	Initial guess for the magnitude of k to be computed
$kmag_{\text{min}}$	0.1 f_{mode}	Lower range limit of k magnitudes to search
$kmag_{\text{max}}$	4.0 f_{mode}	Upper range limit of k magnitudes to search
tol	1e-6	Tolerance of convergence

Table 4.2: Simulation parameters grouped by function. The length unit is microns.

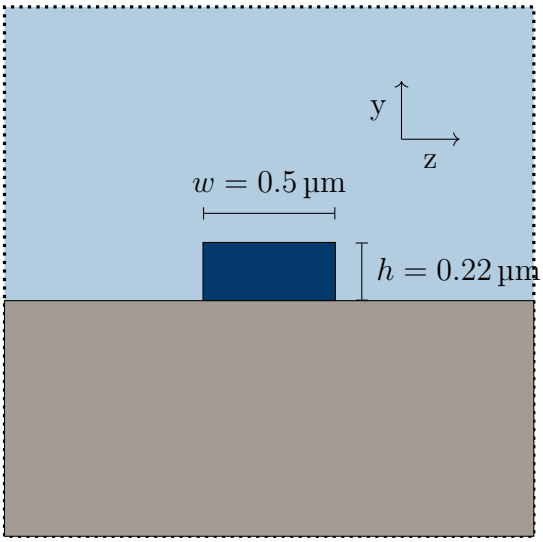

Figure 4.1: Geometry and computational cell of the simulated waveguide in the yz-plane. The dark blue rectangle represents the silicon core which sits on top of the silicon oxide surrounded by water. Each material in the design is given a color grading that represents the value of their respective refractive index. Darker colors have a higher refractive index. The dotted line that surrounds the entire design is the computational cell.

Once the dispersion relation has been calculated, the effective refractive index can be found using Equation (2.31). MPB uses an inverse calculation and Newton's method to find the propagation constant that corresponds to a given mode frequency. This process requires the user to provide tolerance and initial values, which may require some trial and error. The values used for this project are listed in Table 4.2.

With the effective refractive indices for all modes available, the grating period for coupling between asynchronous modes can be found using Equation (2.46).

Calculating the sensitivity is slightly more involved, as it requires both (1) the group indices and (2) the change in the effective refractive index with respect to the cladding index for the two modes, as written in Equation (2.47). Both of these quantities depend heavily on the wavelength, but not necessarily the same set of wavelengths. Therefore, numerical interpolation is required to incorporate both quantities into the same expression for sensitivity. The results will be sufficiently accurate as long as the number of wavevector k-points is large enough.

(1) can be calculated relatively easily using the group velocity provided by the MPB simulation. (2) must be solved numerically by calculating the effective refractive index for a range of cladding indices and using a suitable numerical differentiation algorithm. The Python package NumPy is a highly recommended tool for such numerical analysis [48], but the reader is also encouraged to try a simple finite difference method and compare the results. In this project, four sets of frequencies, corresponding to the k-points, were calculated to find this derivative. Two of these were related to mode 1 and 2 with n_{clad}, and the other two were related to mode 1 and 2 with $n_{clad} + d$, where d is some infinitesimal increase in the refractive index.

4.2 MPB Simulations of Double LPG Coupler

Extending our coupling design to two waveguides as illustrated in figure 2.7 opens up a larger range of opportunities. A double waveguide design is based on the same principles of coupling as for the single SOI waveguide. However, instead of having the fundamental mode coupling to a higher order mode, the coupling occurs *across* the two waveguides. I.e. the fundamental mode of waveguide 1 couples to the fundamental mode of waveguide 2. The goal of the design is to maximize sensitivity for a range of wavelengths around 1.55 µm. Maxwells equations are scale invariant so the phase matching turning point where the sensitivity is infinite can be altered by changing geometry. With two waveguides, there are now four geometric parameters available for tuning: width and height for the two waveguides.

Also, the single waveguide design restricted the geometry to be single-moded. This restriction does not necessarily apply to both waveguides in the double structure. During coupling, all optical power is transferred away from the initial waveguide. Whether the signal is distributed onto multiple modes of the second waveguide or into the cladding is irrelevant as long as it directed away from the initial waveguide so that the output transmission is zero.

Device Geometry and Simulation Parameters

As the two waveguides in this structure are simulated separately, the resulting geometry for each waveguide is similar to that of the single waveguide. Figure 4.2 shows a cross section of the double waveguide structure and the materials used for the simulations are listed in table 4.1. w and h were set to the predefined values 0.5 and 0.22 µm during the single waveguide experiment, but for this case the goal is to investigate the a large set of geometries and find the dimensions that produces the best sensitivity.

Other parameters shown in table 4.2 are kept the same, except for N_{bands} that is set to 1 to restrict the analysis to the coupling between fundamental modes and avoid the software to return wrong values for frequencies where different modes intersect[2].

[2]This was an issue that occurred in the preliminary work.

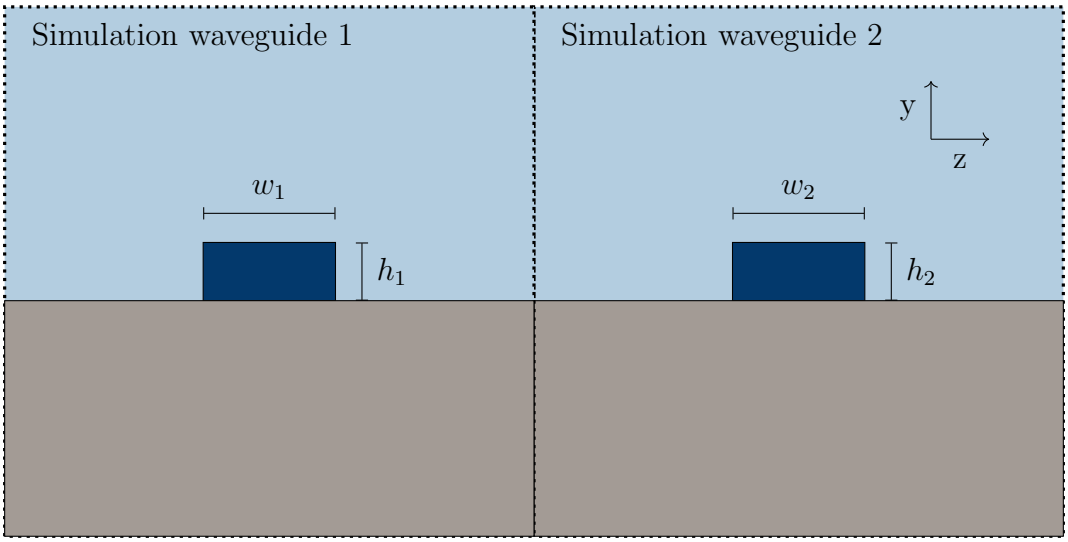

Figure 4.2: Geometries and computational cells of the double waveguide simulations in the yz-plane. The color grading is the same as for figure 4.1, but each waveguide is simulated separately as indicated by the dotted line that shows the computational cell for each waveguide.

Calculating Sensitivities for Optimal Wavelengths Around 1.55 µm

The mathematical approach for calculating sensitivities of the double waveguide structure was the same as for the single waveguide due to separate simulations of the double structure. For any given geometry, the group index difference and derivatives of effective index of each mode with respect to the cladding index are calculated first and numerical interpolation are utilized to calculate sensitivities.

The goal of this part of the study is to find a double waveguide geometry that yields the highest sensitivity at wavelengths around 1.55 µm. Quantifying "high" sensitivity is therefore paramount. The most intuitive way would have been to simply compare sensitivities for $\lambda = 1.55\,\mu\text{m}$ and choose the structure that yields the highest one at this value. That way, the best structures would be those with $n_{g1} = n_{g2}$, i.e. structures where the PMTP appears at $\lambda = 1.55\,\mu\text{m}$ and the sensitivity is theoretically infinite. The problem is that such an approach omits a lot of important information. Although the sensitivity spikes at the right wavelength, it might drop just as quick in immediate proximity. Therefore, the sensitivity has to be analyzed and compared for a range of wavelengths around 1.55 µm to get a better understanding of "good" and "bad" sensitivities. A design that is able to uphold a high sensitivity for a sufficient operating range is greatly improved.

Optimizing Simulation efficiency and Accuracy through Parameter Adjustment and Device Restrictions

In order to optimize the computational efficiency and accuracy of simulations, it is important to carefully adjust parameters and variable ranges. Previous convergence tests can be useful for this purpose, but also a rough investigations of how sensitivity responds to changes in geometry. This ensures that the sensitivity analysis is focused on ranges of widths and heights that are known to produce meaningful results, rather than wasting time and computational resources on suboptimal geometries. Such an

Parameter	Range	Count	Description
w	0.4-0.7 µm	10	Width of waveguides
h	0.20-0.40 µm	10	Height of waveguides
λ_s	1.45-1.65 µm	10	Wavelengths for which sensitivity was calculated

Table 4.3: Parameter range and count for sensitivity computations.

investigation is conducted for this project as well. The geometry of one waveguide is kept constant, while the other was varied in width to identify an appropriate range of widths to use in the final simulations. Upper and lower limits are determined to restrict the number of possible propagating modes to 2.

However, even two modes might cause issues in the device. If the second mode of waveguide 1 overlaps with the fundamental mode of waveguide 2 at operation wavelength, waveguide 1 might couple to its own second order mode instead of the fundamental mode of the other one. This can potentially inflict disturbance in the overall transmission if the second mode in question is a guided mode. Therefore, another restriction is imposed on the optimal design. Namely that there should be no significant overlap between the modes that might interfere with the transmission. The tolerance for this overlap is set to 0.1 µm.

Additional restrictions are also imposed on the design for practical reasons. Fabricating one device that consists of different heights is cumbersome and inefficient because it requires more lithography steps. If the two waveguides are to have different heights, the structure would have to be go through sample coating, exposure, development and etching twice. Therefore, the two waveguides in the double LPG coupler design are restricted to have identical heights $h_1 = h_2 = h$.

To find the design with the highest sensitivity, ten equidistributed widths are combined with ten equidistributed heights around 0.5 µm, and the sensitivity at ten equidistributed wavelengths around 1.55 µm is calculated for each design. These values are then added together and compared to determine the design with the best overall sensitivity. Best overall sensitivity refers to the design that has the highest accumulated sensitivity over the wavelength range λ_s shown in Table 4.3. The table also shows the different height and width values that were tested during the simulations.

Two experimental approaches were conducted to identify geometries with the highest sensitivity:

A Calculate sensitivity for structures of different widths where the height is a constant so that $h_1 = h_2 = h = 0.22$ µm.

B Calculate sensitivity for different structures where both height and width varies through combinations.

Each approach will yield one geometry that performs best in terms of sensitivity. These will be labeled design A and B, respectively.

The 0.5×0.22 µm is a conventional waveguide design used extensively in SOI integrated photonics due to single-mode operation, side wall roughness and low propagation losses in Si [47]. By keeping the waveguide height constant, the resulting device would be highly compatible with existing fabrication techniques in the

industry. Lithography recipes can be kept the same and the only change necessary is that of the design mask. Keeping the height constant also simplifies calculations considerably due to fewer variables.

Nevertheless, the highest sensitivity is most likely found by adjusting three parameters within the parameter range rather than two. Approach B is therefore also included in the experimental procedure. Both methods are then subject to comparison where the resulting designs must be evaluated in terms of manufacturability as well as sensitivity.

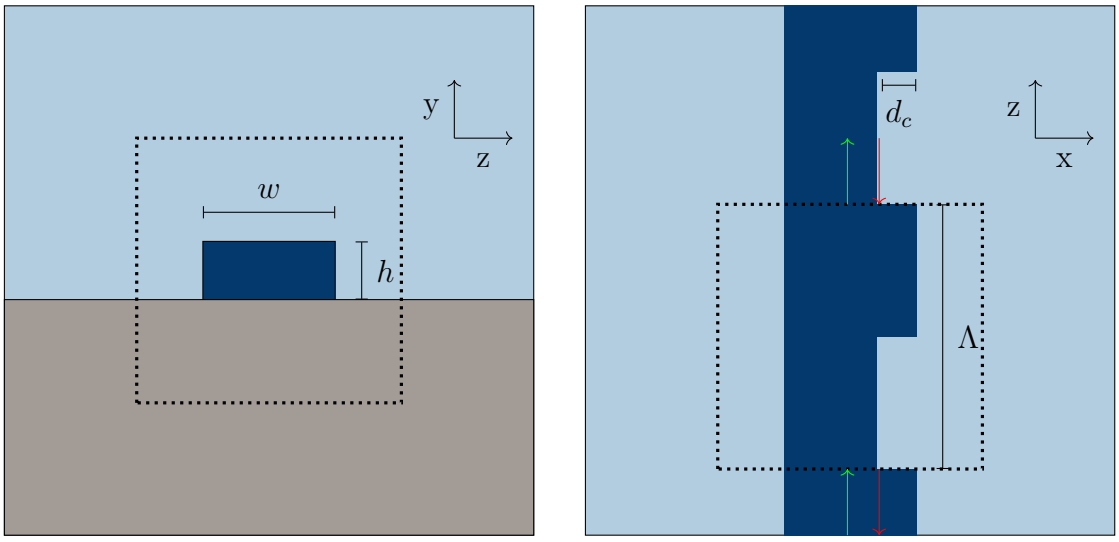

(a) (b)

Figure 4.3: a) Cross section schematic of the single LPG coupler that is being simulated in Lumerical. It is identical to that which was simulated with MPB. b) Schematic of the xz-plane of the same device and relevant dimensions such as the grating depth d_c and grating period Λ. The dotted line in a) and b) indicates the definition of the solver region, which also equals a cell group with one cell.

4.3 Lumerical Simulations of Single LPG Coupler

This section presents the experimental procedure of the EME simulations that were performed on the single LPG coupler in Lumerical. The focus of this section is to investigate the transmission properties of the $0.5 \times 0.22\,\mu m^2$ single LPG coupler that was simulated during the preliminary work.

Single LPG Coupler Setup

Similarly to the modal simulations described previously, the structure of interest has to be built and the parameters have to be set correctly before any simulations can be performed. The target is to build the same structure as was simulated in MPB. That is a silicon waveguide on top of an oxide layer immersed in water with width $w = 0.5\,\mu m$ and height $h = 0.22\,\mu m$. The refractive indices remain the same and the substrate is also omitted from the design as the propagating mode is assumed to be strongly confined withing the waveguide core.

Nonetheless, there is a very important difference with regards to the transmission simulations. In MPB, only the height and width were of interest. Additionally, the grating was never incorporated into the design because MPB is simply a tool for calculating the dispersion relations. The sensitivity and as the goal was not to investigate transmission properties, but to compute modes of interest.

The transmission simulations, however, will be conducted three dimensional so that the length of the waveguide and grating are of utmost importance. The EME solver in Lumerical MODE offers a neat way of dealing with periodic structures. Instead of designing the whole structure, only one unit cell needs to be defined as shown in the setup presented in figure 4.3b. The unit cell consists of one waveguide

of width w and a successive waveguide of width $w - d_c$, where d_c is the grating depth. The solver region is then defined with the same length as the unit cell equal to the desired grating period, and a width and height that confines the structure similarly to the computational cell from the MPB simulations. At each end of the solver region, ports are set up to calculate transmission and reflection at the solver region boundaries, as shown by the red and green arrows in figure 4.3b. Next, the solver region has to be divided into groups and cells based on the cross section and desired modal solutions in each cell. In this case, it is favorable to define the unit cell as one cell group because this will allow for an efficient EME propagation sweep for a range of unit cell lengths during analysis. Also, only the fundamental mode is considered as the 0.5x0.22 Si waveguide is single mode and involving higher order modes would be computationally inefficient.

Next, the grating is created by setting the periodicity of the cell group to some desired value N meaning the unit cell will be propagated N times during the simulations. The grating is chosen to be asymmetric, meaning that it only appears on one side of the grating. The asymmetry enables the propagating mode to couple to asymmetric modes [49]. Symmetric and asymmetric modes refer to the electromagnetic field distribution inside the waveguide and whether or not it is in phase with respect to the center of the waveguide [50]. Higher order even modes, such as the second order, are asymmetric and thus require an asymmetric grating for coupling.

Moreoever, the grating depth, d_c, was set to 0.1 µm, which is slightly larger than what was used experimentally by Høvik et al. The goal of these simulations are not to optimize the structure in terms of loss and noise, but rather identify the required grating period for coupling around $\lambda = 1.55$ µm as a starting point for fabrication. A greater grating depth yields a higher coupling strength, which makes it easier to investigate the coupling.

The most important parameters are listed in table 4.4.

Parameters Subject to Analysis

As the setup is complete, the next step is to decide what to simulate and analyze. MPB simulations of a single LPG coupler was conducted in unpublished preliminary work, but the most important findings, such as the required grating period for coupling, will be presented in the results section. Thus, a propagation sweep that calculates the transmission for a set of grating periods executed in Lumerical will serve to verify previous findings and provide further insight in the LPG structures

As the setup is complete, the next step is to decide what to simulate and analyze. Previous analysis from the project report predicted that a grating period of 1.48 µm at $\lambda = 1.55$ µm would lead to coupling between the fundamental mode and cladding mode. To verify this theory, a propagation sweep of different grating periods around 1.48 µm at $\lambda = 1.55$ µm is performed and analyzed.

4.4 Lumerical Simlations of Double LPG Coupler

This section presents the experimental procedure of simulating double LPG couplers using EME methods with Lumerical. The focus of this section is to investigate the transmission properties of couplers that obtained high sensitivity from the MPB simulations.

Parameter	Value	Description
background index	1.31	Refractive index of surrounding water
wavelength	1.55	[µm]
number of modes in cell groups	2	Modes to solve for in all cells
number of cell groups	1	Cell groups in solver region
start cell group	1	First cell group in the periodic section
end cell group	1	Last cell group in the periodic section
cells	2	Cells in the cell group
periods	N	Repetitions for the cell group
conserve energy	True	Interface S-matrix norm forced to 1

Table 4.4: Most important simulation parameters used during simulations

Double LPG coupler setup

The transition from a single LPG coupler to a double LPG coupler structure is explained in section 4.2 regarding the MPB simulations. The design is improved by the introduction of an additional waveguide placed in parallel to the LPG. An important concept in MPB was that each waveguide was simulated separately and the resulting dispersion relations were used to calculate important characteristics. The transmission simulations that are conducted in Lumerical, on the other hand, will confine the whole structure within the solver region, including both waveguides and the grating as shown by the dotted lines in Figure 4.4 which will be explained below. As the double LPG coupler utilizes a symmetric design with a grating on both sides of the waveguide, the grating depth was set to 0.05 µm on each side.

The rest of the setup is similar to that of the single LPG coupler structure. All parameters from 4.4 were kept the same, so certain pre-simulation configuration details will not be presented to avoid repetition.

Parameters Subject to Analysis

However, there is an important difference in the double LPG coupler design that needs to be addressed. The single LPG coupler was designed to couple the fundamental mode to the second order "lossy" cladding mode. This requires an asymmetric grating due to the asymmetric phase mismatch of the electromagnetic field in the second mode. In contrast, the double LPG coupler design aims to couple between the symmetric fundamental modes of the two waveguides, thus requiring a symmetric grating. Figure 4.4a and 4.4b shows the design for an asymmetric and symmetric double LPG coupler, respectively.

As the simulations consider the total structure, an additional parameter of great importance is introduced to the problem. Namely, the distance between the two waveguides, denoted as d in figure 4.4. From coupling theory, the spacing between the two waveguides, as well as the grating length, governs the resulting coupling strength [49]. In general, a longer coupling length is required for larger spacings [51].

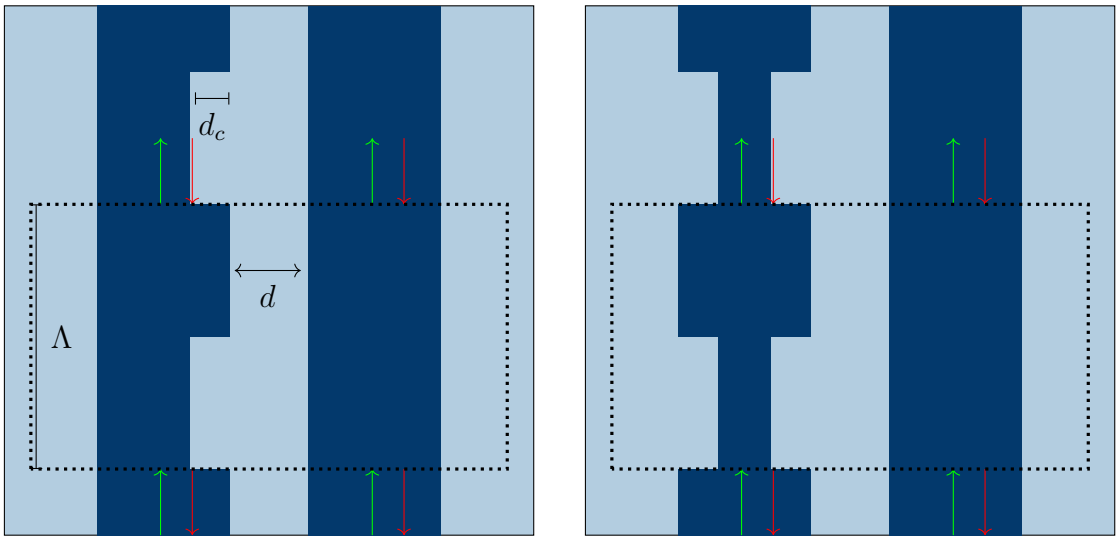

(a) (b)

Figure 4.4: Schematic of the asymmetric (a) and symmetric (b) double LPG coupler design that are simulated in Lumerical. Both designs separate the two constituting waveguide by spacing d. The dotted line indicates the solver region and cell group that is being repeated throughout the simulation. Ports are set on each end of the solver region at both waveguides, indicated by the red and green arrows.

Analytical calculation of coupling coefficients for long period gratings is a rather cumbersome endeavour and experimental results have been found to coincide poorly with theory [52]. Furthermore, the overall coupling will also depend on the grating depth, which leaves many parameters to include in the analysis. The investigation of appropriate parameters is in many ways results in itself and is therefore included and discussed in further detail in the section 8.2. In summary, the correct spacing is found by inspecting transmission plots for increasing spacings and identifying the spacing that yields the most distinct and sharp resonance peaks. The sharpest peak is then subject to further analysis and plotted for varying coupling length. The length that yields the highest resonance is chosen for final fabrication.

The dimensions of the waveguides that are subject to the Lumerical simulations are determined by the results from the MPB simulations. The designs that yield the best sensitivity from approach A and B will be considered in terms of transmission properties. To investigate the coupling between the waveguides, two ports need to be located at the ends of each waveguide yielding a total of four ports for each simulated structure. The transmission and reflection of the modes are calculated at these ports. By injecting any chosen mode into a single waveguide and measuring the response for each waveguide separately, the user can determine the power that is coupled between the waveguides.

Chapter 5

Fabrication and Characterization Procedure

The primary motivation behind the fabrication process is to create physical devices based on the previously simulated structures and evaluate how their coupling abilities align with the findings from the simulations. This iterative process involves fabricating successive chips, each one being an optimized version of the previous chip.

Three different devices are fabricated: the single LPG coupler, asymmetric double LPG coupler and symmetric double LPG coupler. These devices are fabricated with different coupling lengths and grating periods varying in the vicinity of the target values calculated from simulations in MPB and Lumerical. Any discrapencies observed between the two simulation methods is also addressed in the fabrication to confirm or disprove the simulation analysis.

Two individual samples are fabricated to accommodate the three types of devices. The first sample exclusively features single LPG couplers, designed based on the results obtained from the MPB simulations. On the other hand, the second sample incorporates all three types of devices and is designed by considering the results from both MPB and Lumerical simulations. Furthermore, the second sample is optimized to address the shortcomings observed from the characterization and measurements of the first sample.

Both samples undergo the same fabrication procedure, which will be presented in this section.

5.1 Generic LPG coupler design for practical considerations

Simulations of LPG couplers are useful, but the fabrication of physical devices in the real world introduces factors that will create discrepancies with respect to the theory. The lithography procedure that is to be presented cannot be executed perfectly. Some instrument parameters might not reach the exact set value and the fabricated structure will not be an exact copy of the initial design in terms of dimensions. The sum of all such inaccuracies and uncertainties will give the final structure slightly different characteristics from simulations. Therefore, each design that is fabricated in this project will be fabricated in an array that varies important

coupling parameters around the target value that is expected to provide meaningful results. Nevertheless, all waveguides within each array have several attributes in common which will be presented here.

Input Sections and Adiabatic Tapers

There are several practical concerns that have to be addressed as the LPG coupler designs are fabricated into physical devices. First of all, the ends have to be cleaved to enable light coupling and transmission measurements. This means that each end of the devices has to be extended into an "Input" and "Output" section to create wide areas for which the cleavage can be executed. These sections are denoted at the beginning and end of the schematics in Figure 5.1 and Figure 5.2. As the fiber ends used for coupling are much larger than the dimensions of the waveguides, the input and output sections have an increased waveguide width of 5 µm to simplify alignment and increase the amount of light that is coupled. It should be noted that the output and input waveguides are set to 2 mm, which accounts for a significant portion of the overall structure. This choice was made deliberately to enable manual scribing of the sample prior to transmission measurements, thereby reducing the risk of accidentally scribing across the taper section or grating, which would severely damage the device.

The next step is to create a section where the wide input waveguide transitions into the smaller waveguides that constitute the actual LPG coupler. Adiabatic tapers where the obtained transmsission increases with the taper length are used for this exact purpose [53]. The tapers used in the single and double LPG coupler designs were set to be 600 µm and sketched in Figure 5.1 and Figure5.2.

Path Bends and Grating Sections

To prevent unwanted light coupling between the input sections of the two waveguides in double LPG couplers, it is necessary to ensure an adequate distance between them. The separation is then closed before the coupling section by an 60 µm radius waveguide bend at 45°.

Finally, the LPG coupler section is positioned in the middle of the structure as shown in the schematics previously referred to. The goal of the final device is to investigate how well the simulations have predicted the LPG coupler transmission characteristics, i.e. determining the correct grating periods where coupling is achieved for wavelengths at 1.55 µm. To incorporate the irregularities that follows physical fabrication, waveguides of the same basic structure (double, single, asymmetric or symmetric) are fabricated in sets where each set contains couplers with slightly different grating periods close to the obtained value from the simulations. In addition, coupling lengths in the form of number of periods, is also investigated to some extent. When different parameters are adjusted within design sets, the resulting waveguides get varying lengths, which introduces complexity to the cleaving process and makes comparisons more challenging. To address this issue, a consistent coupler area of fixed length is assigned to all waveguides. Within this designated coupler section, the grating occupies a specific portion of the length, determined by the chosen period (Λ) and the number of periods (N) comprising the grating structure.

All section lengths are summarized in table 5.1.

Section	Length
Input	2 mm
Tapers	0.6 mm
LPG coupler	0.65-2.4 mm
Output	2 mm
Total structure length	$\sim$ 10 mm

Table 5.1: Generic section lengths for the device design.

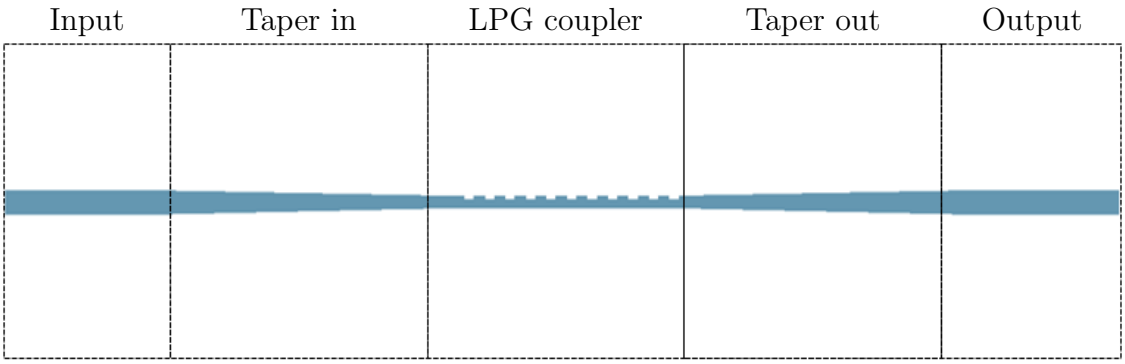

Figure 5.1: Generic schematic of the single LPG coupler design that is being patterned onto the SOI-chips. The input and output sections enable accurate cleaving and adequate light coupling, while the tapers transition the coupled light to the LPG coupler section.

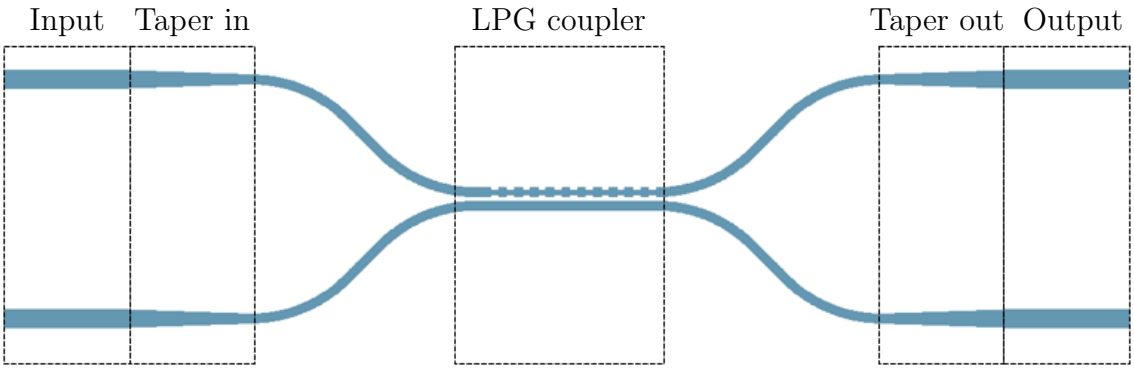

Figure 5.2: Generic schematic of the double LPG coupler design. Each section serves the same purpose as for the single LPG coupler shown in Figure 5.1.

5.2 Optimal Exposure Dose for Accurate pattern transfer

Exposure dose and development time are two key parameters related to electron beam lithography. Getting the combination of these two correct is paramount to ensure that the desired pattern is accurately transferred from the e-beam mask to the sample. It should be emphasized that it is indeed the combination of the two that accounts for a good result. For instance, a longer or more agitated development might counteract small underexposure.

The procedure for identifying proper exposure dose is executed by inspecting an array of patterns, similar to the LPG structures, of different exposure doses, all conveniently created in a single exposure process on the 100 kV Elionix ELS-100 EBL system. On the contrary, determining the correct development time requires the cleaving of each individual pattern. Subsequently, each pattern has to be immersed in the developer for different durations. As the latter procedure is both time consuming and impractical, the development procedure was fixed, while the exposure time was varied.

The chosen dose depend on the e-beam resist, thickness of the resist and the critical dimension of the pattern to be exposed. The critical dimension of the LPG couplers considered in this project is the grating depth which varies between 50 nm and 100 nm, which is why a resolution below 10 nm is required. Thus, a writing field of 500 µm divided into 1 000 000 dots is chosen with a resolution of 9, so that every 9th dot is exposed. That yields a pitch size of 4.5 nm. The beam current is set to 2 nA which yields a minimum beam diameter of 3 nm according to the manual of the EBL system that is used. However, it is important to note that the spatial extent of the exposed dot will exceed the beam diameter depending on the dose time as a consequence of the proximity effects discussed in section 3.2.1. Furthermore, subsequent processing steps such as etching will also depend heavily on the dose that is used during exposure. A test of different doses is therefore performed and the result is inspected to determine what is optimal.

The test uses simple silicon wafers, but are otherwise subject to the same lithography steps in terms of preparation and development as the α-Si chips referred to in section 5.4. Nine LPG coupler patterns were exposed onto the chip with nine different doses raging from 70 to 150 µmC/cm^2. The results are presented in section 5.2 and subsequent patterning scheme is based on the following dose test results.

Dose Test Results

Figure 1 shows optical micrographs of the grating section of three different waveguides that where exposed to an EBL dose of 80 µmC/cm^2, 120 µmC/cm^2 and 150 µmC/cm^2, respectively. As all were patterned on the same chip, they received identical development and etching treatment.

The pattern that received the largest exposure dose, depicted in Figure 5.3a, shows that the grating has been partly erased in subsequent processing steps, indicating overexposure. Overexposure contribute to increased proximity effects and leads to the exposure of a larger area than what was intended. Consequently, Small and intricate parts of the pattern becomes especially vulnerable.

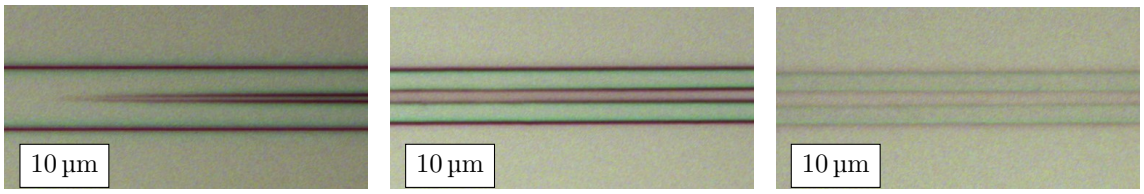

(a) 150 µmC/cm^2 (b) 120 µmC/cm^2 (c) 80 µmC/cm^2

Figure 5.3: Images from optical microscope depicting three identical waveguides that have received three different exposure doses. (a) and (c) are over and underexposed, respectively, while (b) is properly dosed.

Figure 5.3c shows a pattern characterized by slight underexposure. The diminished contrast and overall faint appearance is a clear indication that the resist was not exposed enough to withstand subsequent etching step and ensure a well-defined final pattern.

Finally, 5.3b shows a pattern that has appears to have received an adequate amount of exposure dosage during the lithography process. Edges are clearly defined and the grating is not partly erased. It is desirable to use an exposure dosage that is as high as possible without introducing excessive proximity effects. A high exposure dose ensures smooth edges and removal of all resist residues. Thus, an exposure dose of 120 µmC/cm^2 was selected as the optimal dosage for the fabrication of LPG couplers. Optical inspection performed prior to etching supports this conclusion as well[1]

5.3 Thin Film Deposition

The deposition process of SiO_2 and α-Si thin films was performed by research associates from NTNU NanoLab using a plasma-enhanced chemical vapor deposition (PECVD) system provided by Oxford Instruments [54]. The deposited oxide layer had a thickness of 1 µm, while the α-Si film had a thickness of 0.22 µm. Since the samples were obtained externally, the specific recipe and workflow used for deposition will not be discussed further.

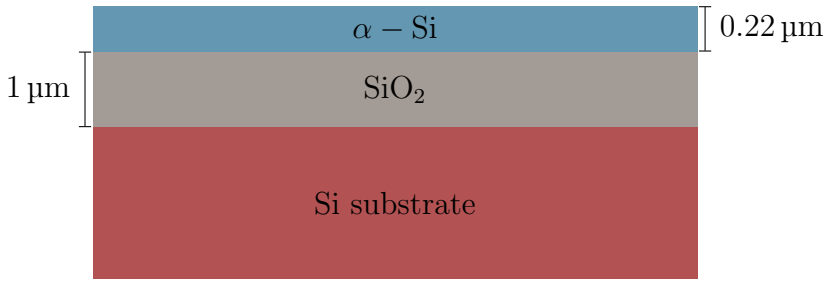

Figure 5.4: Schematic of the cross-sectional composition of the sample after thin film deposition.

[1]Material supporting this claim is found in appendix A.

5.4 Sample Coating, Exposure and Development

The patterning procedure used in this project is based on the standards used at NTNU NanoLab. The Elionix ELS-G100 100kV EBL system installed at NTNU NanoLab is utilized with optimal parameters found from the dose test presented in 5.2. An Si wafer is scribed into multiple 20x25 mm chips that are subject to the lithography procedure outlined below. Optical inspection is recommended between steps to ensure satisfactory results.

Sample preparation To clean the sample, it is submerged in an ultrasonic bath of acetone for 5 minutes with full effect. The acetone is subsequently rinsed off using isopropanol and dried thoroughly with an N_2 gun. Additional residuals are evaporated by a 1 minute dehydration bake at 150 °C.

Spin coating The sample is spin coated with a 2:1 solution of CSAR 62 (positive electron beam resist [55]) at 1000 RPM for 7 seconds and 4000 RPM for another 60 seconds to obtain a film thickness of $\sim 250\,\text{nm}$. Acceleration is set to 500 RPM/s. After the spin coating process has terminated, the film thickness is measured using a reflectometer.

Soft bake The sample is placed on a 150°C hotplate for 1 minute to reduce the residual solvent concentration in the resist layer.

Exposure The same exposure parameters that were discussed in section 5.2 are set with an area dose of $120\,\mu\text{C/cm}^2$, which yields a dose time of $0.012\,\mu\text{s}$. All important parameters are listed in table 5.2. The device pattern are subsequently exposed onto the sample.

Development The exposed sample is submerged in AR 600-459 developer for 1 minute in an ultrasonic bath at low power before being rinsed in a beaker of isopropanol.

Inspection The quality of the lithography steps above is assessed using optical microscopy with magnification levels ranging from 5x to 100x. Inadequate results leads to resist removal and process repetition.

5.5 Etching

Plasmalab System 100 ICP-RIE 180 from Oxford Instruments is utilized to etch the a-Si layer. The recipe is created by Jens Høvik at NanoLab.

Sample preparation The sample is subject to a physical cleaning process through ion bombardment, and a chemical cleaning process through the use of ionized oxygen gas in a femto plasma cleaner by Diener Electronics for 1 minute . The generator frequency and flow rate are set to 20 kH and 100 sccm, respectively. This process effectively removes any excess resist and other unwanted residues from the sample.

Parameter	Value	Unit
Acceleration Voltage	100	kV Beam current
2	nA	
Area dose	120	µC/cm^3
Field size	500	µm
Field dot number	10^6	unitless
Effective field size	500	µm
Pitch size	9 (4.5)	res (nm)
Dose time	0.025	µs/det

Table 5.2: EBL parameters used for exposure.

Function	Chemical
Electron beam resist	AR-P 6200
Developer	AR 600-549
Development stopper	Isopropanol (C_3H_8O)
Resist remover	AR 600-71

Table 5.3: List of chemicals used in the lithography process

Chamber preconditioning To eliminate any undesired chemicals from previous users, the chamber is preconditioned by executing the full recipe on a dummy wafer.

Etching The sample is placed on a Si carrier wafer and etched for a target etching depth of 220 nm. Etching parameters of the recipe are listed in table 5.4.

5.6 Scribing, Breaking and Resist Removal

In order to perform measurements, the sample must first undergo a scribing process that allows for laser and measurement equipment to access the input and output waveguides which enables light coupling. The sample therefore has to be scribed across said inputs and outputs. This can be achieved accurately in a combined scriber and breaker instrument such as the Dynatex DX-III with a diamond tip scriber and an impulse bar breaker. Due to dust and sample residuals following the scribing process, it is advisable to perform this prior to the resist removal so that all dust is cleaned off together with the resist.

The resist removal is performed in two steps. First, most of the electron beam resist is removed by immersing the sample in a beaker of AR 600-71 that is slightly agitated by sonication for 2 minutes and 40 seconds. The sample is rinsed for resist remover in two separate beakers filled with isopropanol afterwards.

Optical inspection following the aforementioned step is likely to reveal insufficient resist removal. Remaining electron beam resist is therefore eliminated using a femto

Parameter	Value
SF_6 flowrate	7.5 sccm
CHF_3 flowrate	50 sccm
Chamber pressure	15 mTorr
RF generator power	40 W
ICP generator power	600 W
Temperature	293 K
Etch time	42 s

Table 5.4: ICP-RIE parameters used for etching

plasma cleaner by Diener Electronics for 10 minutes with a generator power of 40 kHz and 200 sccm flow rate of oxygen gas.

5.7 Characterization

In between processing steps, an optical microscope is utilized to examine the sample and verify that high-quality lithography work has been achieved. Subsequently, after all fabrication and measurements are completed, the SEM Apreo, produced by FEI, is used to obtain an even better view of the fabricated devices. This is performed after all measurements because the electron beam emitted by the instrument can potentially cause degradation or significant alteration to the devices being fabricated. The damage can be seen as surface cracks, which arise due to the interaction between the electron beam and sample valence electrons. The beam might eject electrons that create an observable crack if the resulting vacancy is not filled quickly enough [56].

Chapter 6

Light Coupling and Measurement Procedure

As soon as the waveguide constructions are fabricated, they have to be subject to transmission testing. This is done in a designated laser lab with the setup schematically shown in Figure 6.2. Coupling to the individual waveguides present on a chip is obtained by utilizing a tapered lensed single-mode fiber that is placed in immediate vicinity to the waveguide input as pictured in Figure 6.1a. At the output port of the waveguide, shown in Figure 6.1b, a cleaved single-mode fiber is placed similarly to lead the transmitted light through a Thorlabs biased detector (DET10C) and photodiode amplifier (PDA200C), before the signal is processed on a computer. The light source is a Thorlabs TLK-1550M external cavity laser that is fed through a TE-polarizer.

Accurate alignment is a prerequisite for adequate measurements. Therefore each fiber end, input and output, are mounted on an Elliot precision XYZ-stage that is placed under an Olympus BXFM optical microscope. The microscope is also equipped with a Hamamatsu C14041-10U near-infrared capable camera to enable images of non-visible light coupling.

Transmission measurements was performed by having the laser sweeping through wavelengths from 1.46 to 1.64 µm and reading off the measured transmission from the computer. Savitsky-Golay filtering was used to de-noise the signal [57].

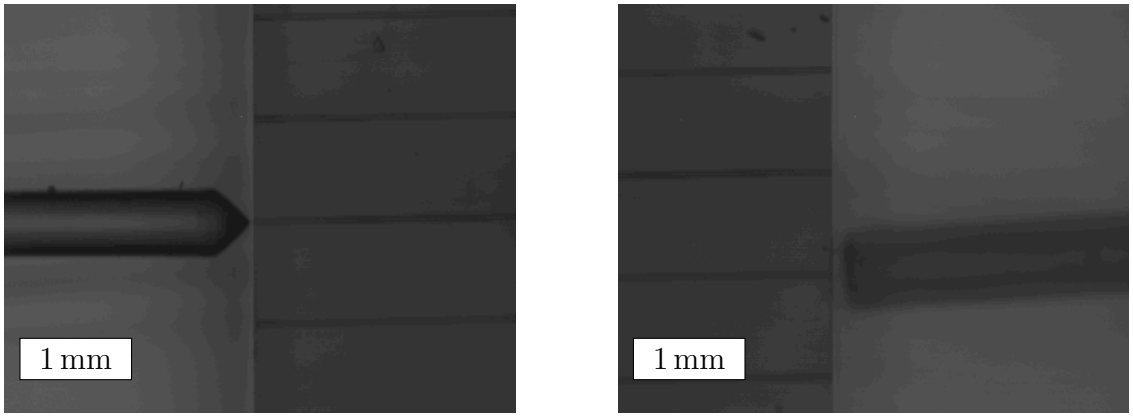

(a) Input (b) Output

Figure 6.1: Image generated by infrared radiation showing the input (a) and output (b) light coupling setup. The dark horizontal lines are the individual waveguides that needs to be aligned with the optical fibers during measurements. The input fiber has a tapered lensed end that focuses the light to minimize coupling loss. The output fiber end is cleaved to maximize light capture. Note that the (a) and (b) is not aligned in this figure, while in reality the light is obviously coupled to the same waveguide that is being measured.

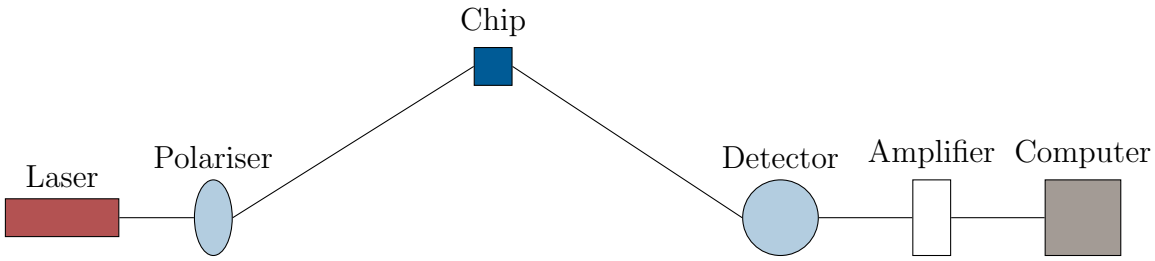

Figure 6.2: Experimental set-up for transmission measurements. A laser is TE polarized, led through an optical fiber and coupled to the waveguide of choice present on the LPG chip through a lensed fiber end. On the output, the laser is coupled from the waveguide and into a cleaved fiber. This fiber is connected to a photodiode that detects the light intensity and feeds the information into an amplifier before all measurements are shown on the computer.

Chapter 7

Results and Discussion for Single LPG Coupler

7.1 MPB Simulation Results

MPB simulations of a $0.5 \times 0.22\,\mu m^2$ LPG coupler was conducted in the unpublished preliminary work. The result are briefly summarized in 7.1 for later referance. Λ refers to the required grating period for coupling while $S_{\pm}$ and $S_{1.55}$ are the sensitivities calculated for wavelengths $\pm 0.1\,\mu m$ away from the PMTP and at operation wavelength, respectively. This section is included for completeness and will not be subject to further elaboration.

Design	PMTP [µm]	Λ [µm]	S_- [µm/RIU]	S_+ [µm/RIU]	$S_{1.55}$ [µm/RIU]
Single	1.36	1.48	0.103	0.18	0.15

Table 7.1: Summarized results from the double LPG structures, design A and B. The phase matching turning point, required grating period for coupling and sensitivities are included. Important findings of the single LPG coupler that was analyized in the specialization project are also included for comparison purposes.

7.2 Lumerical Simulation Results

Lumerical MODE eigenmode expansion analysis was performed to investigate the transmission properties of a $0.5 \times 0.22\,\mu m^2$ single LPG coupler with respect to the grating period. The number of periods and grating depth was set to 100 and 0.1 µm, respectively. As the group span was defined as the grating period, the simulation software can compute the transmission for a large set of grating periods by sweeping through a range of group spans at operation wavelength 1.55 µm. The solver then calculates the scattering parameters that relate the transmission and reflection coefficients for each port at a given mode. The port configuration is shown in Figure 7.1 where the source is indicated with an arrow. The absolute value of the scattering parameter squared $|S_{21}|^2$ describes the transmission through port 2 from port 1, i.e. the transmission of the device.

Figure 7.1: Single LPG coupler port configuration during Lumerical simulations. The source port is indicated by the arrow.

Transmission Analysis of Varying Grating Periods

First, the transmission was calculated for grating periods ranging from 1 to 15 µm in order to investigate the resonance behavior of the LPG coupler for multiple orders. The result is plotted in Figure 7.2. Previous simulation work with this single LPG coupler design in MPB predicted the required grating period for coupling to be a multiple of 1.48 µm (Table 7.1) , which is why the grating periods corresponding to the first five even orders[1] are indicated by the dotted lines.

The Lumerical simulations seems to agree well with the MPB simulations, especially for the lower order grating periods. The first resonance drop occurs at $\Lambda = 2.73\,\mu\text{m}$ while the grating period corresponding to the second order diffraction mode was found to be $2 \times 1.48\,\mu\text{m} = 2.96\,\mu\text{m}$ in MPB. The significantly larger discrepancies observed for the higher orders gratings is a consequence of how this deviation grows for each resonance.

Based on the MPB simulations, resonances were expected to occur for grating periods $\Lambda_m = \Lambda_1 \times m$ for $m = 1, 2, 3, 4....$ However, in the Lumerical simulations, only even-order resonances were observed. This discrepancy can be attributed to the differences between the two simulation methods. In the MPB simulation, the grating specifics were not taken into account. The fundamental and second modes were calculated independently, and the grating period was determined by assuming that periodic variations in the refractive index would generate quasi-Bloch modes, which would couple the propagating mode to the cladding mode. On the other hand, the transmission simulations performed in Lumerical considered the actual shape of the grating during calculations. Since the grating was asymmetrically designed, it is likely that only grating periods corresponding to even diffraction orders could generate sufficient coupling to the second mode.

Minor Transmission Drops and Resonance Variability

In addition to the strong resonances observed in the plot, several minor transmission drops are also evident. These drops may arise from the coupling between modes other than the first and second modes. Alternatively, they could be attributed to Fabry-Perot resonances caused by the reflection of light due to variations in the refractive index [58]. It is important to note that such noise is an inherent characteristic of grating devices and is heavily reliant on achieving perfect periodicity to be observable. However, perfect periodicity is not practically achievable in experimental settings, and therefore, these minor drops will not be further considered.

It is also noted that the transmission for each resonance varies considerable throughout the plot. Almost none of the signal is transmitted for $\Lambda = 8.2\,\mu\text{m}$ while half of the signal is transmitted at $\Lambda = 13.9\,\mu\text{m}$. The grating period required for perfect coupling is in many ways a theoretical value that is not possible to

[1] $\Lambda_m = \Lambda_1 \times m, \quad m = 2, 4, 6, 8, 10$ where $\Lambda_1 = 1.48\,\mu\text{m}$

obtain exactly. The interpolation between data points could potentially hide some information meaning that resonances with a deeper dip are located closer to a specific data point. This hypothesis was investigated by conducting additional simulations with more data points around a specific resonance, but did not yield less transmission than previously calculated. Another explanation is that this is a consequence of the coupling length, i.e. the number of periods. Additional simulations, found in appendix B, revealed that this was indeed the case.

More simulations were conducted around the third resonance that showed the strongest coupling. Figure 7.3 shows the resulting transmission plot and side lobes that typically occur in the proximity of resonances.

To summarize, the single LPG structure showed promising transmission characteristics that is in good agreement with theory and previous results. The discrapency can be explained by the grating design that was not specified in the MPB simulations.

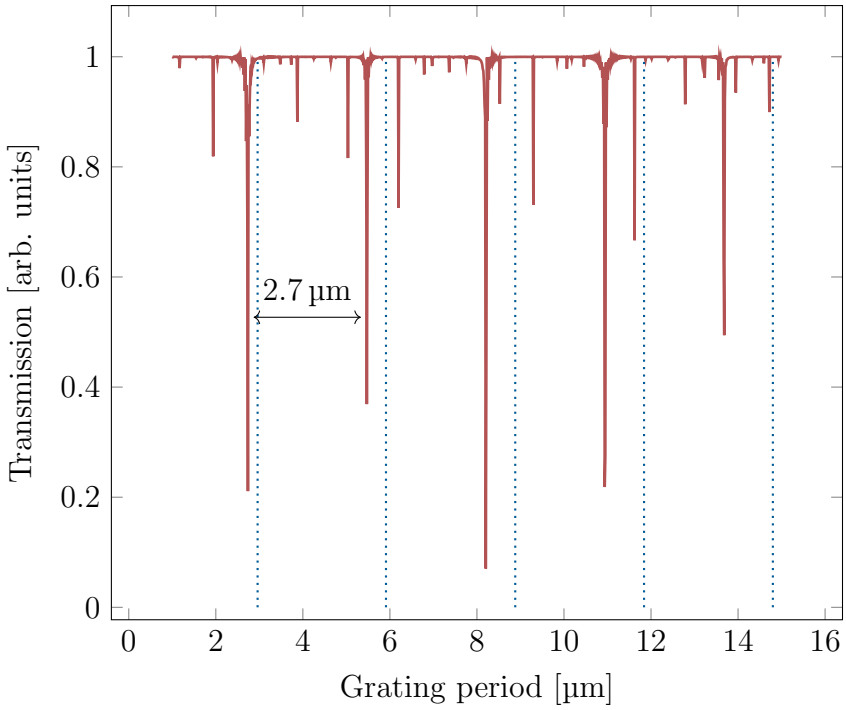

Figure 7.2: Transmission simulations for $0.5 \times 0.22\,\mu m^2$ single LPG couplers of width grating period varying from 1 to 15 µm at $\lambda = 1.55\,\mu m$. Grating depth and number of periods were held constant at 0.1 µm and 100, respectively. The dotted lines indicate even order resonance grating periods that were calculated in MPB.

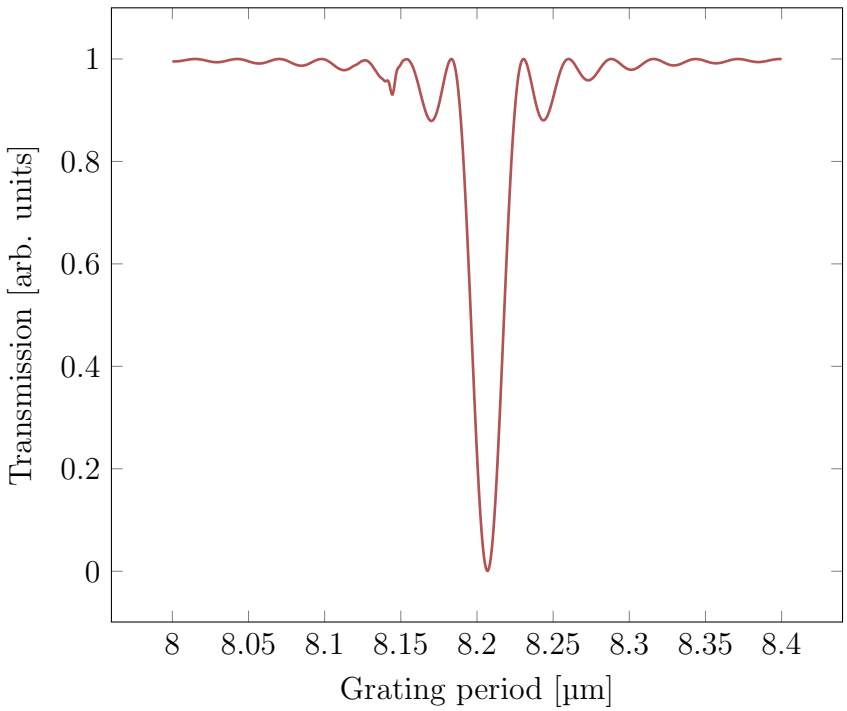

Figure 7.3: Transmission simulations for $0.5 \times 0.22\,\mu m^2$ single LPG couplers of grating period around 8.2 µm at $\lambda = 1.55\,\mu m$. Grating depth and number of periods were held constant at 0.1 µm and 100, respectively.

7.3 Fabrication Results and Characterization of Single LPG Couplers

Overview and Parameter Choice

To investigate the validity of the simulations, a chip containing five single LPG couplers was fabricated with five different grating periods close to the target grating period corresponding to $\Lambda_5 = 5 \times 1.47\,\mu m = 7.35\,\mu m$ from the MPB simulations[2].

For each grating period, five coupling lengths, or equivalently five number of periods N was fabricated resulting in a total of 25 single LPG couplers. The grating depth was set to $0.05\,\mu m$.

7.3.1 Characterization

Patterning and Grating Results

Figure 7.4 depicts five of the LPG waveguides after all processing steps were extecuted. All residual electron beam resist has been eradicated and the waveguides structures appear to be well-defined. The subfigure in the top corner shows that the small features of the text boxes has been patterned successfully as well. A text box including important parameter values was assigned to each waveguide and patterned in close proximity to the relevant structure to distinguish individual waveguides.

Figure 7.5 depicts the grating structure imaged in more detail through a SEM. The grating is indeed well defined and the width was measured to be $0.5\,\mu m$. However, the grating appears to have obtained a small deviation from the optimal 90° angle. SEM imaging was not performed in-between development and etching, which means it is difficult to say witch step was the cause. However, the deviation is very small and will likely not have any significant effect on the performance of the device.

Etch Profile

To assess the quality of the sample further, secondary electron SEM imaging was conducted for the cross section of the device. Figure 7.6 displays the cross-sectional view of the input waveguide and with etch trenches on each side. The silicon substrate is clearly distinguishable from the oxide layer, as indicated by the distinct contrast in grey color. Although difficult to see, a slight contrast can also be observed between the oxide layer and the deposited $\alpha - \mathrm{Si}$ material, which aligns well with the etch depth.

A more detailed image of the etch trench is depicted in Figure 7.7. The etch profile demonstrates a high degree of anisotropy, with minimal deviation from a vertical sidewall angle. Moreover, the sidewall roughness appears reasonably smooth, although further magnification is required to make more definitive observations

The layer of SiO_2 and α-Si was measured to be 980 nm and 220 nm, respectively.

[2]This deviates from the value listed in table 7.1 because subsequent measurements will be carried out in an air environment rather than water. To account for this adjustment, the simulations were rerun with the only modification being the refractive index of the surrounding medium, which was changed from 1.31 to 1.

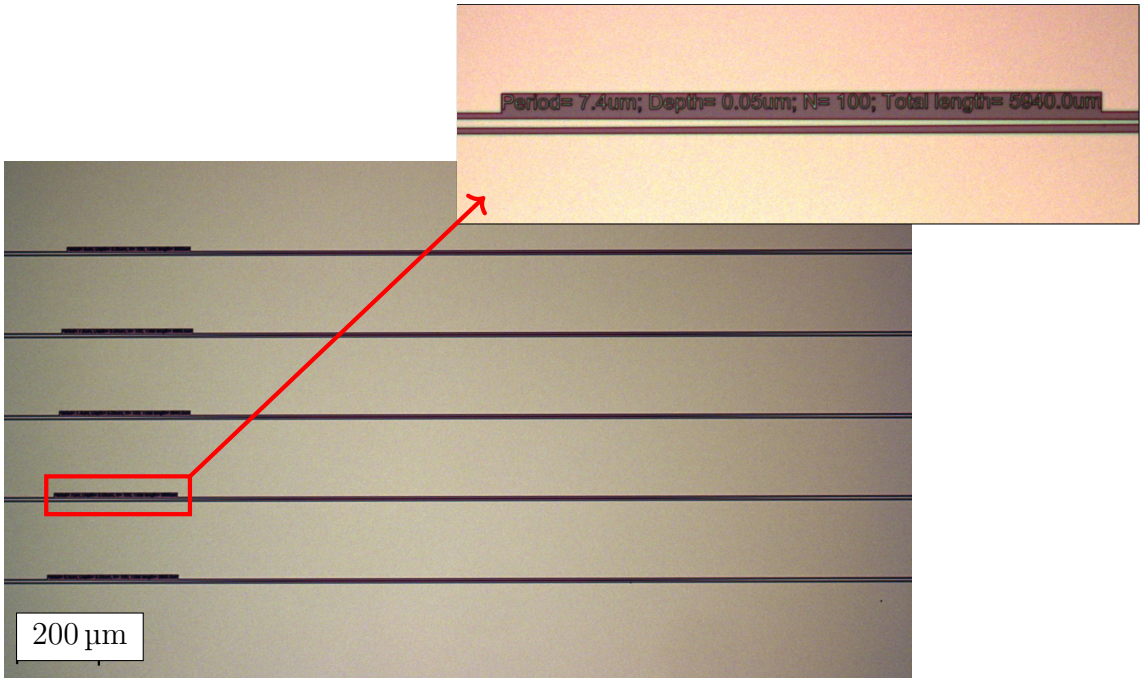

Figure 7.4: Optical micrograph of 5x magnification showing a set of single LPG with grating period $\Lambda = 7.4\,\mu m$. A summery of important parameters related to each individual waveguide was also patterned as shown by the red arrow.

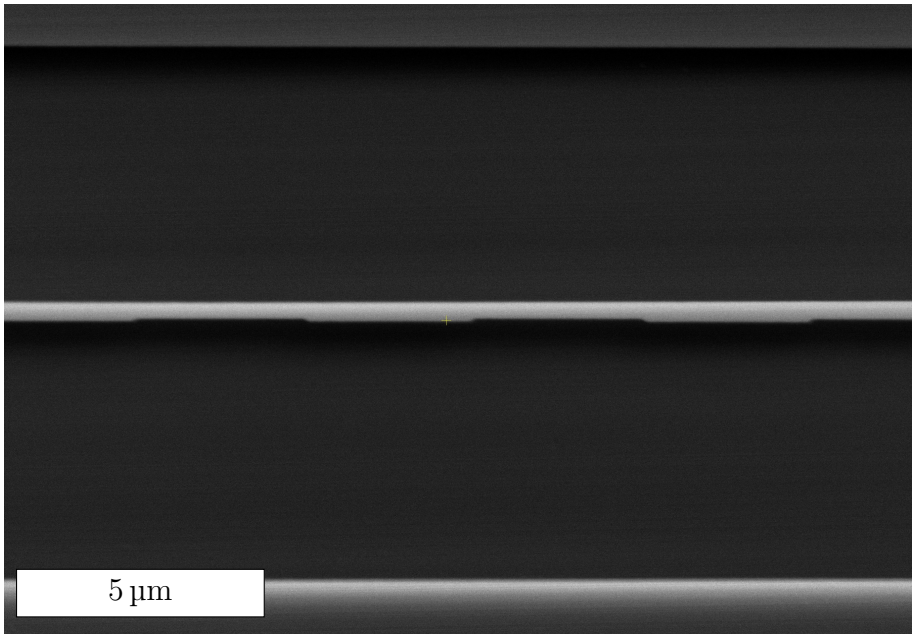

Figure 7.5: SEM image showing top view of the grating in the fabricated single LPG coupler.

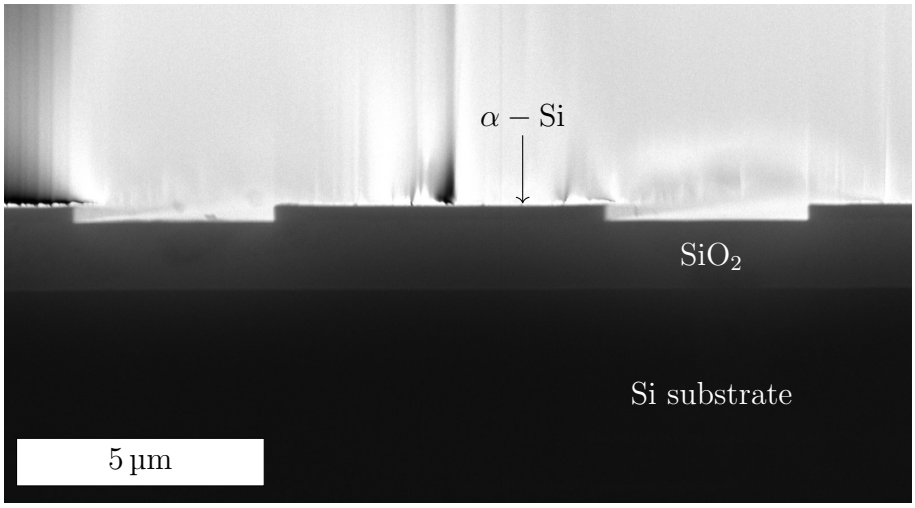

Figure 7.6: Cross sectional view of the layers of Si, SiO_2 and $\alpha - Si$ that constitute the sample captured with SEM.

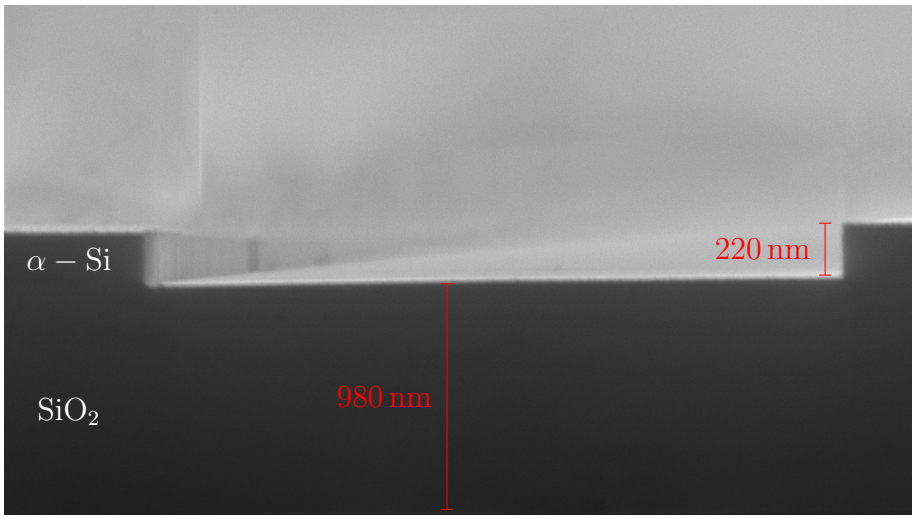

Figure 7.7: SEM image showing the cross section of the input waveguides and underlying oxide layer. The etch depth and oxide layer was measured to be 220 nm and 980 nm, respectively.

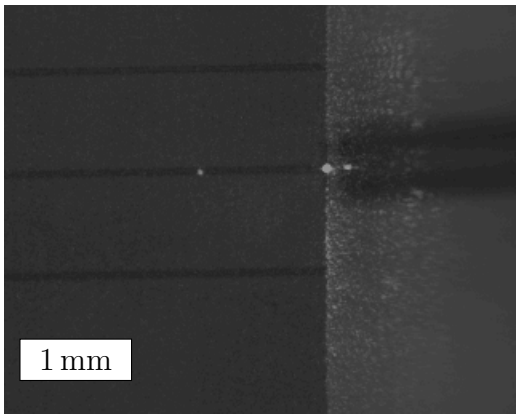

(a) Successful light coupling

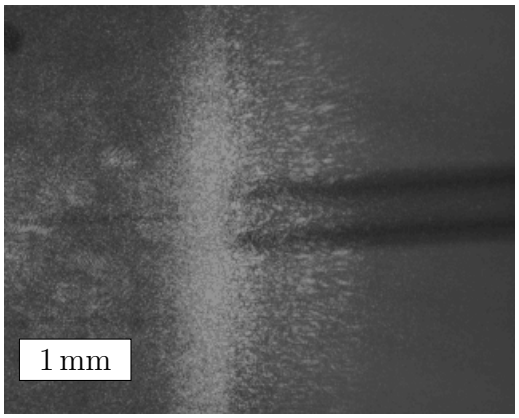

(b) Unsuccessful light coupling

Figure 7.8: Images generated by infrared radiation showing (a) successful and (b) unsucessful light coupling at the output of two LPG couplers. Adequate light coupling was not possible to obtain for some of the structures.

7.4 Measurements Result

Light Coupling

Figure 7.8a and 7.8b show the output of waveguide structures that achieved successful and unsuccessful light coupling followed by sufficient guiding, respectively. Successful light coupling is characterized by the light being focused and accumulated at the output port, while a considerable light distribution indicates unsuccessful coupling.

Most waveguides were adequately coupled to the light source and exhibited acceptable guiding properties, but five individual structures were unable to couple and properly guide the incoming light. This could be a consequence of poor alignment, or damages and irregularities on the structures that leads to power leakage into the cladding.

Results from Transmission Measurements

All waveguides that were able to couple the incoming light showed adequate transmission characteristics. There was, however, significant levels of noise introduced to the signal. Furthermore, no resonances manifested as a transmission drop were observed. The only measurements that indicated some sort of resonance are plotted in Figure 7.9. It shows the results of the transmission measurements for the five waveguides with a grating period of 7.4 µm[3].

No strong coupling effect was observed, but a slightly distinctive drop between wavelengths of 1.55 and 1.58 µm appeared on all structures. The drop was largest for the $N = 180$ LPG coupler as indicated by the red ring in Figure **??**. This observation is particularly promising as the grating period in question is very close to that which was calculated by MPB to achieve resonance at 1.55 µm wavelengths. The measurements does however present significant inconsistencies with theory.

[3]The shape of the measurements is consequence of the $\lambda = 1.55$ µm centered gain chip used by the laser [59]. Normalization of the lasing curve was deemed redundant as only resonance phenomena are considered.

If there was indeed a coupling effect happening between wavelengths of 1.55 and 1.58 µm, the effect should have been stronger for longer grating lengths, i.e. measurements of structures with $N = 220$ and $N = 260$ should have produced a more distinct drop than that of $N = 180$. However, the latter shows the deepest transmission drop. Thus, it might be detection noise rather than an resonance coupling.

To investigate the possible resonance further, the same structures were measured once more with a narrower spectral range. The results can be found in appendix C and showed no significant transmission drop for any wavelengths. This supports the suggestion that the observed "dip" is actually just detection noise.

7.5 Possible Design Flaws in the LPG Coupler Performance

There could be a number of reasons why the LPG coupler design did not work as intended and why no resonance with associated transmission drop was observed . It could be due to inaccurate fabrication steps and poor experimental execution, design flaws or a combination of these.

It is most likely not due to inaccurate fabrication steps. Almost all lithography steps and experimental recipes are standard for SOI fabrication, and resulting structures were inspected in-between steps. Additionally, light coupling from optical fiber was achieved, which proves that the structures works well as effective waveguides.

That leaves design flaws as a possible explanation of the poor coupling characteristics. Firstly, all gratings had the same grating depth of 0.05 µm, which could be too small. Especially in the case for real-life fabrication. In Figure 7.5, the corrugation is not as distinct as the simulated device leaving a trapezoid-shaped grating. This shape makes for a smoother transition between thick and thin sections that might impair the coupling effect. In other words, even though this grating depth was sufficient during simulations, it might result in a coupling effect too weak to observe in a real-life device.

Furthermore, the grating length might also be the cause for the absence of observed coupling. If the grating length is considerably shorter than the coupling length, it will be difficult to observe any resonance in transmission measurements. Grating lengths on this chip varied from 0.65 mm to 2 mm. As this is a single waveguide structure, there is no chance for the light that is coupled out of the propagating mode to de-couple back into it. Thus, it is advantageous to make the grating as long as possible to ensure that the coupling length sufficiently long.

Another possible design flaw is the length of the structures. For this chip, the total length of the waveguides varied from 5.8 mm to 7.3 mm. After scribing input and output sections, these become significantly shorter which becomes a problem during transmission measurements. Short structures means that the distance between the input and output ports become small, which leads to increased noise. Some of the laser power will not be coupled into the waveguide, but scatter around the input port. Some of this scattering will be measured by the detector and lead to higher levels of noise. A portion of this noise can be filtered out during signal processing, but excessive filtering might also filter out important findings. It is therefore desirable to reduce the amount of noise as much as possible prior to signal

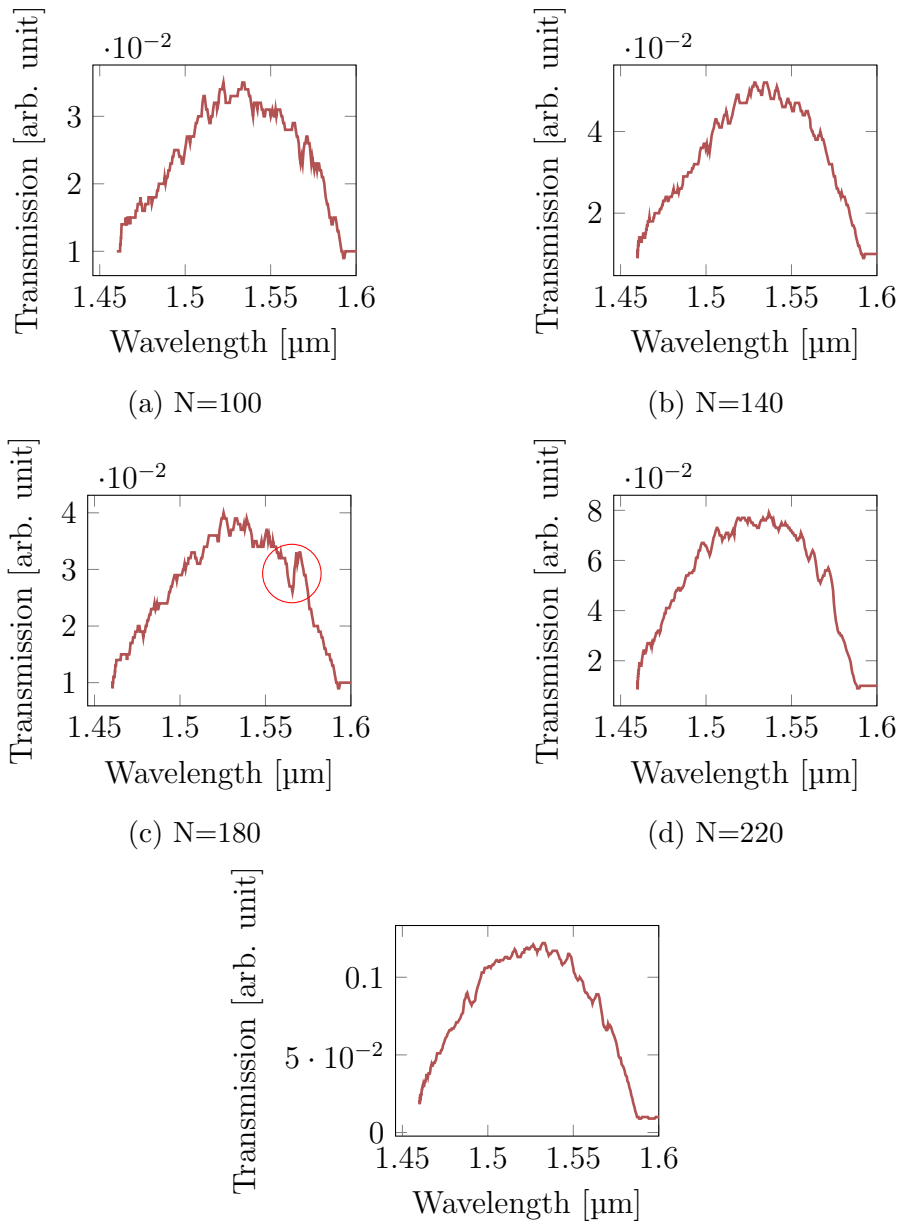

(a) N=100

(b) N=140

(c) N=180

(d) N=220

(e) N=260

Figure 7.9: Transmission measurements performed on single LPG couplers with grating depth and period of 0.05 nm and 7.4 µm, respectively, with five different coupling lengths represented by the number of periods N. The red circle in (c) indicates a possible transmission drop.

processing.

Another explanation is that the coupling strength around this grating period is simply not strong enough because the target grating period $\Lambda = 7.35\,\mu m$ corresponds to an odd order diffraction mode. No resonance was obtained around this grating period in the Lumerical simulations, which appears to be the case for the physical device as well.

In conclusion, the grating period has to be adjusted according to Lumerical predictions, while the grating depth, grating length and total structure length has to be increased to strengthen the coupling effect sufficiently to overpower the noise introduced during measurements.

Chapter 8

Results and Discussion for Double LPG Coupler

8.1 MPB Simulation Results

During the specialization project, MPB was applied thoroughly to simulate single and doublel LPG coupler designs. Several designs were found to show promising sensitivity characteristics, especially the double LPG designs. However, after additional work and analysis the designs had shortcomings. One of these shortcomings was the multimodal overlap and another was the fabrication practicalities that would follow. Both of these issues was therefore handled in this project and the result is presented here.

Section 8.1 presented two approaches employed to determine the optimal waveguide widths for achieving the desired sensitivity characteristics in the double LPG coupler design. These approaches were outlined as follows:

A The sensitivity of structures with varying widths was calculated while maintaining a constant height ($h_1 = h_2 = h = 0.22\,\mu\text{m}$).

B The sensitivity of different structures was calculated, allowing both the height and width to vary across various combinations.

Based on Approach A, design A was obtained, while design B was derived from Approach B. The relevant dimensions of these designs can be found in Table 8.1. Note that both methods yielded very similar dimensions, the only difference being the height of the waveguides.

An interesting observation is that both approaches calculated the highest sensitivities for the smallest widths in the variable range listed in Table 4.3. On the contrary, Høvik et al. observed that the sensitivity of a single LPG coupler increased for larger waveguide widths, which demonstrates differences between double and single LPG devices [7].

Dispersion Relations and Effective Refractive Index of Coupling modes

Dispersion relations for design A and B are plotted in Figure 8.1. It shows the relation between frequency and propagation constant for the fundamental (Figure 8.1a) and second order (8.1b) modes in each design. As each design consist of two

Method	$w_1 \times h_1$[µm]	$w_2 \times h_2$[µm]
A	0.433×0.220	0.400×0.220
B	0.433×0.200	0.400×0.200

Table 8.1: LPG coupler designs that yielded best sensitivity characteristics for the two methods

Mode	n_g	n_{eff}
A1	0.234	2.273
A2	0.229	2.183
B1	0.238	2.172
B2	0.234	2.085

Table 8.2: The group refractive indices n_g and effective refractive indices n_{eff} for the fundamental modes of waveguide 1 and 2 in design A and B. These are important indices that are found from the dispersion relation and characterizes modes within waveguides.

waveguides, there are a total of four modes present in each plot. The dotted lines indicates the frequency that corresponds to the operation wavelength of 1.55 µm, while the shaded areas represent all combinations of frequencies and propagation constants that are disallowed in the structure.

As shown in the plots, all fundamental modes are indeed allowed to propagate as they intersect the dotted line below the lightline. On the other hand, second order modes intersects the same line for forbidden frequencies. Thus, all waveguides in both design A and design B, are single moded.

Important findings from the dispersion relation in Figure 8.1a are listed in Table 8.2, where A1 and A2 refer to the fundamental modes of waveguide 1 and 2 in design A as schematically shown in Figure 4.2.

Required long period grating for coupling

For the two designs to achieve coupling between fundamental modes, the introduced grating needs a periodicity that satisfies equation (2.46) for wavelength λ. The grating for design A and B was found to be 17.21 µm and 17.81 µm, respectively, for $\lambda = 1.55$ µm. As the critical coupling is a periodic effect, a suitable multiple of this periodicity can be chosen for fabrication purposes.

Enhanced Sensitivities at Phase Matching Turning Points

Figure 8.2a shows how the group index difference between the fundamental modes within each design varies for wavelengths ranging from 1.2 to 2.0 µm. The phase matching turning point for device A and B was found to be at 1.74 and 1.67 µm, respectively. At these wavelengths, the two fundamental modes of each device has the same effective group index and the denominator in equation (2.47) approaches zero. The consequence of this can be seen in Figure 8.2b, where the sensitivities are plotted as functions of wavelength. Both sensitivities spike asymptotically at their

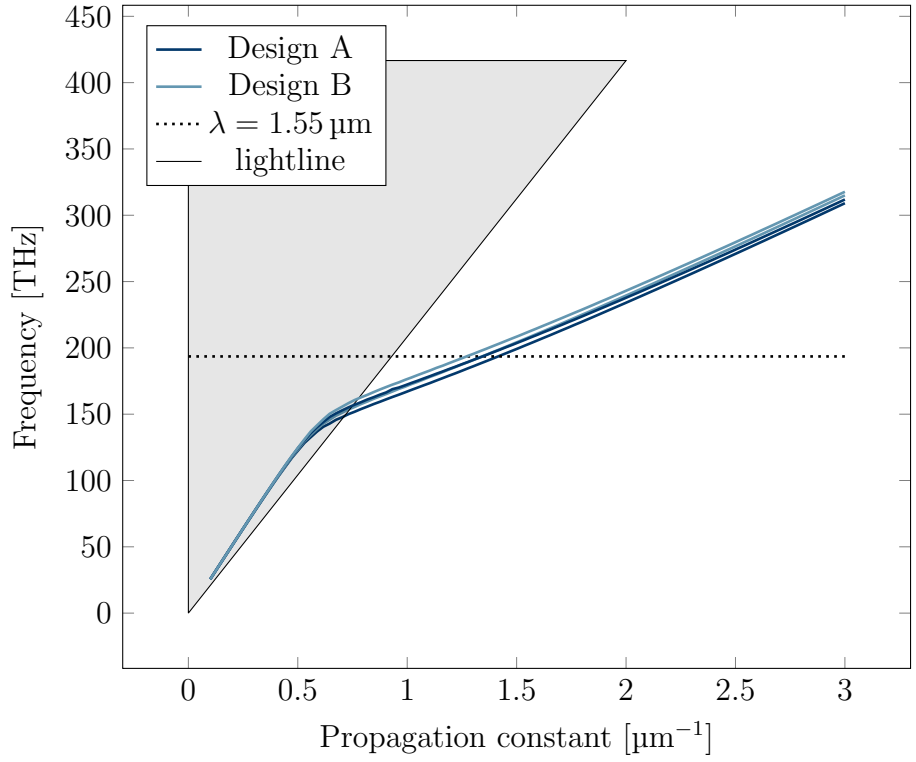

(a)

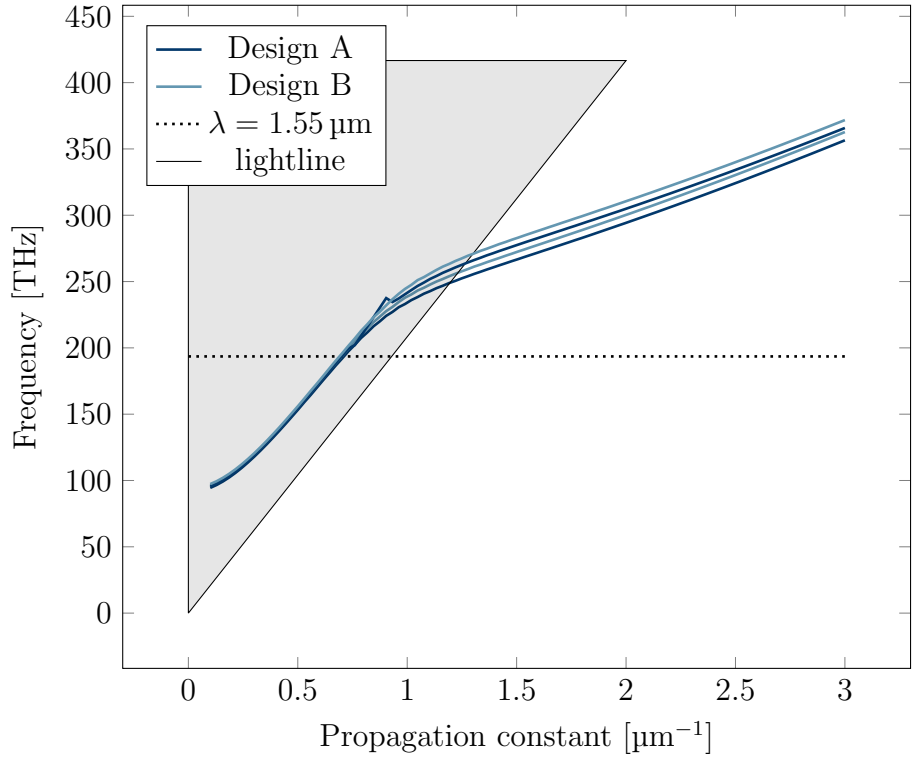

(b)

Figure 8.1: Dispersion relation of the fundamental modes (a) and second order modes (b). The dotted line marks the frequency that corresponds to the operation wavelength and the shaded area indicates the set of unbound frequencies above the lightline. No modes above this line are allowed to propagate.

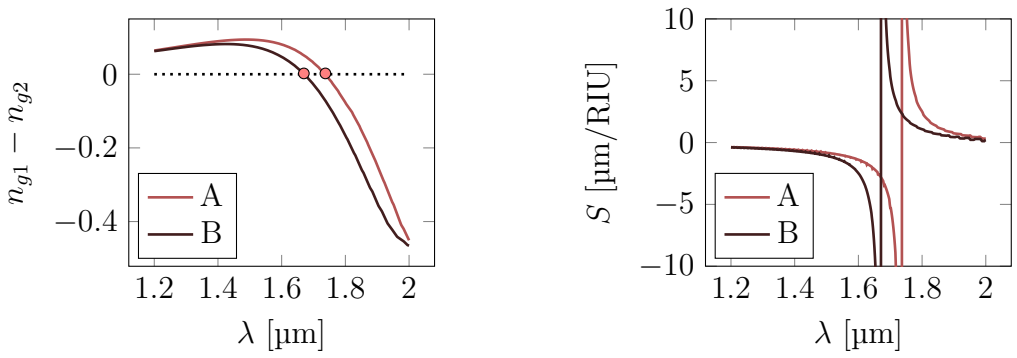

(a) (b)

Figure 8.2: a) Group refractive index difference between the fundamental modes in each device plotted as a function of wavelength. The zero of each graph, denoted by the red dots, refers to the phase match turning point of the two LPG coupler designs. b) Plotted sensitivity of design A and B. Both sensitivities increases exponentially at their respective phase match turning point.

respective PMTP.

In order to examine the sensitivity over a broader range, specific sensitivities were calculated for three wavelengths. These includes the sensitivity at operation wavelength, denoted as $|S_{1.55}|$, and at wavelengths $\pm 0.1\,\mu m$ away from the PMTP, denoted as $|S_{\pm}|$.

Comparative Analysis and Performance Evaluation

Table 8.3 lists the most important findings from the double LPG coupler designs where the calculated sensitivities are given in micrometers per refractive index unit ([µm/RIU]). Both designs exhibit considerably better sensitivities than the single LPG coupler from the preliminary work, yielding almost a ten fold increase in the case for B. The sensitivities of design A and B was found to be 1.03 and 1.48 µm/RIU, respectively, at $\lambda = 1.55\,\mu m$. For comparison, a typical racetrack ring-resonator design has a sensitivity of $\sim 0.07\,\mu m/RIU$, but can be improved to yield 0.48 µm/RIU by utlizing a sub-wavelength grating [60][61]. Furthermore, design B exhibit a sensitivity slightly higher than the refractive index sensor of Liu et al. based on coupling between a strip waveguide and a slot waveguide of 1.46 µm/RIU [28].

On the other hand, LPG couplers of significantly higher sensitivities has also been observed. Jens et. al measured sensitivities up to 5 µm/RIU at the PMTP for a single LPG coupler design [7]. It should however be noted that this was measured on a 0.58 µm wide waveguide and that the sensitivities for waveguides of widths below 0.5 µm were considerably lower, around 0.5 µm/RIU. Wider waveguides are typically multimode and suffer from higher attenuation and multimodal dispersion. The simulations of Design A and B obtained in this study, however, yielded high sensitivities for a broad operation range utilizing single mode waveguides. The sensitivities $\pm 0.1\,\mu m$ away from the PMTP, $|S_+|$ and $|S_-|$, was found to be above 1.7 and 1.4 µm/RIU.

Comparing the two designs with each other reveals slightly higher sensitivities

Design	PMTP [µm]	Λ [µm]	S_- [µm/RIU]	S_+ [µm/RIU]	$S_{1.55}$ [µm/RIU]
A	1.74	17.21	1.86	1.45	1.03
B	1.67	17.81	1.76	1.46	1.48
Single	1.36	1.48	0.103	0.18	0.15

Table 8.3: Summarized results from the double LPG structures, design A and B. The phase matching turning point, required grating period for coupling and sensitivities are included. Important findings of the single LPG coupler that was analyzed in the specialization project are also included for comparison purposes.

Figure 8.3: Double LPG coupler port configuration during Lumerical simulations. The source port is indicated by the arrow.

calculated for design B, except for $|S_-|$. Approach B had more parameters subject to variations which explains its slight superiority. As the dimensions of the two designs turned out to be very similar, this is to be expected. The deviation is, however, so small that design A is preferred for further analysis due to manufacturing concerns and compatibility with existing fabrication techniques.

8.2 Lumerical Simulation Results

As mentioned above, design A was selected to be the best option for further analysis and is therefore the only design considered in this section. Figure 8.3 shows a schematic of the design and the location of ports 1, 2, 3 and 4. Port 1 is the source port which means that all coupling is related to the transmission of power from this port through port 4.

Spacing Effects for Optimal Resonance Conditions

To find an appropriate spacing between the waveguides that constitute the device, transmission simulations were executed for a set of different spacings within the range 0.1 to 0.7 µm and a constant number of periods set to $N = 100$. Some of the results are plotted in Figure 8.5 which shows the transmission through port 2 ($|S_{21}|^2$) and 4 ($|S_{41}|^2$) for grating periods between 1 and 100 µm at $\lambda = 1.55$ µm. The periodic coupling between the two waveguides becomes sharper for the larger spacings > 0.4 µm as shown in 8.5c and 8.5d, respectively. Smaller spacings such as 0.2 and 0.4 µm shown in 8.5a and 8.5b, respectively, are affected by more fabry-perot noise and overcoupling tendencies for almost all grating periods. Such evanescent coupling occurs due to the continuous leakage of power between waveguides that are in very close proximity.

Another interesting attribute of the coupling that is particularly evident for

the two largest spacings is that the coupling strength varies for different grating periods. To understand this, it is important to note that the number of periods was held constant for all simulations, but the same is not the case regarding the coupling length. The strength of each resonance will depend heavily on the coupling length, and is expected to be periodic. This is a consequence of how the propagating power will couple back and forth throughout the coupling section if it is permitted. Larger grating periods acquire a longer coupling length which again affect the overall coupling.

The goal of this project is to fabricate a functional device, which means it is desirable to identify the sharpest resonance with the highest peak and use the combination of grating period and grating length to achieve this at operation wavelength 1.55 µm.

The structure with a spacing of 0.6 µm exerted best transmission characteristics in terms of sharp and defined resonances, but as half of the resonances vanished, it was not subject to further investigation. Instead, Figure 8.5 indicates that 0.5 µm is an appropriate spacing and the transmitted power as a function of grating periods for this spacing is therefore plotted in Figure 8.4.

Resonance Peak Analysis and Symmetry Effects

The resonance peak between 10 and 20 µm appears most suitable and is subject to further investigation. The periodicity of the resonance peaks was found to be 16.3 µm. MPB simulations yielded a required grating period $\Lambda = 17.21$ µm corresponding to the first order diffraction mode, which is in very good agreement with the results in Figure 8.4.

An interesting finding is that which relates to the gratings corresponding to even and odd diffraction modes. In Figure 8.5d, only half of the resonances remain. This is very similar to what was observed for the single LPG coupler simulations presented in the Section 7.2. It is clear from Figure 8.5a that resonances corresponding to odd orders undergo a stronger coupling than even ones. Similarly to the simulation findings for the single LPG coupler, this could be attributed to the shape of the grating. Additional simulations was thus performed for an asymmetrical waveguide with identical parameters. The results are included in Appendix D and showed no change in the transmission plot which contradicts the reasoning given earlier. An alternative explanation is that the difference in resonance strength is not due to the symmetry of the grating, but rather a result of the symmetry of the mode that is coupled. It indicates that asymmetric mode coupling (single LPG case) is stronger for gratings corresponding to even diffraction modes, while symmetric coupling favours odd ones.

Coupling Length and Associated Transmission Behavior

To find the coupling length, the maximum transmission value through port 4 $|S_{41}|^2$ within the grating period range of 14 and 18 µm was calculated for coupling lengths between $N = 25$ to $N = 175$. The result is plotted in 8.6a. As expected, the behavior is periodic, but it occurs between 1 and 0.4. The plot indicates that the coupling reaches its peak with a periodicity of $81N$, but never drops down to zero as expected for traditional couplers **??**. Further investigation revealed that the lowest

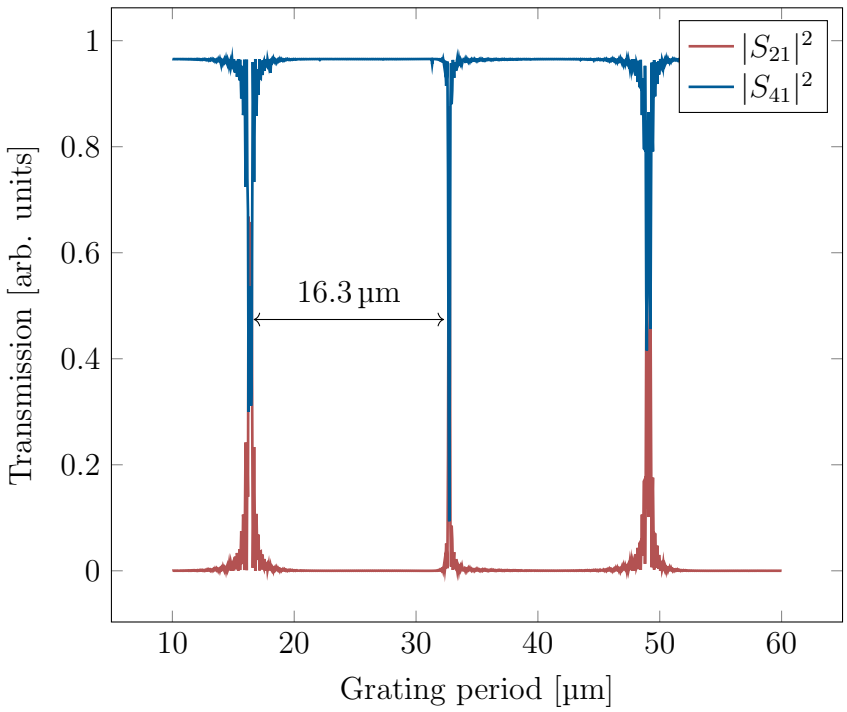

Figure 8.4: Transmission through port 2, $|S_{21}|^2$, and port 4, $|S_{41}|^2$, as a function of grating periods for design A. The simulations was done for $N = 100$ and 0.05 µm grating depth. The periodicity was found to be 16.3 µm.

transmission peak converges toward full transmission for large Ns as shown in Figure 8.6b.

A quasi-coupling length can be defined as coupling length for which the transmission has gone from minimum to maximum[1]. The distance between successive peaks in Figure 8.6a was found to be 81, which means the number of periods between maximum and minimum transmission is approximately 40. The quasi-coupling length can then be calculated as $L_c = 40 \times 16.3\,\mu\text{m} = 652\,\mu\text{m}$. .

[1]The actual coupling length is defined in section 2.4 regarding coupled mode theory.

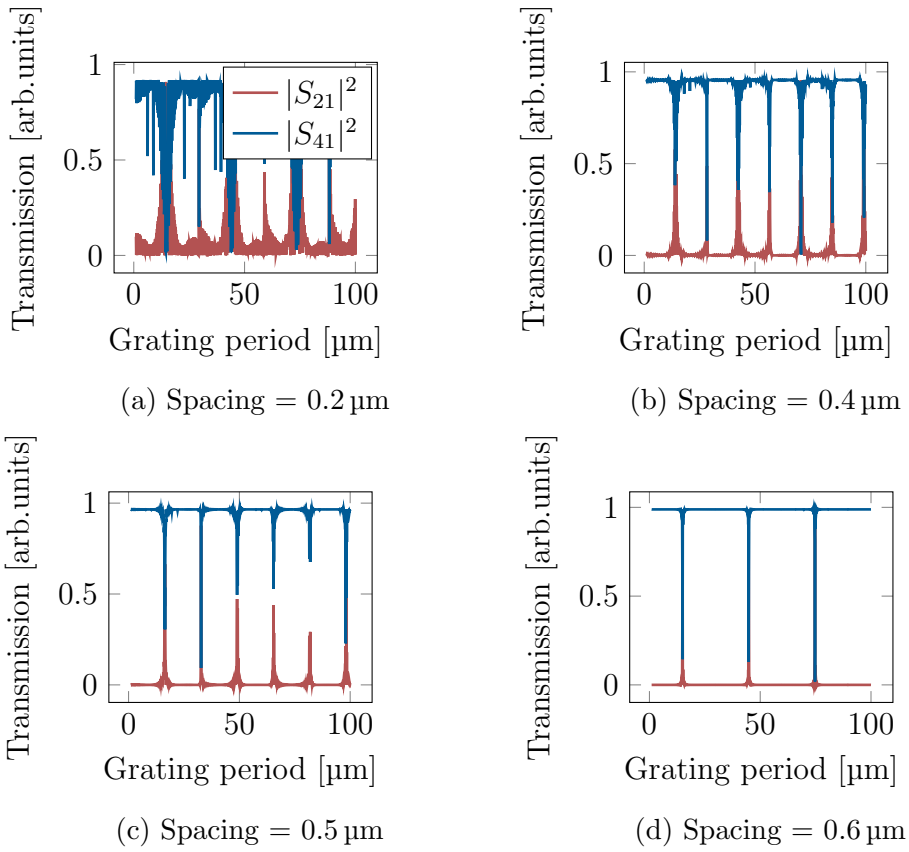

(a) Spacing = 0.2 µm

(b) Spacing = 0.4 µm

(c) Spacing = 0.5 µm

(d) Spacing = 0.6 µm

Figure 8.5: Transmission of power through port 2, $|S_{21}|^2$, and port 4, $|S_41|^2$ from source port 1 as a function of grating periods for different spacings between the waveguides in design A with a grating period of 0.05 µm and 100 periods.

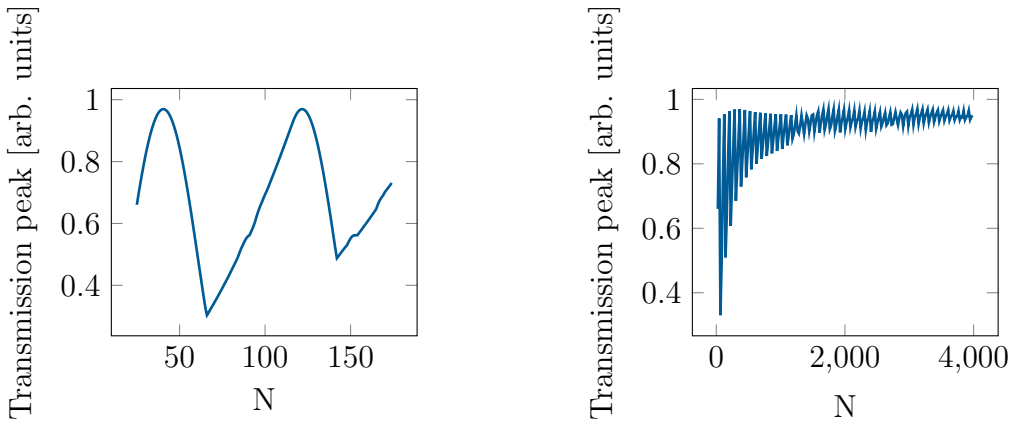

(a)

(b)

Figure 8.6: Peak transmission through port 4 at grating period $\Lambda = 16.3$ µm as a funtion of number of periods N. a) Coupling periodicity was found to be 81. b) The transmission peak converges toward full transmission for large N.

8.3 Fabrication and Characterization of Double LPG Couplers

This section presents the second sample that was fabricated during this thesis, which contained the double LPG structures, as well as improved single LPG couplers. Each design was patterned as five individual structures with grating periods close to the target values obtained from the Lumerical simulations, namely 8.2 µm and 16.3 µm for the single and double designs, respectively[2]. The grating depth of the single LPG coupler was increased to 0.1 µm, while the double LPG couplers retained the same grating depth as used in the simulations, namely 0.05 µm. Furthermore, all devices were extended in length to address the shortcomings from the preceding sample discussed in Section 7.5.

Severe Sample Damage due to Instrument Malfunction

Unfortunately, due to a malfunction in the scriber/breaker device, comprehensive characterization and measurements of these structures could not be obtained. Figure 8.7 displays the two ends of the cleaved sample. One end was successfully cleaved, as shown in Figure 8.7a, while the other end, depicted in Figure 8.7b, was impacted by two unintended scriber marks that intersect with the waveguide structures. Despite attempts to manually remove the portion of the sample between the innermost scriber mark and the cleaved edge, the small size of the affected region made it impractical to remove the portion entirely. A designated breaker instrument was also employed without success. Additionally, the constrained timeline and badly timed maintenance of the EBL system posed further obstacles in fabricating a new sample within the available time frame.

SEM imaging was employed to conduct further examination of the scribing damage, as illustrated in Figure 8.8. The obtained images highlights the failure of the cleavage process to produce a smooth edge, as presented in Figure 8.8a, and reveals that the scribing action resulted in entanglement of the two waveguides, as shown in 8.8b. All devices present on the sample were consequently deemed non-functional.

[2]The actual devices were fabricated with required coupling grating periods for an air environment to prepare for measurements, but the values discussed in the simulations are written here to avoid confusion.

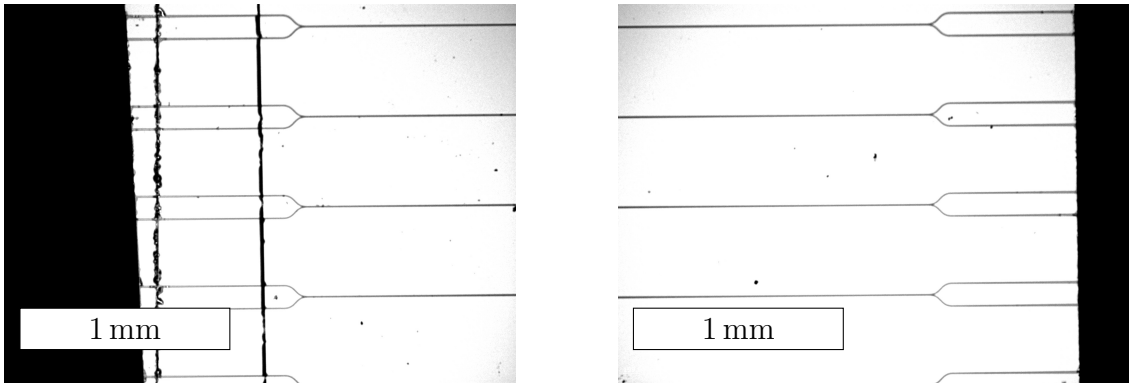

(a) (b)

Figure 8.7: Optical micrographs of the double LPG structures that were damaged during scribing.

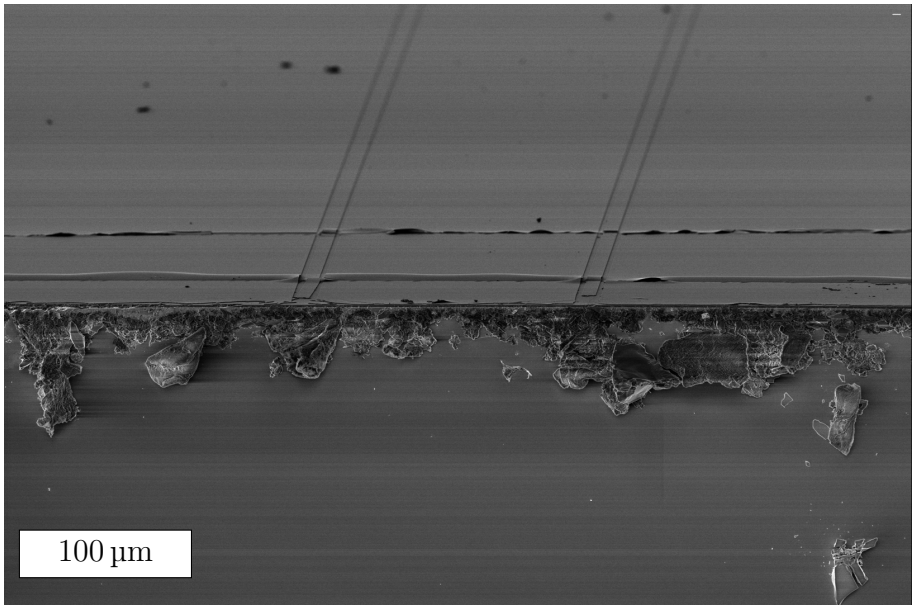

(a)

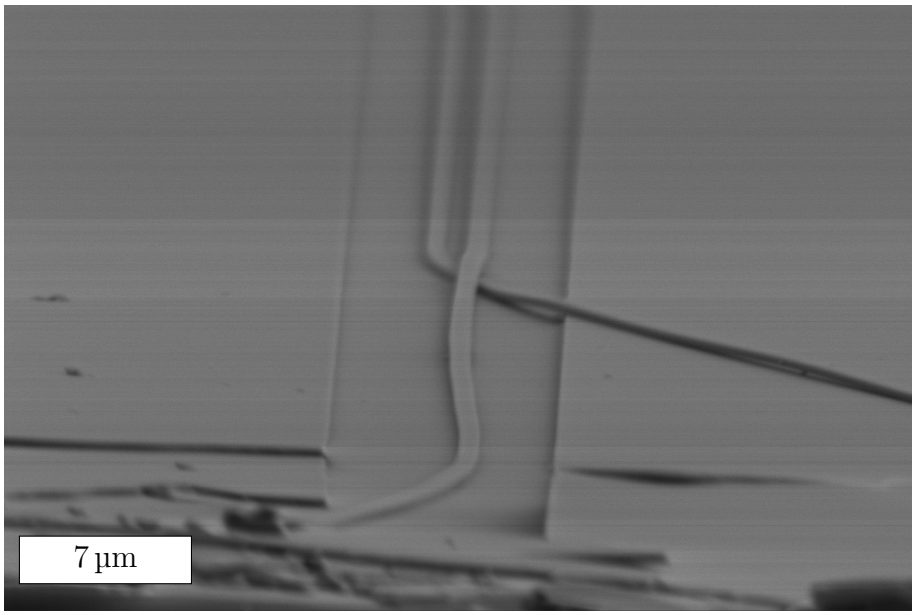

(b)

Figure 8.8: SEM images showing scribing damages exerted on the double LPG structures.

Chapter 9

Conclusion

The main goal of this study has been to design, simulate and fabricate single and double LPG couplers with a focus on sensitivity and transmission characteristics for bio-related applications.

Experimental Procedure

A frequency domain eigenproblem solver from the simulation software MPB was utilized to calculate dispersion relations, required grating periods for coupling and sensitivities in the mid-infrared range. Structures that yielded the highest sensitivities for a wide operation range were subject to transmission simulations conducted with eigenmode expansion methods provided by the Lumerical EME solver. Promising structures were fabricated onto silicon-on-insulator (SOI) samples of $\alpha - \mathrm{Si}$ and SiO_2, by the use of electron beam lithography (EBL) and inductively coupled plasma-reactive ion etching, while the characterization was performed with a scanning electron microscope (SEM). Subsequent measurements were conducted in a laser laboratory utilizing cleaved fibers for light coupling.

Results single LPG Coupler

MPB results of a $0.5 \times 0.22\,\mu m^2$ single LPG coupler predicted coupling to occur for grating periods that are a multiple of $1.48\,\mu m$ and the sensitivity was found to be $0.15\,\mu m/RIU$[1]. Transmission measurements performed in Lumerical, however, predicted that only grating periods corresponding to even-order diffraction modes will achieve coupling. The discrepancy was attributed to the differences in the simulation software such as the grating geoemtry which is not considered in MPB simulations. Furthermore, it is suggested that coupling to asymmetric modes might favor grating periods corresponding to even-order diffraction modes.

The first fabricated sample contained 25 single LPG couplers with different grating periods close to that which was calculated to achieve sufficient coupling in MPB ($5 \times 1.48\,\mu m$). The resulting structures were well-defined and anisotropically etched, but no coupling effect was observed during measurements. The absence of transmission resonances was attributed to short grating lengths and shallow grating depths. Additionally, no coupling was observed for grating periods corresponding to odd

[1]This is a result from preliminary work but included for completness.

diffraction orders in Lumerical simulations, which also explains the transmission results.

Results for Double LPG Coupler

MPB simulations and analysis predicted that a double LPG coupler design (design A) consisting of two single mode waveguides with dimensions $0.433 \times 0.22\,\mu m^2$ and $0.400 \times 0.22\,\mu m^2$, would yield sensitivity of $1.03\,\mu m$/RIU and a reasonably wide operation range. This is significantly higher than typical racetrack ring-resonator designs and comparable to what has been measured for more advanced refractive index sensors. From the MPB simulations, the grating period of design A was calculated to be $17.21\,\mu m$. This was in good agreement with supplementary transmission simulations from Lumerical, which found the same required grating period to be $16.3\,\mu m$. A spacing of $0.5\,\mu m$ between the two waveguides was found from the Lumerical simulations to yield most defined resonances. Resonances at grating periods corresponding to odd diffraction modes were found to be much stronger than even ones. The latter dissapeared completely for larger spacings. It was suggested that coupling to symmetric modes are stronger for grating periods corresponding to odd diffraction orders.

The second fabricated sample contained five single LPG couplers and ten double LPG couplers that were geometrically optimized based on the shortcomings of the first sample. However, due to a malfunctioning scriber system, the sample was severely damaged and deemed useless for transmission measurements.

Final Conclusion

In conclusion, the simulation results presented in this thesis are considered useful for creating double LPG couplers of high sensitivity that can potentially be integrated into nanophotonic sensor devices for biomedical applications. However, further investigation, particularly regarding transmission properties, are required to incorporate loss, dispersion and other obstacles associated with physical devices.

Bibliography

[1] Lars Thylén and Lech Wosinski. 'Integrated photonics in the 21st century'. In: *Photon. Res.* 2.2 (Apr. 2014), pp. 75–81. DOI: 10.1364/PRJ.2.000075. URL: https://opg.optica.org/prj/abstract.cfm?URI=prj-2-2-75.

[2] N. L. Kazanskiy et al. 'State-of-the-Art Optical Devices for Biomedical Sensing Applications—A Review'. In: *Electronics* 10.8 (2021). ISSN: 2079-9292. DOI: 10.3390/electronics10080973. URL: https://www.mdpi.com/2079-9292/10/8/973.

[3] B Sepúlveda et al. 'Optical biosensor microsystems based on the integration of highly sensitive Mach–Zehnder interferometer devices'. In: *Journal of Optics A: Pure and Applied Optics* 8.7 (June 2006), S561. DOI: 10.1088/1464-4258/8/7/S41. URL: https://dx.doi.org/10.1088/1464-4258/8/7/S41.

[4] Enxiao Luan et al. 'Silicon Photonic Biosensors Using Label-Free Detection'. In: *Sensors* 18 (Oct. 2018), p. 3519. DOI: 10.3390/s18103519.

[5] Mukesh Yadav and Astrid Aksnes. 'Multiplexed Mach-Zehnder interferometer assisted ring resonator sensor'. In: *Opt. Express* 30.2 (Jan. 2022), pp. 1388–1396. DOI: 10.1364/OE.448023. URL: https://opg.optica.org/oe/abstract.cfm?URI=oe-30-2-1388.

[6] N. Kazanskiy, Svetlana Khonina and Ali Butt. 'A Review of Photonic Sensors Based on Ring Resonator Structures: Three Widely Used Platforms and Implications of Sensing Applications'. In: 14 (May 2023), p. 1080. DOI: 10.3390/mi14051080.

[7] Jens Høvik et al. 'Waveguide asymmetric long-period grating couplers as refractive index sensors'. In: *Opt. Express* 28.16 (Aug. 2020), pp. 23936–23949. DOI: 10.1364/OE.397561. URL: https://opg.optica.org/oe/abstract.cfm?URI=oe-28-16-23936.

[8] Vipul Rastogi and Kin Chiang. 'Long-Period Gratings in Planar Optical Waveguides'. In: *Applied optics* 41 (Nov. 2002), pp. 6351–5. DOI: 10.1364/AO.41.006351.

[9] John D. Joannopoulos et al. *Photonic Crystals: Molding the Flow of Light (Second Edition)*. 2nd ed. Princeton University Press, 2008. ISBN: 0691124566.

[10] David K Cheng. *Field and Wave Electromagnetics*. eng. Pearson custom library. Harlow: Pearson Education UK, 2013, p. 335. ISBN: 9781292026565.

[11] *The Basics of Guided Waves*. John Wiley Sons, Ltd, 2004. Chap. 2, pp. 11–36. ISBN: 9780470014189. DOI: https://doi.org/10.1002/0470014180.ch2. eprint: https://onlinelibrary.wiley.com/doi/pdf/10.1002/0470014180.ch2. URL: https://onlinelibrary.wiley.com/doi/abs/10.1002/0470014180.ch2.

[12] *Guided-Wave Optics*. John Wiley Sons, Ltd, 2007. Chap. 9, p. 356. ISBN: 9780471358329. DOI: https://doi.org/10.1002/0471213748.ch7. eprint: https://onlinelibrary.wiley.com/doi/pdf/10.1002/0471213748.ch7. URL: https://onlinelibrary.wiley.com/doi/abs/10.1002/0471213748.ch7.

[13] *Guided-Wave Optics*. John Wiley Sons, Ltd, 2007. Chap. 9, p. 358. ISBN: 9780471358329. DOI: https://doi.org/10.1002/0471213748.ch7. eprint: https://onlinelibrary.wiley.com/doi/pdf/10.1002/0471213748.ch7. URL: https://onlinelibrary.wiley.com/doi/abs/10.1002/0471213748.ch7.

[14] *Guided-Wave Optics*. John Wiley Sons, Ltd, 2007. Chap. 7, pp. 353–391. ISBN: 9780471358329. DOI: https://doi.org/10.1002/0471213748.ch7. eprint: https://onlinelibrary.wiley.com/doi/pdf/10.1002/0471213748.ch7. URL: https://onlinelibrary.wiley.com/doi/abs/10.1002/0471213748.ch7.

[15] Espen Hovland. 'Optimization and Fabrication of Multiplexed Mach-Zehnder Interferometer-Assisted Ring Resonator Configuration (MARC) Photonic Sensors'. MA thesis. Norwegian University of Science and Technology, 2022.

[16] *Guided-Wave Optics*. John Wiley Sons, Ltd, 2007. Chap. 9, p. 365. ISBN: 9780471358329. DOI: https://doi.org/10.1002/0471213748.ch7. eprint: https://onlinelibrary.wiley.com/doi/pdf/10.1002/0471213748.ch7. URL: https://onlinelibrary.wiley.com/doi/abs/10.1002/0471213748.ch7.

[17] *Guided-Wave Optics*. John Wiley Sons, Ltd, 2007. Chap. 9, p. 370. ISBN: 9780471358329. DOI: https://doi.org/10.1002/0471213748.ch7. eprint: https://onlinelibrary.wiley.com/doi/pdf/10.1002/0471213748.ch7. URL: https://onlinelibrary.wiley.com/doi/abs/10.1002/0471213748.ch7.

[18] Johannes Skaar and Jacob Linder. *Lyshastighet*. 2021. URL: https://snl.no/lyshastighet.

[19] Dr. Rüdiger Paschotta. *Group index*. Dec. 2022. URL: https://www.rp-photonics.com/group_index.html.

[20] *Guided-Wave Optics*. John Wiley Sons, Ltd, 2007. Chap. 9, p. 367. ISBN: 9780471358329. DOI: https://doi.org/10.1002/0471213748.ch7. eprint: https://onlinelibrary.wiley.com/doi/pdf/10.1002/0471213748.ch7. URL: https://onlinelibrary.wiley.com/doi/abs/10.1002/0471213748.ch7.

[21] Nikhil Agnihotri. *Why silicon still dominates the IC industry*. 2021. URL: https://www.engineersgarage.com/ic-manufacturing-semiconductors-silicon-germanium-gallium-arsenide/.

[22] Christopher Doerr. 'Silicon photonic integration in telecommunications'. In: *Frontiers in Physics* 3 (Aug. 2015). DOI: 10.3389/fphy.2015.00037.

[23] *Guided-Wave Optics*. John Wiley Sons, Ltd, 2007. Chap. 9, p. 367. ISBN: 9780471358329. DOI: https://doi.org/10.1002/0471213748.ch7. eprint: https://onlinelibrary.wiley.com/doi/pdf/10.1002/0471213748.ch7. URL: https://onlinelibrary.wiley.com/doi/abs/10.1002/0471213748.ch7.

[24] G. Reed. *An Introduction to Silicon Photonics*. Vol. 119. May 2007, pp. 161–203. ISBN: 978-3-540-28910-4. DOI: 10.1007/978-3-540-28912-8_7.

[25] W. K. Burns and A. F. Milton. 'Waveguide Transitions and Junctions'. In: *Guided-Wave Optoelectronics*. Ed. by Theodor Tamir. Berlin, Heidelberg: Springer Berlin Heidelberg, 1988, pp. 89–144. ISBN: 978-3-642-97074-0. DOI: 10.1007/978-3-642-97074-0_3. URL: https://doi.org/10.1007/978-3-642-97074-0_3.

[26] *Guided-Wave Optics*. John Wiley Sons, Ltd, 2007. Chap. 9, p. 379. ISBN: 9780471358329. DOI: https://doi.org/10.1002/0471213748.ch7. eprint: https://onlinelibrary.wiley.com/doi/pdf/10.1002/0471213748.ch7. URL: https://onlinelibrary.wiley.com/doi/abs/10.1002/0471213748.ch7.

[27] *Guided-Wave Optics*. John Wiley Sons, Ltd, 2007. Chap. 9, p. 380. ISBN: 9780471358329. DOI: https://doi.org/10.1002/0471213748.ch7. eprint: https://onlinelibrary.wiley.com/doi/pdf/10.1002/0471213748.ch7. URL: https://onlinelibrary.wiley.com/doi/abs/10.1002/0471213748.ch7.

[28] Yingwen Liu et al. 'Evanescent-wave coupling phase-matching for ultrawidely tunable frequency conversion in silicon-waveguide chips'. In: *Opt. Express* 27.20 (Sept. 2019), pp. 28866–28878. DOI: 10.1364/OE.27.028866. URL: https://opg.optica.org/oe/abstract.cfm?URI=oe-27-20-28866.

[29] F Bloch. 'Über die quantenmechanik der elektronen in kristallgittern'. In: *Zeitschrift für physik* 52.7 (1929), pp. 555–600.

[30] L. Alwis, T. Sun and K.T.V. Grattan. '[INVITED] Developments in optical fibre sensors for industrial applications'. In: *Optics Laser Technology* 78 (2016). The year of light: optical fiber sensors and laser material processing, pp. 62–66. ISSN: 0030-3992. DOI: https://doi.org/10.1016/j.optlastec.2015.09.004. URL: https://www.sciencedirect.com/science/article/pii/S0030399215002522.

[31] Xudong Fan et al. 'Sensitive optical biosensors for unlabeled targets: A review'. In: *Analytica Chimica Acta* 620.1 (2008), pp. 8–26. ISSN: 0003-2670. DOI: https://doi.org/10.1016/j.aca.2008.05.022. URL: https://www.sciencedirect.com/science/article/pii/S0003267008009343.

[32] Dominic Gallagher. 'Industry Research Highlights, Photonic CAD Meatures'. In: *LEOS Newsletter* 22.1 (2008), pp. 2–3.

[33] Dominic Gallagher and Thomas Felici. 'Eigenmode Expansion Methods for Simulation of Optical Propagation in Photonics - Pros and Cons'. In: *Proc. SPIE* 4987 (June 2003). DOI: 10.1117/12.473173.

[34] S. G. Johnson. *MIT Photonic Bands User Tutorial*. URL: http://ab-initio.mit.edu/wiki/index.php/MPB_User_Tutorial.

[35] Ansys. *Ansys Lumerical MODE Optical Waveguide Coupler Solver*. URL: https://www.ansys.com/products/photonics/mode.

[36] *EME Solver analysis window overview*. https://optics.ansys.com/hc/en-us/articles/360034917513-EME-Solver-analysis-window-overview.

[37] *EME Tutorial Videos*. https://optics.ansys.com/hc/en-us/sections/360007871793-EME100-List-of-videos.

[38] José María De Teresa, ed. *Nanofabrication*. 2053-2563. IOP Publishing, 2020. Chap. 3. ISBN: 978-0-7503-2608-7. DOI: 10.1088/978-0-7503-2608-7. URL: https://dx.doi.org/10.1088/978-0-7503-2608-7.

[39] A.N. Broers, A.C.F. Hoole and J.M. Ryan. 'Electron beam lithography—Resolution limits'. In: *Microelectronic Engineering* 32.1 (1996). Nanotechnology, pp. 131–142. ISSN: 0167-9317. DOI: https://doi.org/10.1016/0167-9317(95)00368-1. URL: https://www.sciencedirect.com/science/article/pii/0167931795003681.

[40] M. Quirk and J. Serda. *Semiconductor Manufacturing Technology*. Prentice Hall, 2001, p. 385. ISBN: 9780130815200. URL: https://books.google.no/books?id=O2eGQgAACAAJ.

[41] *Inductively Coupled Plasma Etching (ICP RIE)*. https://plasma.oxinst.com/technology/icp-etching.

[42] Daniel Flamm. 'Mechanisms of silicon etching in fluorine- and chlorine-containing plasmas'. In: *Pure and Applied Chemistry - PURE APPL CHEM* 62 (Sept. 1990), pp. 1709–1720. DOI: 10.1351/pac199062091709.

[43] D.K. Sparacin. 'Process and design techniques for low loss integrated silicon photonics'. PhD thesis. Massachusetts Intitute of Technology, 2006.

[44] Ray F. Egerton. In: *Physical principles of electron microscopy*. Springer Science+Business Media, Inc., 2005, pp. 125–143.

[45] Etheresia Pretorius. 'Influence of Acceleration Voltage on Scanning Electron Microscopy of Human Blood Platelets'. In: *Microscopy research and technique* 73 (Jan. 2009), pp. 225–8. DOI: 10.1002/jemt.20778.

[46] Ardavan Oskoii. *Open-Source Computational Electromagnetics Projects*. Oct. 2016. URL: http://www.simpetus.com/projects.html.

[47] Lukas Chrostowski and Michael Hochberg. *Silicon Photonics Design: From Devices to Systems*. Mar. 2015. ISBN: 9781316237113. DOI: 10.1017/cbo9781316084168.

[48] Charles R. Harris et al. 'Array programming with NumPy'. In: *Nature* 585.7825 (Sept. 2020), pp. 357–362. DOI: 10.1038/s41586-020-2649-2. URL: https://doi.org/10.1038/s41586-020-2649-2.

[49] D. Marcuse. 'Directional couplers made of nonidentical asymmetric slabs. Part I: Synchronous couplers'. In: *Journal of Lightwave Technology* 5.1 (1987), pp. 113–118. DOI: 10.1109/JLT.1987.1075399.

[50] Jie Yang et al. 'Analysis of the Symmetric and Anti-Symmetric Modes in Spoof–Insulator–Spoof Waveguides'. In: *Journal of the Physical Society of Japan* 86 (June 2017). DOI: 10.7566/JPSJ.86.064401.

[51] Xueliang Shi et al. 'CMOS-Compatible Long-Range Dielectric-Loaded Plasmonic Waveguides'. In: *Lightwave Technology, Journal of* 31 (Nov. 2013), pp. 3361–3367. DOI: 10.1109/JLT.2013.2281823.

[52] Toto Saktioto et al. 'Theoretical and empirical comparison of coupling coefficient and refractive index estimation for coupled waveguide fiber'. In: *Journal of Applied Science and Engineering Technology* (Jan. 2008).

[53] Yunfei Fu et al. 'Efficient adiabatic silicon-on-insulator waveguide taper'. In: *Photon. Res.* 2.3 (June 2014), A41–A44. DOI: 10.1364/PRJ.2.000A41. URL: https://opg.optica.org/prj/abstract.cfm?URI=prj-2-3-A41.

[54] *PlasmaPro 100 PECVD*. https://ntnu.norfab.no/WebForms/Equipment/EquipmentView.aspx?toolId=33.

[55] Allresist GmbH. *Positive E-Beam Resists AR-P 6200 (CSAR 62) datasheet*. URL: https://www.allresist.com/wp-content/uploads/sites/2/2016/12/allresist_produktinfos_ar-p6200_englisch.pdf.

[56] Hengfei Gu et al. 'Considerable knock-on displacement of metal atoms under a low energy electron beam'. In: *Scientific Reports* 7.1 (2017). DOI: 10.1038/s41598-017-00251-3.

[57] Abraham. Savitzky and M. J. E. Golay. 'Smoothing and Differentiation of Data by Simplified Least Squares Procedures.' In: *Analytical Chemistry* 36.8 (1964), pp. 1627–1639. DOI: 10.1021/ac60214a047. eprint: https://doi.org/10.1021/ac60214a047. URL: https://doi.org/10.1021/ac60214a047.

[58] *Guided-Wave Optics*. John Wiley Sons, Ltd, 2007. Chap. 11, p. 440. ISBN: 9780471358329. DOI: https://doi.org/10.1002/0471213748.ch7. eprint: https://onlinelibrary.wiley.com/doi/pdf/10.1002/0471213748.ch7. URL: https://onlinelibrary.wiley.com/doi/abs/10.1002/0471213748.ch7.

[59] *SAF1550P2 - Mounted SAF Gain Chip*. Accessed: 2023-06-11. URL: https://www.thorlabs.com/thorproduct.cfm?partnumber=SAF1550P2.

[60] Katrien De Vos et al. 'Silicon-on-Insulator microring resonator for sensitive and label-free biosensing'. In: *Opt. Express* 15.12 (June 2007), pp. 7610–7615. DOI: 10.1364/OE.15.007610. URL: https://opg.optica.org/oe/abstract.cfm?URI=oe-15-12-7610.

[61] Jonas Flueckiger et al. 'Sub-wavelength grating for enhanced ring resonator biosensor'. In: *Opt. Express* 24.14 (July 2016), pp. 15672–15686. DOI: 10.1364/OE.24.015672. URL: https://opg.optica.org/oe/abstract.cfm?URI=oe-24-14-15672.

Appendix

A Dose Test Prior to Etching

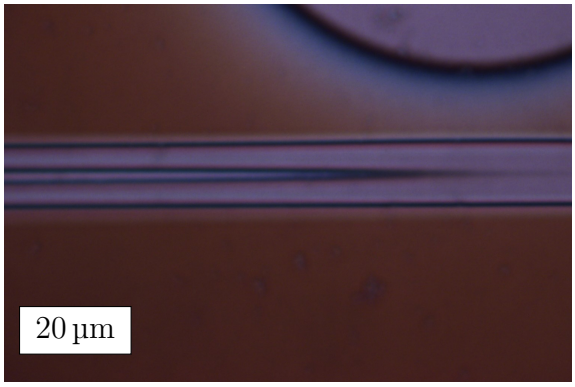

(a) 150 µmC/cm^2

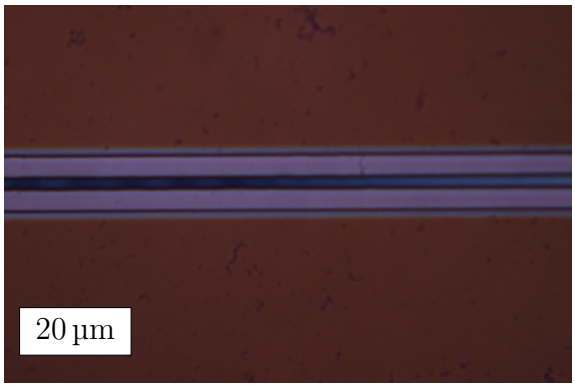

(b) 120 µmC/cm^2

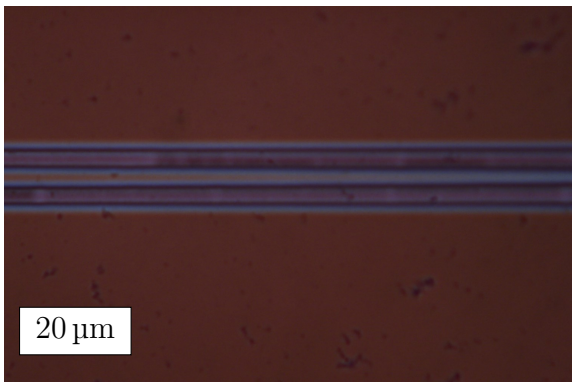

(c) 80 µmC/cm^2

Figure 1: Images from optical microscope depicting 3 identical waveguides that have received three different exposure doses. (a) and (c) are over and underexposed, respectively, while (b) is properly dosed. Pictures taken after exposure but prior to etching.

B Changing Resonance Dips for Higher Number of Periods

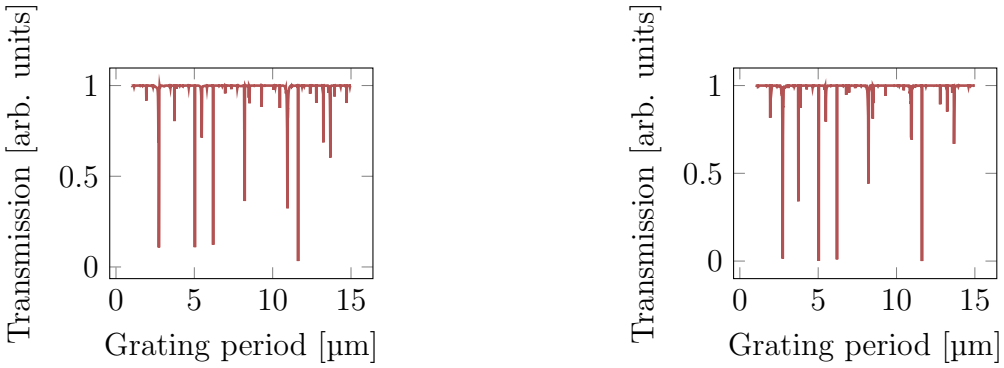

(a) $N = 400$ (b) $N = 1000$.

Figure 2: Transmission plot obtained from Lumerical simulations of $0.5 \times 0.22\,\mu m^2$ single LPG couplers for larger Ns. Changing the number of periods changes the resonance dips as well.

C Additional Measurements 1540-1580nm

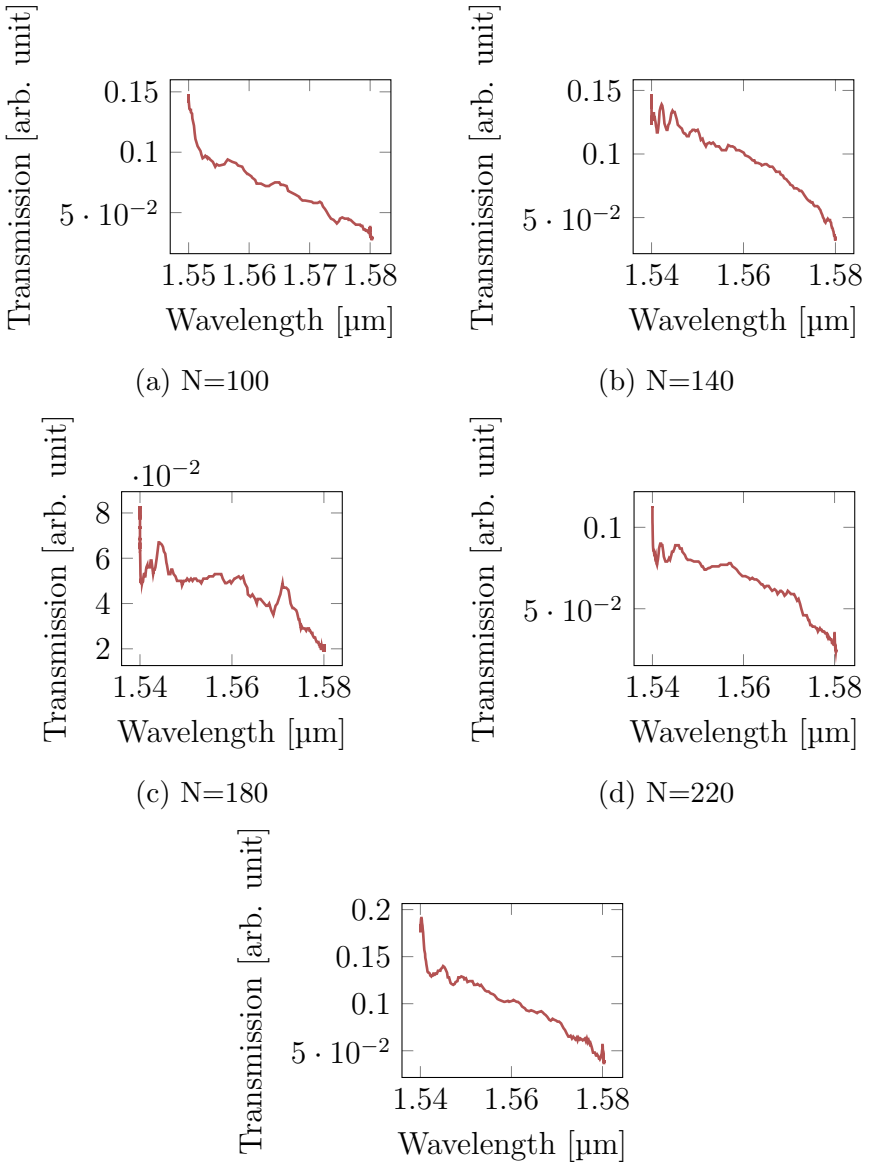

Figure 3: Transmission measurements from single LPG couplers with wavelength range between 1.54 and 1.58 µm with five different coupling lengths, but with identical grating period $\Lambda = 7.4\,\mu m$.

D Symmetrical and Asymmetrical Grating Comparison

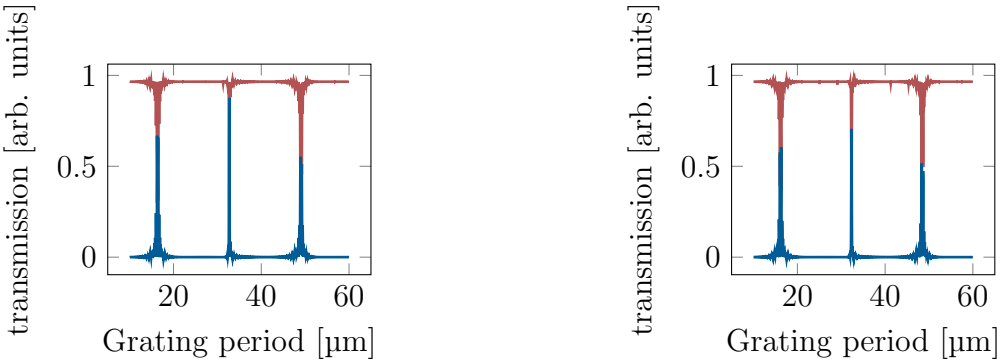

(a) Symmetric

(b) Asymmetric

Figure 4: Transmission plot obtained from Lumerical simulations of a symmetric (a) and an asymmetric (b) double LPG structure. $|S_21|^2$ is plotted red, while $|S_41|$ is plotted blue. No difference was observed when changing the grating symmetry.

E Python script

The following script is what was used to find the double waveguide structure with the highest sensitivity. It includes functions and procedures that were used to investigate the single LPG coupler as well.

```
#!/usr/bin/env python
# coding: utf-8

# In[1]:


import meep as mp
from meep import mpb
from matplotlib import pyplot as plt
import numpy as np
import random
import csv



# In[2]:


#parameters

clad = mp.Medium(index=1.31) #water 1.31
core = mp.Medium(index=3.47) #Si 3.47
substrate = mp.Medium(index=1.44) #SiO2 1.44


#Supercell size
sc_x = 0
sc_y = 2
sc_z = 2

#Geometry waveguides
width_1= 0.5
height_1 = 0.22

#number of pixels per unit length
resolution = 32

#number of bands to calculate
num_k = 40
k_min = 0.1
k_max = 3.0
k_points = mp.interpolate(num_k,[mp.Vector3(k_min),mp.
    Vector3(k_max)])
```

```
num_bands = 1

f_mode = 1/1.55

#Propagation direction
kdir = mp.Vector3(1)
kmag_guess = f_mode*3.45
kmag_min = f_mode*0.1
kmag_max = f_mode*4.0


#Tolerance for find_k
tol = 1e-6

#Tolerance for overlap
tolerance = 0.1

geometry_lattice = mp.Lattice(size = mp.Vector3(sc_x,sc_y,
    sc_z))
band_min = 1
band_max = 1

#Set a global wavelength range to work with as there is a
    lot of wavelength dependence
wl_range = np.linspace(1.2,2.0,100)


# In[5]:


def create_waveguide(w,h):

    geometry = create_geometry(w,h)

    ms = mpb.ModeSolver(
        geometry_lattice = geometry_lattice,
        geometry = geometry,
        resolution = resolution,
        k_points = k_points,
        default_material = clad,
        num_bands = num_bands)
    ms.run_te(mpb.display_yparities, mpb.
        display_group_velocities)

    return ms

def create_geometry(w,h):
        geometry = [mp.Block(
```

```
                    size = mp.Vector3(mp.inf,mp.inf,0.5*(
                        sc_z-h)),
                    center = mp.Vector3(0,0,0.25*(sc_z+h)),
                    material = substrate),
                mp.Block(
                    size =mp.Vector3(mp.inf, w, h),
                    center = mp.Vector3(),
                    material = core)]
        return geometry

def dispersion_relation(wgs):
    #freqs = wg.all_freqs

    #k_points is a list of Vector3 objects
    x_vals = []
    for i in k_points:
        x_vals.append(i[0])

    fig, ax = plt.subplots()
    for i in wgs:
        ax.plot(x_vals,i.all_freqs)

    plt.axhline(y = 1/1.55, color = 'black', linestyle = '--
        ',label="$\lambda$=1.55um") #1.55um wavelength single
        mode

    ax.fill_between(x_vals, [i / 1.44 for i in x_vals], 3.0,
        interpolate=True, color='gray', alpha=0.3)

    plt.legend(["m=1","m=2","$\lambda$=1.55$um","lightline"
        ])
    plt.title("Dispersion relation")
    plt.xlabel("wavevector $k_x$ [2$\pi$ $\mu m^{-1}]$")
    plt.ylabel("frequency [300 THz]")
    plt.show()
    return


#returns the group velocity at frequency f_mode
def get_group_velocity(wg,wl):

    k_modes = wg.find_k(mp.ODD_Y, 1/wl, band_min, band_max,
        kdir, tol, kmag_guess,
                kmag_min, kmag_max, mpb.
                    display_group_velocities)

    return wg.compute_group_velocity_component(mp.Vector3
        (1,0,0))
```

```
#returns a list of effective indexes in x-dir for waveguide
    wg
def get_index(wg,wl):

    f_mode = 1/wl    # frequency corresponding to 1.55 um


    k_modes = wg.find_k(mp.ODD_Y, f_mode, band_min, band_max
        , kdir, tol, kmag_guess,
                kmag_min, kmag_max, mpb.
                    display_group_velocities)
    neffs = []
    for i in k_modes:
        neffs.append(i/f_mode)

    return neffs

#returns the grating period needed for coupling between mode
    with effective index n1 and mode with n2 at wavelength
    wl
def get_grating(n1,n2,wl):
    return abs(wl/(n1-n2))


def get_group_index_diff(geometries,wl_range):

    n_g = []
    freqs = []


    for geo in geometries:
        n_temp = []
        f_temp = []
        for i in k_points:

            ms = mpb.ModeSolver(
                geometry_lattice = geometry_lattice,
                geometry = geo,
                resolution = resolution,
                k_points = [i],
                default_material = clad,
                num_bands = num_bands,
                optimize_grid_size = True #This rounds the
                    grid size in each direction to the
                    nearest integer with small factors, to
                    improve FFT speed.
```

```
                )
            ms.run_te()
            vel = ms.compute_group_velocity_component(mp.
                Vector3(1,0,0))
            n_temp.append(1/vel[0])
            f_temp.append(ms.freqs[0])

        n_g.append(n_temp)
        freqs.append(f_temp)

    n_diffs = []
    for wl in wl_range:
        n_diffs.append((np.interp(1/wl,freqs[0],n_g[0]) - np
            .interp(1/wl,freqs[1],n_g[1])))

    return(n_diffs)

#takes in a geometries and returns the difference in dndc
    for the two
def get_dndc(geometries,wl_range):

    dn_clad = 0.01

    ns = []
    for geo in geometries:

        ms = mpb.ModeSolver(
            geometry_lattice = geometry_lattice,
            geometry = geo,
            resolution = resolution,
            k_points = k_points,
            default_material = mp.Medium(index = (1.31)),
            num_bands = num_bands)

        ms_d = mpb.ModeSolver(
                geometry_lattice = geometry_lattice,
                geometry = geo,
                resolution = resolution,
                k_points = k_points,
                default_material = mp.Medium(index = (1.31+
                    dn_clad)),
                num_bands = num_bands)

        ms.run_te()
        ms_d.run_te()

        f = np.array([i[0] for i in ms.all_freqs])
        f_d = np.array([i[0] for i in ms_d.all_freqs])
```

```
        n = np.array([i[0] for i in k_points])/f
        n_d = np.array([i[0] for i in k_points])/f_d

        ns_temp = []
        for wl in wl_range:
            ns_temp.append((np.interp(1/wl,f,n)-np.interp(1/
                wl,f_d,n_d))/dn_clad)

        ns.append(ns_temp)

    return (np.array(ns[0])-np.array(ns[1]))

#Takes two waveguides and returns false if there is a mode
    overlap at 1.55um. If two modes overlap within the
    tolerance
#it might interfere with the coupling mechanism and thus
    sensing abilities.
def no_overlap(geometries,tolerance):

    k = []

    for geo in geometries:
        ms = mpb.ModeSolver(
                geometry_lattice = geometry_lattice,
                geometry = geo,
                resolution = resolution,
                k_points = k_points,
                default_material = mp.Medium(index = (1.31))
                    ,
                num_bands = num_bands)
        k_modes = ms.find_k(mp.ODD_Y, f_mode, band_min, 2,
            kdir, tol, kmag_guess,
                kmag_min, kmag_max, mpb.
                    display_group_velocities)
        k.append(k_modes)

    if (abs(k[0][0]-k[1][1]) < tolerance) or (abs(k[1][0]-k
        [0][1]) < tolerance):
        return False
    else:
        return True


def get_sensitivity(geometries, wl_range):
    n_d = get_group_index_diff(geometries,wl_range)
    dndc = get_dndc(geometries,wl_range)
```

```
    s = [wl_range[i]*dndc[i]/n_d[i] for i in range(len(
        wl_range))]
    return s


#returns the total sensitivity for a range of sensitivities
    around 1.55
def get_infrasens(sens,wl_range,range_size):
    s = 0
    sensitivity_range = np.linspace(1.55-range_size,1.55+
        range_size,10)

    for wl in sensitivity_range:
        s+=abs(np.interp(wl,wl_range,sens))

    return s

def plot_sensitivity(sens,wl_range):
    plt.plot(wl_range, sens)
    plt.ylabel("Sensitivity")
    plt.xlabel("wavelength [um]")
    plt.ylim(-10,10)
    plt.legend()
    return



#Checks all possible combinations for the given width and
    height range and
#spits out the best sensitivity and geometry. The heights of
    both waveguides for one design is always the same
def best_sensitivity(wl_range,height_range,width_range,
    sens_range):
    highest_sens = 0

    width1 = 0
    height1 = 0

    width2 = 0

    combinations = []

    for w1 in width_range:

        for h1 in height_range:
            geo1 = create_geometry(w1,h1)
```

```
            wg1 = (w1,h1) #save a tuple of this combination
                to avoid duplicate simulation
            for w2 in width_range:
                wg2 = (w2,h1)
                comb_set = {wg1,wg2}
                if comb_set not in combinations:
                    combinations.append(comb_set)
                    geo2 = create_geometry(w2,h1)
                    if no_overlap([geo1,geo2],tolerance):
                        sen = get_sensitivity([geo1,geo2],
                            wl_range)
                        sensitivity = abs(get_infrasens(sen,
                            wl_range,sens_range))
                        if sensitivity > highest_sens:
                                highest_sens = sensitivity

                                width1 = w1
                                height1 = h1
                                width2 = w2

    print("Highest sensitivity: ", highest_sens)
    print("w1 = ",width1)
    print("h1 = ",height1)
    print("w2 = ",width2)
    retdic = {"sensitivity":highest_sens, "w1":width1,"h1":
        height1,"w2":width2}
    return retdic


def best_sensitivity_consth(wl_range,h,width_range,
    sens_range):
    highest_sens = 0

    width1 = 0
    width2 = 0

    widths = []

    combinations = []

    for w1 in width_range:
        geo1 = create_geometry(w1,h)
        wg1 = (w1,h) #save a tuple of this combination to
            avoid duplicate simulation
        for w2 in width_range:
            wg2 = (w2,h)
            comb_set = {wg1,wg2}
            if comb_set not in combinations:
```

```
                if w1 != w2:
                    combinations.append(comb_set)
                    geo2 = create_geometry(w2,h)
                    if no_overlap([geo1,geo2],tolerance):
                        widths.append([w1,w2])
                        sen = get_sensitivity([geo1,geo2],
                            wl_range)
                        sensitivity = abs(get_infrasens(sen,
                            wl_range,sens_range))
                        if sensitivity > highest_sens:
                                highest_sens = sensitivity
                                width1 = w1
                                width2 = w2

    print("Highest sensitivity: ", highest_sens)
    print("w1 = ",width1)
    print("h = ",h)
    print("w2 = ",width2)
    print("Tested widths:")
    print(widths)
    retdic = {"sensitivity":highest_sens, "w1":width1,"h":h,
        "w2":width2}
    return retdic


# In[6]:


wl_range = np.linspace(1.4,1.7,100)
height_range = np.linspace(0.20,0.4,10)
width_range = np.linspace(0.4,0.7,10)
sens_range = 0.1


# In[38]:


const_h_sens = best_sensitivity_consth(wl_range,0.22,
    width_range,sens_range)
varying_h = best_sensitivity(wl_range,height_range,
    width_range,sens_range)
```

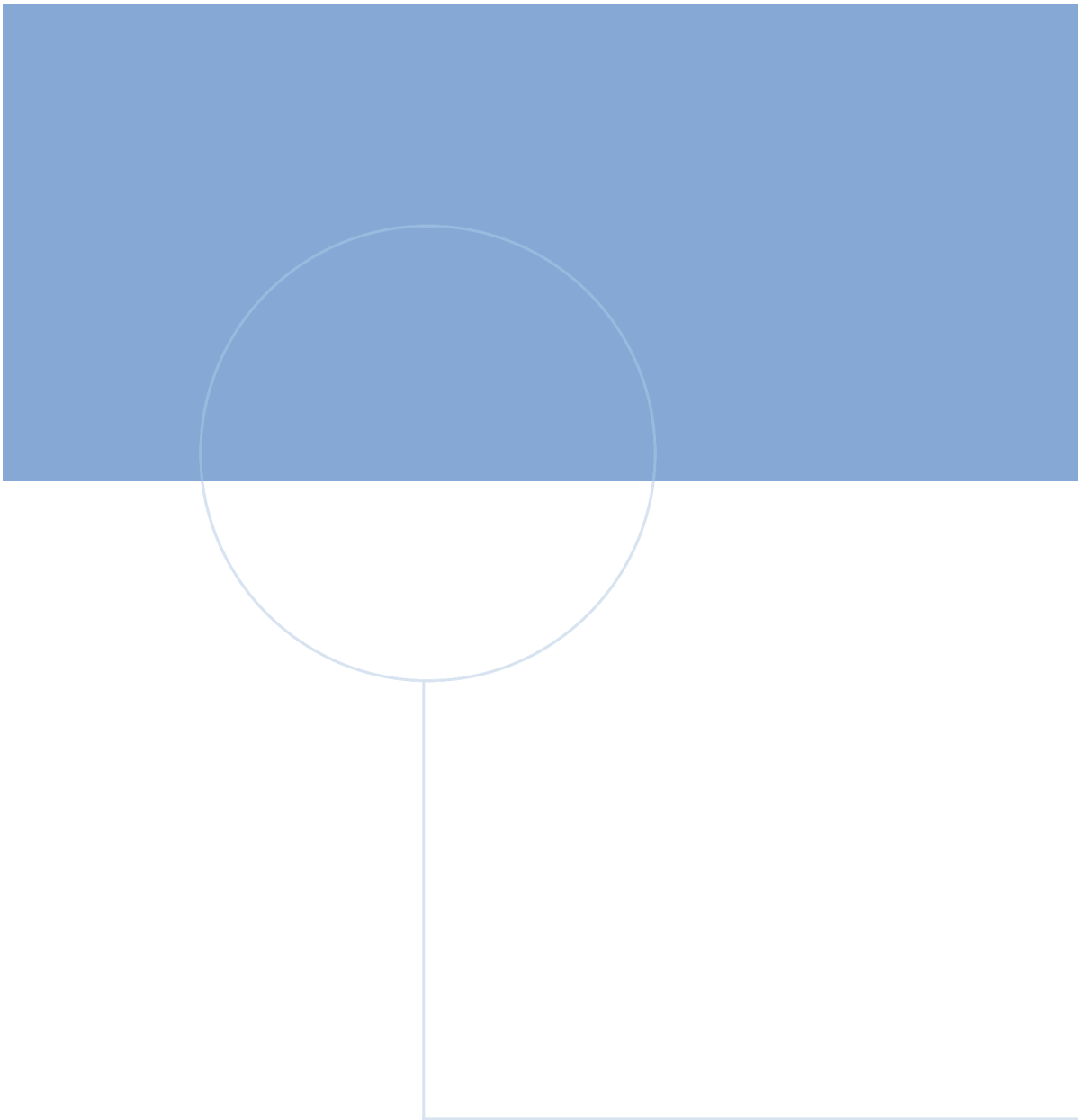

NTNU

Kunnskap for en bedre verden